POLITECNICO DI MILANO

School of Industrial and Information Engineering

Master of Science in

Materials Engineering and Nanotechnology


# LIGHT HARVESTING CAPACITORS

Supervisor: **Prof. Guglielmo Lanzani**

Co-supervisor: **Prof. Cesare Soci**

Master Degree Thesis of:

**Paolo GRILLI** - ID 850170

Academic year 2016/2017

*Alla mia famiglia,*

*per essere sempre al mio fianco.*

# I. Abstract

Over the last decade, organic semi-conductive materials have attracted increasing interest in the field of photovoltaic energy harvesting (OPV). They are easy to fabricate, cheap and environmental-friendly. However, the maximum efficiencies that have been achieved are barely above 10%. The main restriction with organic semi-conductive materials lays in their limited conductivity, which is usually thousands of times smaller if compared to the characteristic one for their inorganic counterparts. Trying to solve this problematic, a new light harvesting concept is presented in this master thesis: the **light harvesting capacitor (LHC)**. The fundamental advantage of LHCs lays in the fact that the charge transport is completely removed thanks to the addition of two insulant layers to the classic OPV heterojunction. This work focuses firstly on the development of a physical model, then on devices fabrication and finally on their characterization.

As already mentioned the starting point was the development of a theoretical model on MATLAB to predict the parameters dependency. After that, the focus switched to the analysis of the donor/acceptor couple: copper phthalocyanine (CuPc) and fullerene ($C_{60}$). Specifically, a study of the active bi-layer was performed with both ultrafast and steady-state pump-probe spectroscopies. This was done to observe the exciton splitting mechanism and the lifetime of the separated charges within the active layer itself. Regarding the actual device fabrication, both the two small molecules were thermally evaporated on top of the insulant layer and then enclosed by an additional one. In order to verify the accuracy of the theoretical model predictions, three different dielectric materials were exploited at three different thicknesses each: a spin-coated PMMA, a thermally evaporated $ZrO_2$ and an atomic layer deposited (ALD) $TiO_2$. Given the semi-conductive character of titanium dioxide, a preventive study was performed to verify its appropriateness as an insulant material. All the structures were tested measuring the time-resolved current generated under light and dark cycles at different frequencies. The transient photo-current was then integrated to obtain the stored charge allowing the computation of the final external efficiency. Although the values obtained were rather far from the simulated ones, indicating a necessary optimization of the active bi-layer, the increase ratios associated to the insulant material changes were properly predicted. This was actually not completely true when the employed insulant was $TiO_2$ since the efficiency rise was definitely higher than expected. The explanation for that was found in the atypical behavior of titania which was therefore selected as the most performing insulant to use for LHCs fabrication. Finally, the aim of the last section was the study of the light intensity effect on the device performance in order to verify the accuracy of another aspect of the theorized physical model. Some puzzling results were found, indicating that further studies on this promising device need to be done.

# II. Estratto

Nel corso dell'ultimo decennio, i materiali organici semiconduttivi hanno attirato un crescente interesse nel campo del fotovoltaico, in quanto facili da fabbricare, economici e con un basso impatto ambientale. Tuttavia, la massima efficienza raggiunta è di poco superiore al 10%. Il principale ostacolo all'utilizzo dei materiali organici semiconduttivi risiede nella loro limitata conducibilità, che è migliaia di volte inferiore a quella delle loro controparti inorganiche. Per cercare di risolvere questo problema, un nuovo concetto per la raccolta di energia verrà presentato in questa tesi magistrale: il **light harvesting capacitor** (**LHC**). Il vantaggio fondamentale risiede nel fatto che qualsiasi meccanismo di trasporto di carica è completamente rimosso grazie all'aggiunta di due strati elettricamente isolanti alla classica struttura organica. L'elaborato si concentra inizialmente sulla creazione di un modello fisico, successivamente sulla fabbricazione di dispositivi ed infine sulla loro caratterizzazione.

Il modello teorizzato, che mira a predire la dipendenza del sistema dai diversi parametri, è stato sviluppato su MATLAB. In seguito, l'attenzione si è spostata sull'analisi della coppia donatore/accettore ftalocianina di rame (CuPc) e fullerene ($C_{60}$). Nello specifico è stato effettuato uno studio dello strato attivo utilizzando due diverse spettroscopie pump-probe per osservare il meccanismo di separazione di carica e il loro tempo di decadimento. Passando alla fabbricazione vera e propria, entrambe le small molecule sono state evaporate termicamente su un film di materiale isolante e racchiuse da un ulteriore strato del medesimo. Per verificare l'accuratezza del modello, sono stati utilizzati tre diversi materiali dielettrici, ciascuno a tre differenti spessori: spin-coated PMMA, $ZrO_2$ termicamente evaporato e ALD $TiO_2$. Dato il carattere semiconduttivo dell'ossido di titanio, è stato svolto uno studio preventivo per verificarne l'idoneità come materiale isolante. Tutte le diverse strutture sono state caratterizzate misurando la corrente generata tramite cicli luce-buio a diverse frequenze. Questa corrente è stata poi integrata per ricavare la carica immagazzinata nel dispositivo e quindi l'efficienza esterna. Anche se i valori risultanti sono decisamente più bassi di quelli simulati, indicando che un'ottimizzazione dello strato attivo è indispensabile, gli incrementi ottenuti con le variazioni sul materiale isolante si avvicinano alle predizioni del modello. È bene puntualizzare come quest'ultima affermazione non sia del tutto vera quando si utilizza $TiO_2$, in quanto la crescita in efficienza riscontrata è stata di molto superiore alle aspettative. La spiegazione per questo fenomeno risiede nel comportamento atipico della titania, che è stata quindi selezionata come il miglior dielettrico da utilizzare nella fabbricazione di LHC. Infine, nell'ultima parte della tesi, è stato studiato l'effetto dell'intensità luminosa sulla performance del dispositivo, così da verificare l'accuratezza di un altro aspetto del modello fisico. Tuttavia i risultati ottenuti non sono conclusivi, indicando come sia necessario studiare più approfonditamente questi promettenti dispositivi.

# III. Acknowledgements

First of all, I would like to thank professor Guglielmo Lanzani for giving me the opportunity to work on his own innovative idea for energy harvesting in one of the most prestigious university: Nanyang Technological University (NTU). I would also like to thank professor Cesare Soci for letting me join his group at NTU and for guiding me throughout my first experience in academic research during the eight months I spent in Singapore. Moreover, I want to acknowledge all the people in the CDPT group that helped me with either the laboratory permits or part of the experiments: Sruthi Varier, Giorgio Adamo, Annalisa Bruno, Harish Krishnamoorthy, Azhar Iqbal, Xin Yu Chin. Special thanks are due to Francesco Maddalena and Walter Wong that spent a great amount of their time, even if they had not to, helping me with my thesis project. I must also acknowledge both Giuseppe Paternò and Carlo Perini in IIT, Milan.

At last, but not least, I would like to thank my family for their support throughout my years of studies; my old friends back home, for always being there when I needed them; the new ones I met in Milan, for living together with me this great experience; and all the friends that I met around the world for teaching me the importance of different cultures.

# IV. Scope and survey of the thesis

The aim of this master thesis is to study light harvesting capacitors in order to better understand the working principle and the involved device parameters. Trying to improve the efficiency is also one of the goals. The first step is the implementation of a theoretical model to predict the behavior of LHCs. The software used to develop this model is MATLAB and the simulation results are exploited to study the different parameters dependence. The following stage is the fabrication of actual LHCs with the use of different deposition techniques: spin-coating, thermal evaporation and atomic layer deposition. The final phase is the characterization of the produced devices, through a special current measurement set-up, and of the active bi-layer itself, with two pump-probe spectroscopy techniques. The LHC external efficiencies obtained experimentally are then compared with the simulated ones. The focus is on single active bi-layer devices only.

# V. Table of contents

# VI. List of figures

# VII. List of tables

# Chapter I. Introduction

1000 oil barrels, 100 000 $m^3$ of natural gas and 100 eq oil tons of coal. This is the amount of fossil fuels the world population is consuming every second in 2015 [1]. Considering that those kind of energy resources are not unlimited and moreover they are harmful not only to the planet we are living in, but also to our own health, we clearly need to change road or we will eventually have to face the so-called "Tragedy of the Commons". This concept was first proposed by a Victorian economist in the 19$^{th}$ century, but it became widely known in 1968 with the article from Garrett Hardin. It is not directly related to the energy problem, although lately it has been applied to it more and more often. It basically expresses the notion that whenever there is an open source, every human being will exploit it considering only his own personal need. This clearly does not work when the source itself is not unlimited and will eventually end [2].

The world energy demand is currently 15 trillion watt (TW), a number which has increased exponentially since the Industrial Revolution and which keep rising in a quite appalling way. To produce this humongous amount, as already said, humans mainly rely on fossil fuels, which cover more than 80% of the total need as shown in figure I.1. However, other alternative sources that can supply us without damaging the earth exist [3, 4].

Renewable energies have been known for longer than fossil fuels (the first evidence of a wind mill is contained in a hindu book dated 400 BC [5]) and they are probably the best option to solve the energy problem. Although the efficiency reached in hydropower energy harvesting is close to 90% and with wind turbines is around 40% [6], those two alone cannot provide sufficient power to cover the world current need. On the other hand, the solar radiation hits the earth with 90 petaWatt (PW) average, which is more than 6000 times the actual demand. Even considering that part of it is required for other processes like photosynthesis or for atmospheric circulation, there is still plenty left. The problem then is to exploit this enormous amount of energy that reaches us every day in an efficiently enough manner. The device which aim to do so is the photovoltaic solar cell, which is able to convert the energy of incident photons in circulating current. Different kinds of solar cells are being studied and although the working principle is rather simple, there is still plenty of research that needs to be done to optimize the process and to make it more affordable [6].

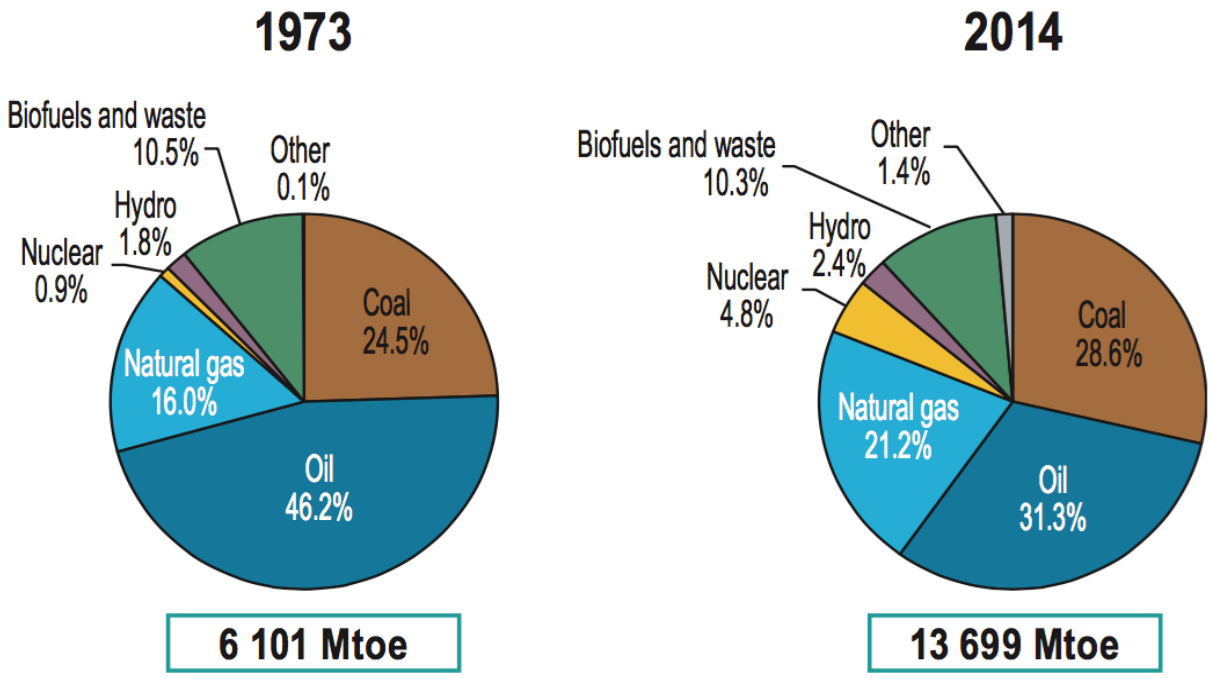


*Figure I.1 World energy production in million tonne of equivalent oil (Mtoe). Comparison between 1973 and 2014 [3].*

# I.1 Photovoltaic Cell

The very first indication of a photovoltaic (PV) effect has been found in 1839 by Edmond Becquerel while experimenting in his father's laboratory. He discovered that, when shined with light, a silver chloride electrode connected to platinum electrodes and immersed in an electrolytic solution will generate a voltage and a current [7]. However, almost fifty more years were needed for the construction of an actual photovoltaic cell and hundred more to obtain one, based on silicon, able to power some electrical equipment in 1954 [8].

Starting from that moment, the interest of the community has increased notably and lot of different materials and technologies have been studied to improve those devices that can represent the key to solve the global energy problem. Although the efficiency/cost ratio is not appealing enough to replace the more commonly used fossil fuels yet, in isolated area like south of Italy or some parts of Spain, photovoltaic devices would already be more affordable than the national energy grid. However, it is clear that before solar cells could actually replace fossil fuels there is still a long way to go. And it is also clear that in order for the research to keep going and eventually being able to make PV more attractive, both governments and companies have to keep investing money in this field.

## I.1.1 Inorganic PV cells

The first class of materials exploited to produce photovoltaic cell was the family of inorganic semiconductors. Since it has been known for quite a long time, the working mechanism is reasonably well understood and furthermore the efficiency reached is higher than with other kind of PV devices. Those are the two reasons why inorganic solar cells are usually the starting point to study solar energy harvesting processes. Within this class of materials, silicon was the first to be exploited. Since it was also used in other electronic devices (e.g. transistors), the progresses in the production techniques and in the theoretical understanding itself were quite fast. Other semiconductors are part of the III-V family, which is analyzed further in a later paragraph, and of the II-VI one.

### *I.1.1.1 Working principle*

Generally speaking, a PV cell is a device able to convert photons energy into a circulating current. To understand better what is actually happening, the overall process can be divided into multiple steps as shown in figure I.2 [9].

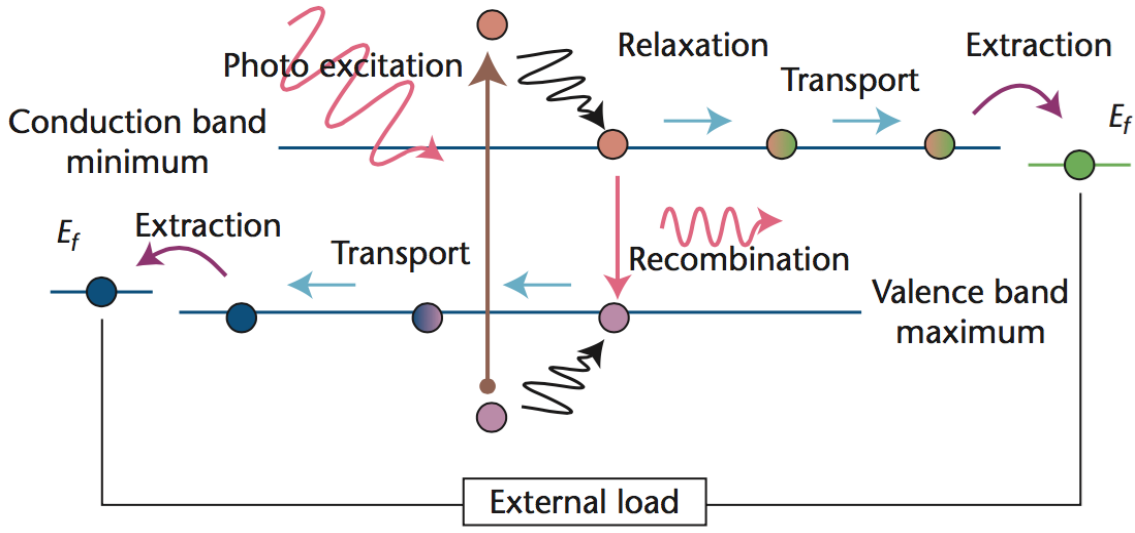


*Figure I.2 Schematic view of the photovoltaic process [10].*

First, a photon is absorbed by the material and its energy is spent to excite an electron to the conduction band leaving behind a hole. For the two free charges to flow to the respective electrodes, a relaxation phenomenon has to occur. When it reaches it, the electron whose energy has been pumped by the incoming photon, take an external path to lose it and recombine with one of the holes on the opposite electrode. The external path usually involves some electrical load or storage mechanism [10].

The fundamental structure to obtain such a device is the so-called p-n junction which is schematically represented in figure I.3. This configuration, which is also used in other devices like photodetectors, is based on a joint between two materials: a p-doped semiconductor and a n-doped one.

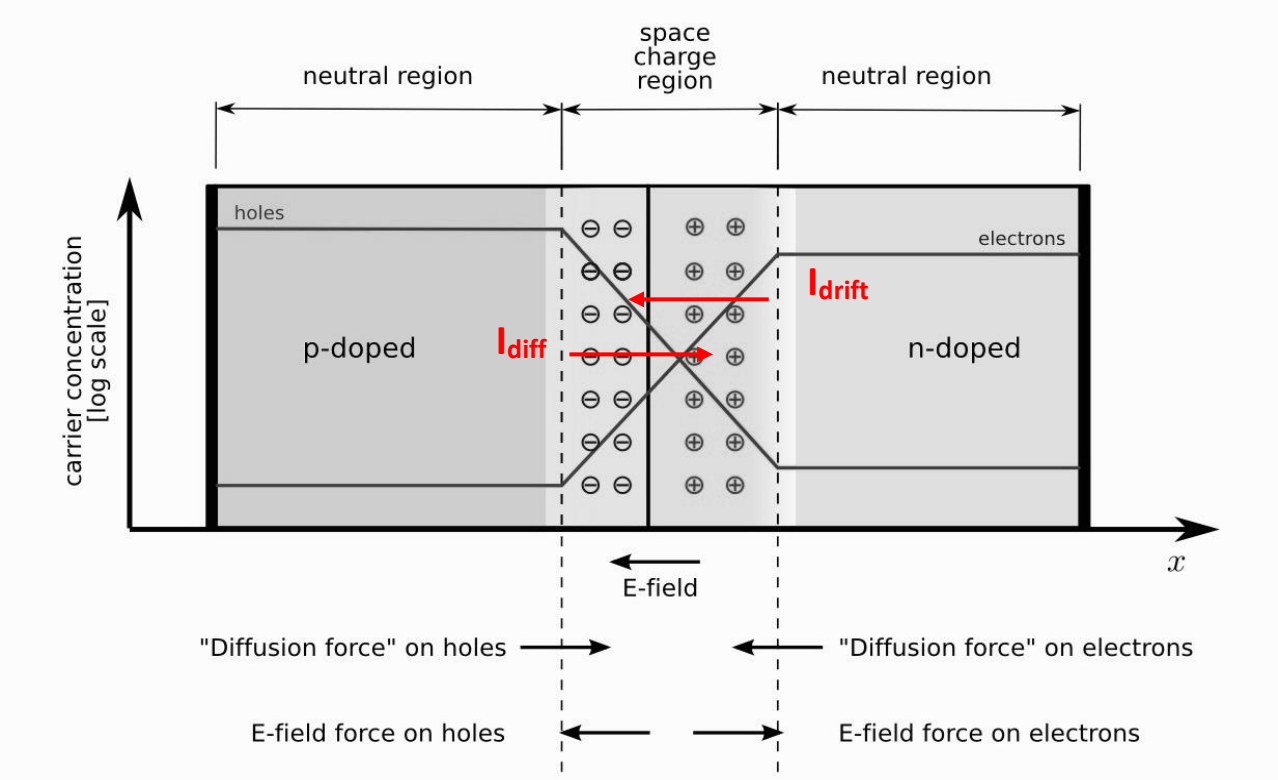


*Figure I.3 Schematic view of a p-n junction.*

When those two materials are connected the difference in charge carriers concentration across the junction will lead to a diffusion phenomenon. Electrons will flow toward the p side and holes toward the n side, generating a diffusion current $I_{diff}$. As a consequence, a depletion region (or space charge region SCR) is formed. Since the ionized acceptors and donors are left behind, an electric field is then formed in this region. Thus, the charge carriers will be driven in the opposite direction from that of the diffusion phenomenon, producing a drift current $I_{drift}$. When those two contrary currents are equal, an equilibrium characterized by a built in potential ΔV is reached [11]. Increasing the quantity of dopants improves the electric field but decreases the SCR width instead.

When the junction is shined with light, electron-hole pairs are generated and, if that occurs in the SCR where the internal electric field is present, a photocurrent $I_{ph}$ going through the external load starts flowing. In order for the charges to be separated, and thus contribute to the photocurrent, the pair generation has to occur either in the SCR or within a diffusion length distance from it. Due to the band structure of the semiconductor, it is evident that the circulating current consists of minority charge carriers. The working mechanism of organic PV cells is slightly different and it will be analyzed later. For the time being, the focus will be on the materials used for inorganic ones.

### *I.1.1.2 Materials and technologies*

The first solar cell considered to be viable for energy harvesting was based on silicon, and in the actual PV market, silicon is still the most used one with more than 90% of the total photovoltaic output. After the first single crystal cell made in the 50's, lots of new techniques have been developed, as depicted in the trend shown in figure I.4, but the efficiency record (on the market) still belongs to the former.

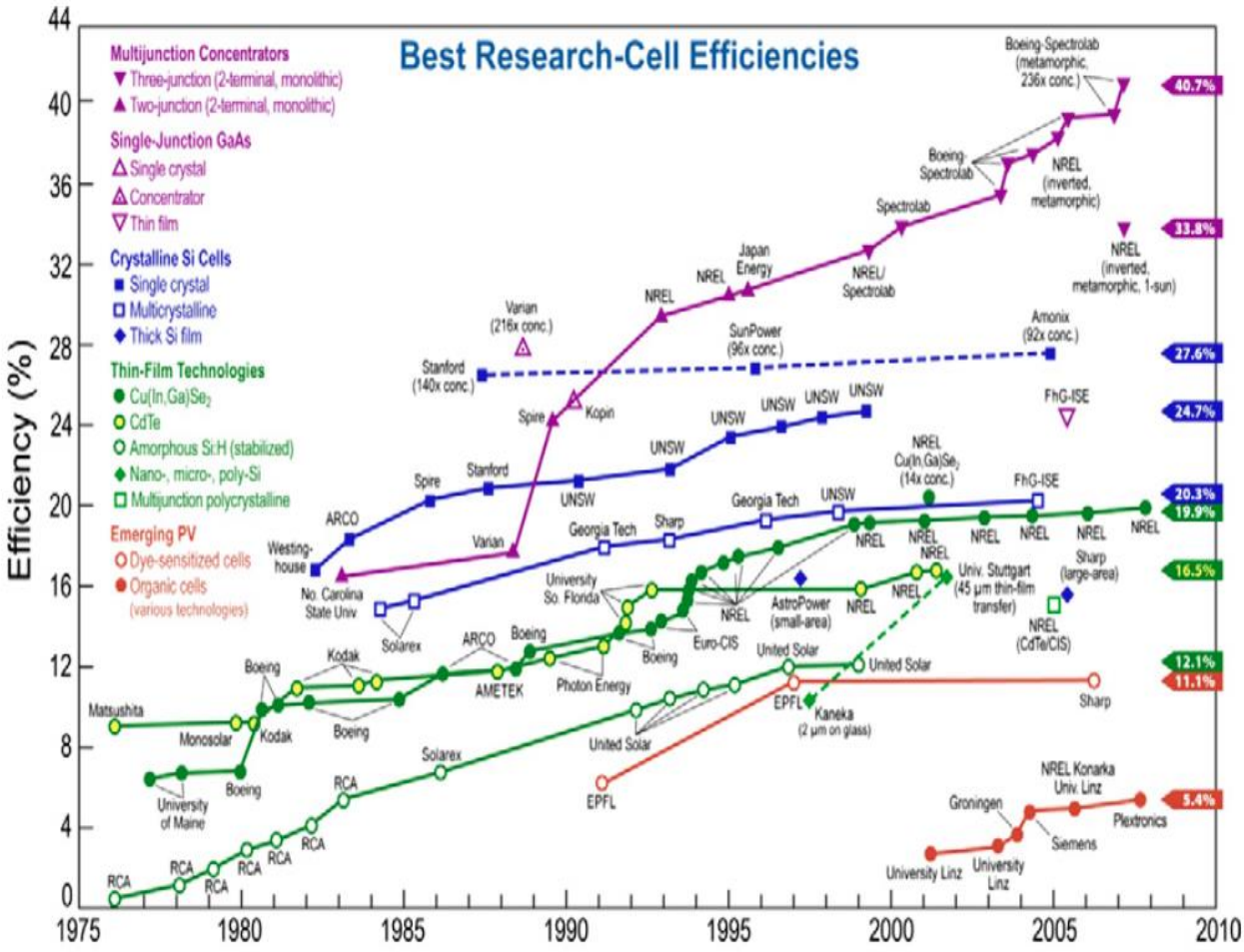


*Figure I.4 Solar energy harvesting technology trend from 1975 [13].*

More in detail, a single crystal wafer was grown by float-zone process that, combined with the passivated emitter rear locally diffused (PERL), led to an efficiency as high as 24.7% [11]. However, most of the silicon solar cell on the market are produced with Czochralski (CZ) process that allows to obtain a defect-free lattice with low recombination losses. Nevertheless, some contaminations are present on the boron-doped wafer i.e. oxygen and carbon [12].

Poly-crystalline cells have also been studied, reaching an efficiency of 19.8%. However, although they present some advantages, the cost difference with the former type is not significant and does not justify their usage over the previous kind presented [13].

After that, the researchers focus was on finding a way to fabricate thin silicon film PV units. This kind of devices instead, present numerous benefits in terms of cost, dimensions and integration. The technologies involved are newer if compared to the ones used up to this point for single and poly-crystal cells and that is why the efficiency reached is not as high (13.4%). The best one is based on amorphous silica (a-Si) film obtained by plasma enhanced CVD. However, due to a large number of dangling bonds, to dope amorphous silicon a high amount of hydrogen needs be present has shown in figure I.5 [13].

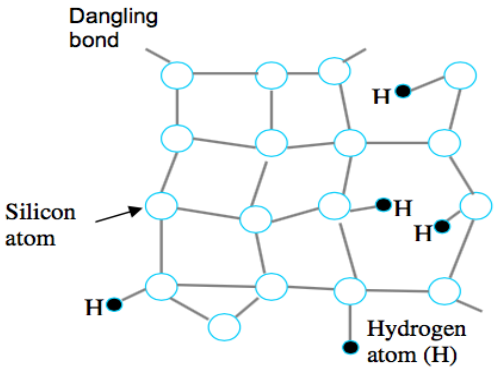


*Figure I.5 Network of a-Si exhibiting broken silicon atom dangling bonds, which are passivated by hydrogen atoms [13].*

With this kind of devices however, the conventional p-n configuration is not suitable due to the large presence of defect states even after the hydrogen passivation. To solve this problem the so-called p-i-n configuration is used instead. In this case an interlayer of intrinsic semiconductor is added with the only function of absorbing light. The free charges generated are then separated by the p-n electric field. The final cell looks like the one in the figure I.6 and can either be obtained by "superstrate" (p-layer first) or "substrate" (n-layer first), that makes it a rather flexible technique [13].

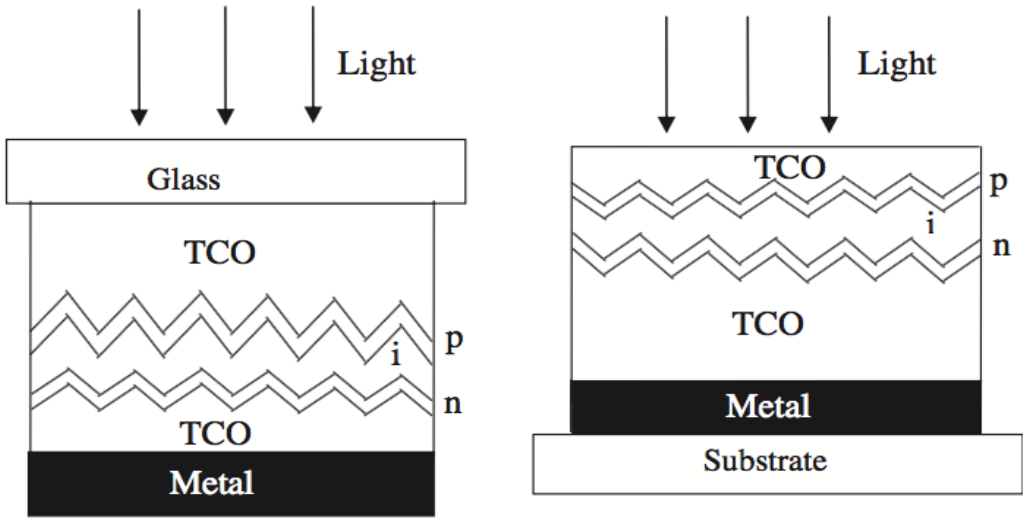


*Figure I.6 (left) a-Si solar cell in "superstrate" p–i–n configuration, and (right) "substrate" n–i–p configuration [13].*

A viable alternative to silicon-based PV are the III-V single- and multi- junction solar cells that present a number of attractive properties. First of all, the bandgaps in this family of semiconductors are conveniently spread over the solar spectrum. Furthermore, having them similar crystalline structures, multi-junction can be fabricated. Exploiting this technique, one of the main limitation for silicon solar cell, the bandgap, can be partially overcome. This limitation is basically related to the photon absorption phenomenon: a photon with less energy than $E_{gap}$ will not be absorbed, while on the other hand a photon with higher energy than $E_{gap}$ will be absorbed but will dissipate the excess [14].

The key to efficiently use the solar spectrum is to build a structure where each sub-cell possesses a higher bandgap than the one below it, as shown in figure I.7. In this way, each sub-cell absorbs light from the spectral range closest to its band gap, hence reducing thermalization losses [14].

Another important part of the whole structure is the tunnel junction that avoid the formation of unwanted p-on-n junction which would block the current flow. A suitable interconnector must have a low electrical resistivity and a high optical transmissivity, and it has to be integrated into the structure [14]. With this technology the efficiency has been boosted to the highest level ever reached for a PV solar cell, namely 46% [15]. However, the very high cost and the extreme toxicity of the precursors used in the molecular beam epitaxy, make them competitive only in space system applications. Before a commercial usage can become feasible, those two problems need to be solved [16].

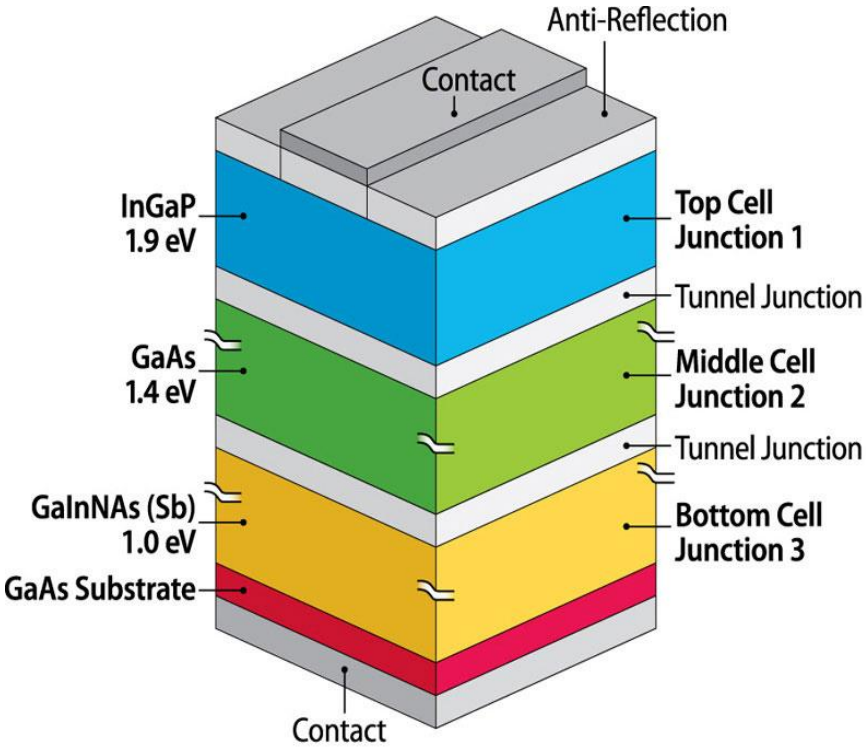


*Figure I.7 Schematic view of a III-V multi-junction solar cell [14].*

## I.1.2 Organic PV cells (OPV)

Considering a theoretical limit efficiency which is the same as for conventional semiconductors devices and production costs related to plastic processing, organic photovoltaic solar cells are possibly the key to achieve an economically feasible large-scale energy harvesting.

The main advantages lay in the fact that all the organic materials used are relatively inexpensive and they usually have a high absorption coefficient. Moreover, they can be processed with low-temperature approaches that further decrease the processing cost and which allow the use of other substrates that are not stable enough for the temperatures reached during inorganic devices fabrication [13].

The first conductive polymer was reported in the 70's and it was basically a chemically doped poly-acetylene. The first major milestone in the OPV field however, was achieved by C. W. Tang [17] who was able to produce, in 1985, a single heterojunction solar cell with an efficiency as high as 1% based on copper phthalocyanine (CuPc) and a perylene tetracarboxylic derivative (PTCBI) (figure I.8). Starting from that moment, lot of research had been going on trying to properly tailor the materials to use and to achieve the best device structure possible [18].

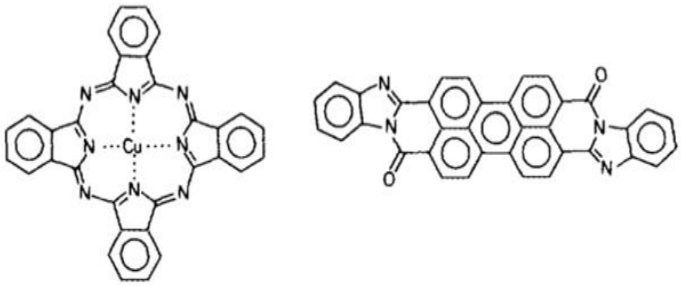


*Figure I.8 Chemical structure of CuPc (on the left) and PTCBI (on the right) [17].*

### *I.1.2.1 Working principle*

Although the working principle is quite similar to the one used in the explanation of the classic inorganic p-n junction devices, it is not completely the same. The understanding of the overall process is far less advanced than for conventional PV cells and it remains an intense subject of research studies.

The key difference is in the light absorption phenomenon that does not lead any more to the creation of free charges. In the case of OPV, when a photon is absorbed, a strongly bounded electron-hole pair called exciton is formed. As a consequence of the quite high binding energy, dissociating them and therefore generating the photocurrent, requires an interface of some kind between p and n type (donor/acceptor) materials, used directly in their pristine state. Accordingly, in contrast with inorganic devices, the photocurrent is produced by major charge carriers. In a similar way to the conventional p-n junction

structure though, the exciton formation needs to be within diffusion length distance from the interface itself, which is the key to create the two separate charges [18].

Figure I.9 summarizes the four steps involved in the photovoltaic process generating the photocurrent. The first one is of course light absorption and exciton formation in the donor. After that, the e-h pair has to diffuse at the donor-acceptor interface. Once there, the charges separation will occur and the free charges will then flow to the respective electrodes.

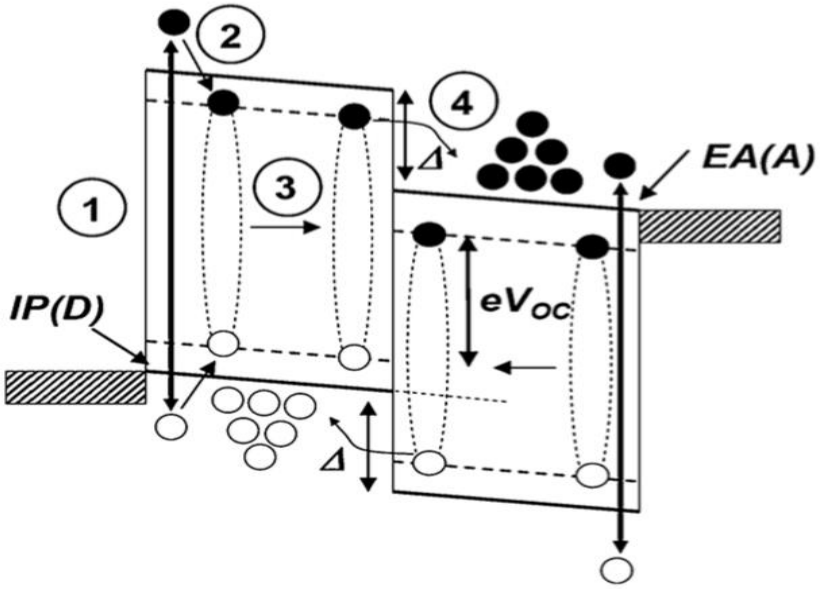


*Figure I.9 Schematic view of the organic photovoltaic process [18].*

However, to be more accurate, between the exciton and charge separation there is an additional step called charge transfer (CT) state. This CT states correspond to a situation where hole and electron are technically separated, but still coulombically bound and that is why it is also called bound polaron pair [19]. To have the complete charges separation, the energy $E_{CT}$ related to the electron in the acceptor LUMO and to the hole in the donor HOMO has to be overcome. Where exactly is this energy coming from, is not completely clear yet, but several hypotheses have been proposed like the presence of disorders or the assistance of phonons [18, 19].

## *I.1.2.2 Materials and technologies*

When studying OPV, it is worth noting that not only the cell working mechanism is different, but also the materials involved themselves are quite singular. Organic semiconductors do not have a band structure as the one present in inorganic ones like silicon. They are instead characterized by a Highest Occupied Molecular Level (HOMO, comparable to the valence band) and a Lowest Unoccupied Molecular Level (LUMO, comparable to the conduction band).

To achieve such a conductive polymer, the key is to obtain a high electron delocalization so that they can freely move and generate a current. Considering that a π-bond is much less localized than a σ-bond (fig. I.10), a polymer chain having a perfect alternation of double and single bonds, like poly-acetylene, will have a quite high delocalization. Theoretically speaking, the higher the extent of the conjugation, which is how the single-double bond alternation is called, the higher the conductivity. However, a perfect conductive polymer, with value close to metallic materials, cannot be achieved due to the Peierls distortion and to a certain influence of intermolecular forces. More in details, instead of having a homogenous delocalization, the stability is higher with the formation of dimerized structures which therefore lead to a decrease of the conjugation. For sake of comparison, the charge carries mobility in crystalline inorganic semiconductor is $10^2$ to $10^3$ $cm^2/(V*s)$, while in organic materials ranges from $10^{-6}$ to $10^{-3}$ $cm^2/(V*s)$, with maximum values around 1 $cm^2/(V*s)$, for highly ordered crystalline materials [18]. Those values of mobility are directly related to the polymer conductivity and allow to predict, for example, the carrier drift length [20].

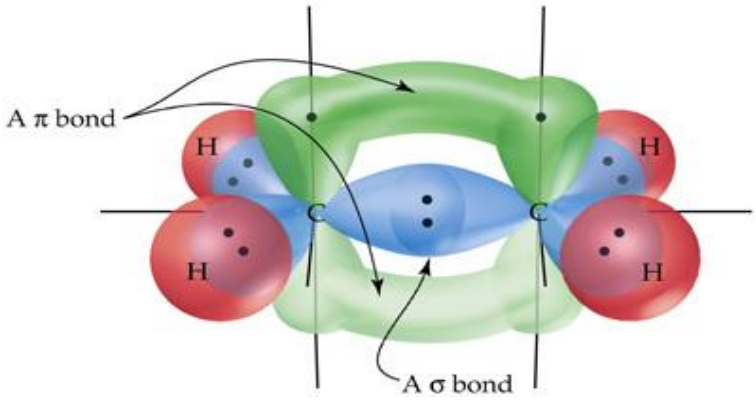


*Figure I.10 Electron delocalization occurring during a π- bond [22].*

Although poly-acetylene was first synthetized in 1958 by Natta, the conductivity obtained was very low and his work was not accepted widely in the field. It was almost 20 years later that Shirakawa, MacDiarmid and Heeger were finally able to produce an actual conductive version of the polymer. The key to achieve that result, basically discovered by serendipity, was to dope the poly-acetylene with bromine vapor (also iodine and $AsF_5$ can be exploited). In a similar way to inorganic semiconductors, the doping leads to the formation of holes (or extra electron in case of n-doping) as shown in figure I.11.
However, the amount of dopant needed in the case of organic semiconductors is some percentage and not in the ppm range. The conduction phenomenon is then represented by hopping of charge carriers, namely solitons, polarons or bipolarons (positive in case of p-doping and negative in case of n-doping), either from one polymer chain to another or along the chain itself [21, 22, 23].

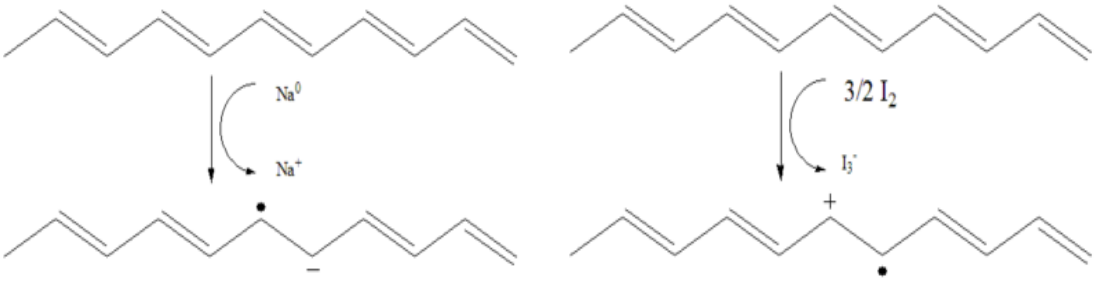


*Figure I.11 Formation of a negative soliton on the left (n-doping) and of a positive soliton on the right (p-doping). The related anti-soliton is shown as well [23].*

A feasible alternative to conductive polymers, without leaving the organic family, is represented by small molecules. A classic example is pentancene, represented in figure I.12, where there is no more alternation of single and double bonds along a backbone chain. The delocalization in this case is instead achieved thanks to fused benzene rings. The crystallinity level achievable with this group of chemicals is higher than with polymers like poly-acetylene and as consequence the mobility is higher as well. However, small molecules are usually not soluble, implicating that processing them is more complex and usually require evaporation techniques in vacuum.

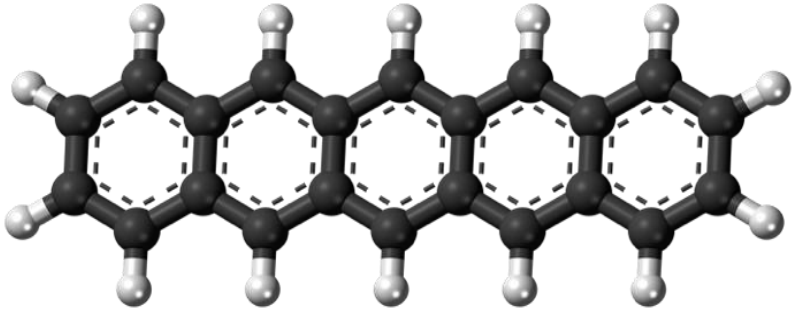

*Figure I.12 Chemical structure of a pentancene molecule.*

All the compounds part of the organic semiconductors family, meaning both polymer and small molecules, are further divided into two categories depending on their HOMO/LUMO levels positions i.e. donor and acceptor. When the LUMO level is rather low and as a consequence the material is more willing to accept an electron, it is called acceptor (or n-type). When instead the HOMO level is high, losing an electron and acquiring a hole is more likely, hence it is called donor (or p-type). The amount of donor compounds available is quite wide, but the same is not true for acceptor ones, that are mainly based on fullerene derivatives. That is why when wanting to tune the device properties one has to work on the donor material that can be tailored accordingly. For example, to increase the light absorption the band gap has to decrease, and the most common way to achieve that is to use the donor/acceptor strategy on the p-type polymer during the synthesis.

One of the most common p-type material used for organic solar cell is Poly3-hexylthiophene (P3HT) reported in the figure I.13 which has excellent properties: high optical absorption in the range 400-600 nm; high hole mobility, up to 0.1 $cm^2/(V*s)$ [24]; regio-regularity is also easily obtained. Regarding n-type material instead, the most used is PCBM (fig 13), which is basically a fullerene molecule with an attached alkyl chain to make it soluble [25].

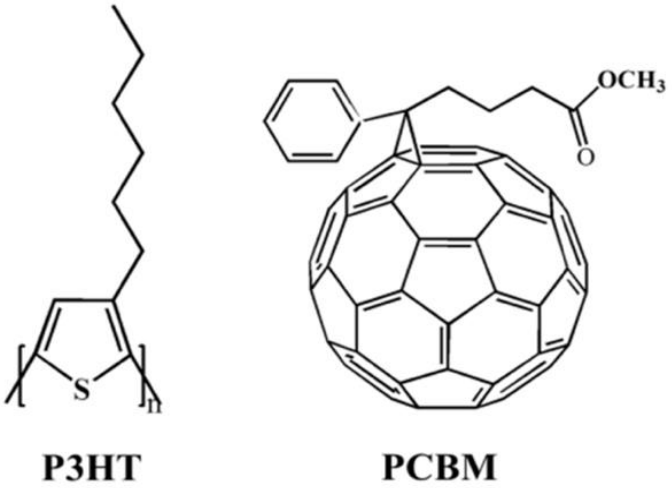


*Figure I.13 Chemical structure of the two most widely used D/A couple [24].*

Now that the cause for exciton separation occurring at the interface between the two compounds is clearer, it also unmistakable that the A/D interface itself is crucial to obtain an efficient charge separation. This is the reason behind the target of several research groups which, starting from the very first acceptable efficiency obtained with the single heterojunction, are now trying to improve as much as possible such interface. The main problem with the bi-layer configuration is that to achieve a high enough absorption, the absorber (usually the donor) has to be thick enough. Increasing the thickness however, might lead to an exciton formation not within diffusion length distance from the interface. In this scenario, the exciton will recombine before the charge separation can occur and the efficiency will drop. It seems then that transport and sufficient absorption are incompatible [18].

The solution came with the currently most studied configuration, the so-called bulk-heterojunction, which is shown in comparison with the bi-layer one in figure I.14. In this kind of design, the A/D components are mixed together forming an interpenetrating, phase-separated network with a nanoscale morphology. Since with this new structure the heterojunction is distributed across the whole layer, the charge separation is much more efficient, leaving holes in the donor material and electrons in the acceptor one. A supplementary advantage lays in the percolation pathways which facilitate the charges transport to the respective electrodes.

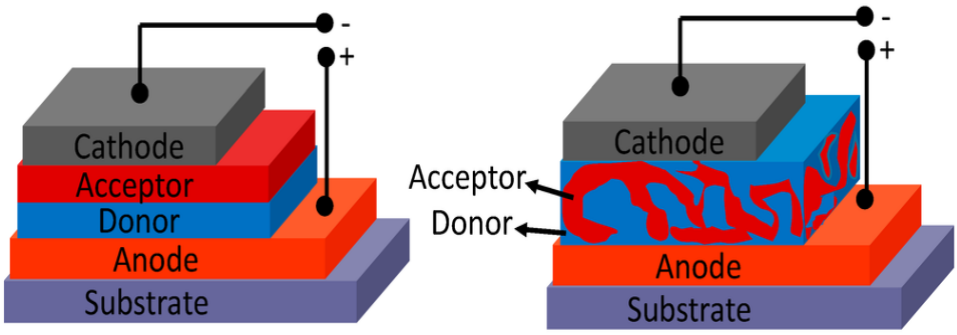


*Figure I.14 Comparison between bi-layer heterojunction (left) and bulk heterojunction (right) [20].*

The first multi heterojunction proposed in 1995 was based on a blend of PCBM and a poly-phenylene-vinylene derivative [26]. However, the maximum efficiency obtainable with this D/A couple was around 3% and for that reason, new donor materials were explored. A suitable alternative was represented by a poly-alkyl-thiophene, the above mentioned P3HT. Although it was already known as a good conductive polymer, the efficiency achievable was rather low when compared to the former one and this is why it was only after new findings in 2002 that the interest for this polymer started to rise. The key discovery was the radical improvement of the device resulting from an annealing process. At first the reason behind this was not very clear, but after few years three main reasons were found. During the heating process, the P3HT matrix softens (I) allowing the diffusion of PCMB molecules and their subsequent aggregation (II). The now PCBM free polymer matrix can recrystallize into larger fibril-like crystal (III). With this new kind of donor material and fabrication process, the final efficiency was boosted up to 5% [27].

Nevertheless, low charge mobility is still one of the main complications limiting the final efficiency of the device. An overall comparison of the main PV cells efficiencies obtained so far is shown in table I.1. It is possible to observe as the highest ones reported for OPV are around 6%, meaning that they are still far from being competitive at any level [18]. The charge transport mechanism and its related problems will be discussed in the next section.

*Table I.1 Selected examples of device parameters for solar cells measured under AM 1.5G, 100 mW/cm²*

| Device type | Efficiency |
|---|---|
| Monocrystalline Si PERL cell | 24.7 |
| Multicrystalline Si cell | 18.2 |
| Monocrystalline Si commercial module | 16.9 |
| a-Si cell | 13.0 |
| CdTe cell | 16.0 |
| OPV: 1986 Tang cell | 0.9 |
| OPV: Small molecule cell | 3.5 |
| OPV: P3HT:PCBM single cell | 5.1 |
| OPV: tandem cell | 6.5 |

# I.2. Charge transport mechanism

Once free electrons and holes are formed in conventional semiconductors after light irradiation, they are free to flow respectively in the conduction and valence band, eventually reaching the electrodes. When working with organic semiconductors however, the conduction mechanism is completely different. As already anticipated, it is based instead on the hopping of carriers from molecule to molecule. More in details the electron transfer process has been studied by A. Marcus, whose theory has been used to obtain a transfer rate '$k_{et}$':

$$k_{et} = \frac{V^2}{\hbar}\sqrt{\frac{\pi}{\lambda k_b T}}\exp\{-\frac{(\Delta G^0 + \lambda)^2}{4\lambda k_b T}\}$$

*Eq. I-1*

where $\Delta G^0$ [J] is the free energy difference between the initial and final molecular sites, V [N] is the coupling strength and $\lambda$ [J] is the reorganization energy term which is further divided into an internal and external term. The internal one reflects changes in molecular geometry associated with going from the neutral state to the ionized state, and vice versa. The external one is instead related to the change in electronic polarization of surrounding molecules [28]. The most important parameters are the coupling strength and the reorganization term that can both be calculated theoretically with several approaches as the "Band-Fitting Method" for 'V' and "Normal Mode Analysis" for '$\lambda$'. With the knowledge of the charge transfer rate, it is then possible to evaluate charge mobility considering a single hopping step, or more accurately through random walk simulation for the charge diffusion trajectories. Since the former method is the easiest and allows a good enough understating, it is the only one reported here. The starting point is the definition of mobility which is the ability of carriers to flow under an applied electric field and its expressed as follow:

$$\mu = \frac{\nu}{F}$$

*Eq. I-2*

where $\nu$ [m/s] is the charge drift velocity and $F$ [V/m] is the driving electric field. Assuming that the charge transport is a Boltzmann hopping process, with a travelling length equal to the nearest inter-site distance $a$ [m] and a hopping time $\tau$ [s], it is possible to define the drift velocity as:

$$\nu \approx \frac{a}{\tau} = ak$$

*Eq. I-3*

where '$\tau$' can also be expressed as the reciprocal of the transfer rate '$k$'. In this scenario though, the electron transfer rate obtained by Marcus theory has to be modified due to the electric field contribution as follow [28]:

$$k_{et} = \frac{V^2}{\hbar}\sqrt{\frac{\pi}{\lambda k_b T}}\exp\left\{-\frac{(\Delta G^0 + eFa + \lambda)^2}{4\lambda k_b T}\right\}$$

*Eq. I-4*

where $F$ [V/m] is again the driving electric field, $a$ [m] is the inter-site distance and $e$ [Q] is the fundamental charge.

Now that charge transport process has been examined in a deeper manner, it is possible to better understand why the mobility in organic semiconductors is definitely lower than in conventional ones. It is also possible to understand why charge transport is one of the main issues in the general organic photovoltaic process. First of all, a poor charge transport leads to a charge recombination process that become competitive with the charge collection one, decreasing the resulting photocurrent. In a second place, the collection process at the electrodes is also limited by the mobility of the material decreasing further the final efficiency. Another problem caused by low mobility, is related to the charge pair separation subsequent the exciton dissociation which appears to be less effective. However, since the overall charge separation phenomenon is not completely understood, the reason behind this is not known as well [29].

Finally, although it is not exactly related to the charge transport process itself, one last problem is due to the high interface present in the most commonly used configuration. Exploiting the bulk heterojunction structure, the donor/acceptor blend allows to obtain a very high charge separation efficiency. However, it may also lead to higher charge recombination, which in turn decreases the final photocurrent [29,30].

To solve all the issues just presented, a new kind of devices has been developed and proposed. However, instead of trying to improve the charge transport process of organic materials, it simply gets rid of it. This new promising device is called: light harvesting capacitors [31].

# I.3 Light harvesting capacitors (LHCs)

Presented for the first time in 2012, light harvesting capacitors (fig. I.15) promise to solve all the charge transport related problems at the same time. The key to do so is to basically remove any kind of charge transport phenomena within the device itself.

The structure to achieve such a goal is very close to the bi-layer heterojunction where the D/A interface is exploited to separate the charges. However, in the LHC an insulant layer of PMMA is added between the organic materials and the electrodes as depicted in figure I.15. In this way, the free charges separated at the interface are prevented from transferring to either the anode or the cathode [31].

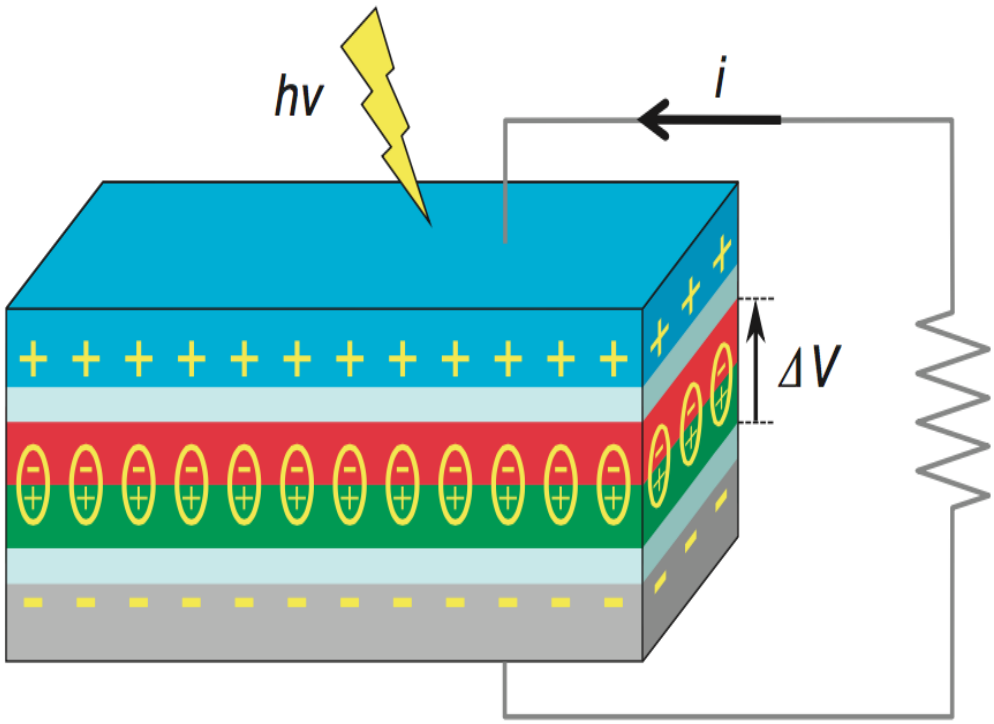


*Figure I.15 Schematic view of light harvesting capacitor [31].*

The bi-layer then, upon illumination, undergoes a macroscopic polarization induced by the coherent sum of oriented nano-dipoles generated after photon absorption. This polarized medium will therefore induce a circulating current in the external circuit that can be exploited through an electrical load [31].

The materials evaporated in the paper (Garbugli et. al) as donors and acceptors are reported in the figure I.16 together with the circulating current obtained experimentally. It is possible to observe as the circulating current peaks follow the illumination profile. This behavior can be explained based on the same working mechanism behind pyroelectric materials, that are mainly used for photodetectors [32]. Namely

these two peaks can be associated to both the charging and discharging of the LHC that therefore is working in an alternate regime. When the capacitor is charging, and thus the potential difference across the device is increasing, electrons will be ejected from the ITO electrode. As consequence, the positive current will start flowing from the gold side. When the device is placed in the dark instead, the polarization will start decaying off leading to another circulating current in the opposite direction due to charges attraction toward the surface of ITO. Hence the negative peak [31].

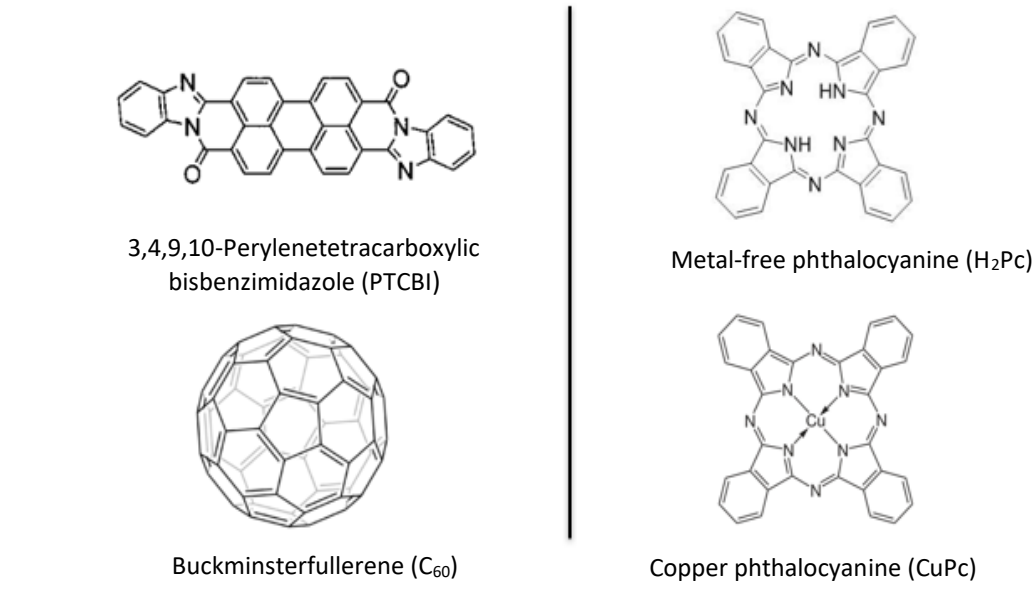


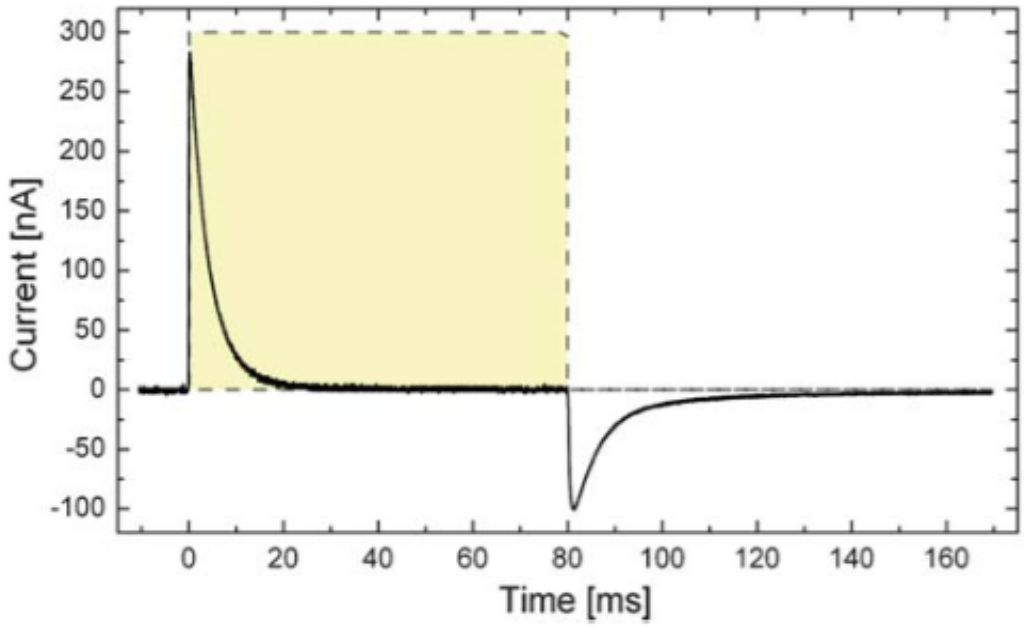


*Figure I.16 Molecular structures of the considered A/D pairs (top). Circulating current obtained experimentally with an illumination (dotted line) wavelength of 632 nm and 40 mW/cm² intensity (bottom) [31].*

To have an overall idea on the internal quantum efficiency dependences, it is possible to start from the ratio between the electrostatic energy stored ($u$) in the capacitor and the absorbed radiation ($E_{light}$). Considering that a long-lived dipole is generated for each absorbed photon (no recombination assumption), a first approximated formula can be obtained:

$$u = \frac{1}{2}\varepsilon_0 F^2$$

*Eq. I-5*

$$F = \frac{n}{V} * \frac{\Delta\mu}{\varepsilon_0} = N\frac{\Delta\mu}{\varepsilon_0}$$

*Eq. I-6*

$$\eta_{int} = \frac{u}{E_{light}} = \frac{N(\Delta\mu)^2}{2\varepsilon_0 h\nu}$$

*Eq. I-7*

where $F$ [V/m] is the electric field, $N$ [1/m$^3$] is volumetric density of absorbed photons (based on the previous assumption is also equal to the dipoles density), $\Delta\mu$ [C*m] is the average dipole moment, $h\nu$ [J] is the absorbed photon energy and $\varepsilon_0$[F/m] is the vacuum permittivity. It is possible to observe that a high dipole density and large dipole moment increase the final efficiency [30]. To make the assumption of one dipole generated for each photon absorbed reasonable, the active layer has to be thin enough. That means the thickness of both the donor and acceptor layers should be smaller than the diffusion length of the exciton itself, considered to be around 25 nm. A consequence of this though, is a very low light absorption. However, since the charge collection is not an issue, stacking more double-layer separated by insulant layers increases the overall absorption without affecting the global working mechanism of the device. Moreover, the choice of proper active materials with different absorption peaks can further improve the final external efficiency. To show the effect of stacking more active double-layer, a three-bilayer device has also been fabricated and characterized. The current improvements together with the absorption spectra are reported in figure I.17 [31].

The actual device fabricated and tested in the paper was characterized under monochromatic illumination. An external efficiency for the bi-layer of 0.025% has been reported. This rather low value, when compared to the theoretical limit, is due to some experimental limitations. Above all is the deposition technique used, that has not allowed the achievement of a very sharp D/A interface. As a consequence, the dipole size and lifetime does not fulfill the requirement of the model. Moreover, absorption spectra, bilayers and dielectric spacing are not optimized as well [31].

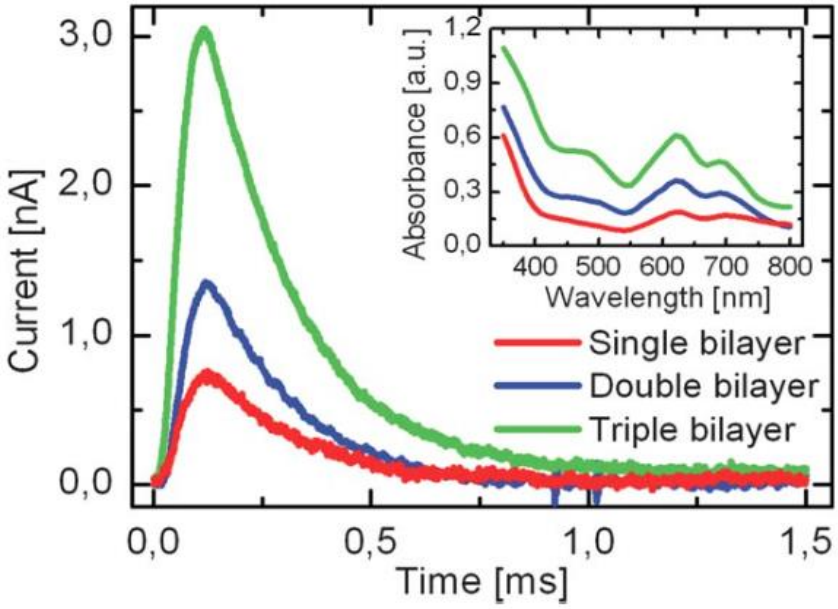


*Figure I.17 Evolution of the measured current for three devices with respectively one, two and three active bilayers. Inset: the absorption spectra for the three devices [31].*

With this final paragraph, the introduction to the master thesis project is complete. The next chapter will focus on the development of a physical model and on some MATLAB simulations. This is done to better explain the LHC working principle and to simulate the different dependences of the overall system.

# Bibliographic References

[1] BP, “BP Statistical Review of World Energy About this review Contents,” no. June, pp. 1–48, 2013.

[2] G. Hardin, “The Tragedy of the Commons Author ( s ): Garrett Hardin Published by : American Association for the Advancement of Science Stable URL : http://www.jstor.org/stable/1724745,” vol. 162, no. 3859, pp. 1243–1248, 2017.

[3] IEA, “Key World Energy Statistics 2016,” *Statistics (Ber).*, p. 80, 2016.

[4] N. Armaroli and V. Balzani, “Part One Living on Spaceship Earth,” 2011.

[5] B. Sorensen, “History of, and Recent Progress in, Wind-Energy Utilization,” *Annu. Rev. Energy Environ.*, vol. 20, no. 1, pp. 387–424, 1995.

[6] N. Armaroli and V. Balzani, “Part Four Renewable Energies,” 2011.

[7] G. Porter, *“Solar Heat and Electricity “*. 2011.

[8] D. M. Chapin, C. S. Fuller, and G. L. Pearson, “A new silicon p-n junction photocell for converting solar radiation into electrical power [3],” *J. Appl. Phys.*, vol. 25, no. 5, pp. 676–677, 1954.

[9] Y. Kanai, J. B. Neaton, and J. C. Grossman, “Theory and Simulation of Nanostructured Materials for Photovoltaic Applications,” *Comput. Sci. Eng.*, vol. 12, pp. 18--27, 2010.

[10] S. J. Fonash, “Introduction,” *Sol. Cell Device Phys.*, pp. 1–5, 1981.

[11] Adolf Goetzberger, Joachim Knobloch, Bernhard VoS, “Crystalline Silicon Solar Cells,” pp. 49–65.

[12] J. Zhao, A. Wang, and M. A. Green, “High-efficiency PERL and PERT silicon solar cells on FZ and MCZ substrates,” *Sol. Energy Mater. Sol. Cells*, vol. 65, no. 1, pp. 429–435, 2001.

[13] T. M. Razykov, C. S. Ferekides, D. Morel, E. Stefanakos, H. S. Ullal, and H. M. Upadhyaya, “Solar photovoltaic electricity: Current status and future prospects,” *Sol. Energy*, vol. 85, no. 8, pp. 1580–1608, 2011.

[14] B. Applications, “High Efficiency III - V Solar Cells : 목차,” pp. 417–448, 2010.

[15] Soitec, “New world record for solar cell efficiency at 46%,” pp. 12–15, 2014.

[16] N.J. Ekins-Daukes, “III-V Solar Cells,” 2014.

[17] C. W. Tang, “Two-layer organic photovoltaic cell,” *Appl. Phys. Lett.*, vol. 48, no. 2, pp. 183–185, 1986.

[18] B. Kippelen and J.-L. Brédas, “Organic photovoltaics,” *Energy Environ. Sci.*, vol. 2, no. 3, p. 251, 2009.

[19] C. Deibe, T. Strobe, and V. Dyakonov, “Role of the charge transfer state in organic donor-acceptor solar cells,” *Adv. Mater.*, vol. 22, no. 37, pp. 4097–4111, 2010.

[20] Y. Yang and G. Li, *Progress in High- Efficient Solution Process Organic Photovoltaic Devices*. 2015.

[21] S. Barbara and S. Kivelson, “Polymers,” 1988.

[22] N. Hall, “Twenty-five years of conducting polymers,” *Chem Commun*, no. 1, pp. 1–4, 2003.

[23] H. Shirakawa, “Nobel Lecture: The discovery of polyacetylene film—the dawning of an era of conducting polymers,” *Rev. Mod. Phys.*, vol. 73, no. 3, pp. 713–718, 2001.

[24] H. S. Nalwa, “Handbook of organic conductive molecules and polymers,” *Handb. Org. Conduct. Mol. Polym.*, p. 87, 1997.

[25] S. Hayase, “Organic Electronics Materials and Devices,” 2015.

[26] G. Yu, J. Gao, J. C. Hummelen, F. Wudl, and A. J. Heeger, “Polymer Photovoltaic Cells : Enhanced Efficiencies via a Network of Internal Donor- Acceptor Heterojunctions Author ( s ): G . Yu, J . Gao, J . C . Hummelen, F . Wudl and A . J . Heeger Published by : American Association for the Advancement of Science,” *Science (80-. ).*, vol. 270, no. 5243, pp. 1789–1791, 1995.

[27] C. J. Brabec, S. Gowrisanker, J. J. M. Halls, D. Laird, S. Jia, and S. P. Williams, “Polymer-Fullerene Bulk-Heterojunction Solar Cells,” *Adv. Mater.*, vol. 22, no. 34, pp. 3839–3856, 2010.

[28] A. Furini, *SpringerBriefs in Molecular Science*. 2013.

[29] R. Volpi and M. Linares, “*Organic solar cells*” .

[30] J. Nelson, J. O. E. J. Kwiatkowski, J. Kirkpatrick, and J. M. Frost, “Modeling Charge Transport in Organic Photovoltaic Materials Introduction,” *Acc. Chem. Res.*, vol. 42, no. 11, 2009.

[31] M. Garbugli *et al.*, “Light energy harvesting with nano-dipoles,” *Nanoscale*, vol. 4, no. 5, p. 1728, 2012.

[32] D. M. All, “Fundamentals of Pyroelectric Materials,” pp. 1–17.

# Chapter II. Device Simulations

The focus of this chapter will be to first develop a physical model based on the one reported in the LHC paper mentioned above. This model will allow the explanation of the device working mechanism and the prediction of efficiency values. The model will then be applied to a single bi-layer device under incident monochromatic light. The second step will be the stacking of several bi-layers introducing a Lambert-Beer model for the progressive absorption phenomenon. Again, the efficiency will be calculated under incident monochromatic light. Finally, to obtain more realistic efficiency values, a sun radiation model will be developed and combined with the absorption spectra for the donor material. With the final simulation ready, the effect of changing different parameters will be presented.

## II.1 Physical Model

To have a better understanding of the LHC working principle and to predict efficiency values, a physical model has been developed. The key point is to consider the device as a capacitor which is charged by solar radiation. The macroscopic polarization derives from the nano-dipoles formation and orientation in the active bi-layer that will then lead to energy storage as shown in figure II.1.

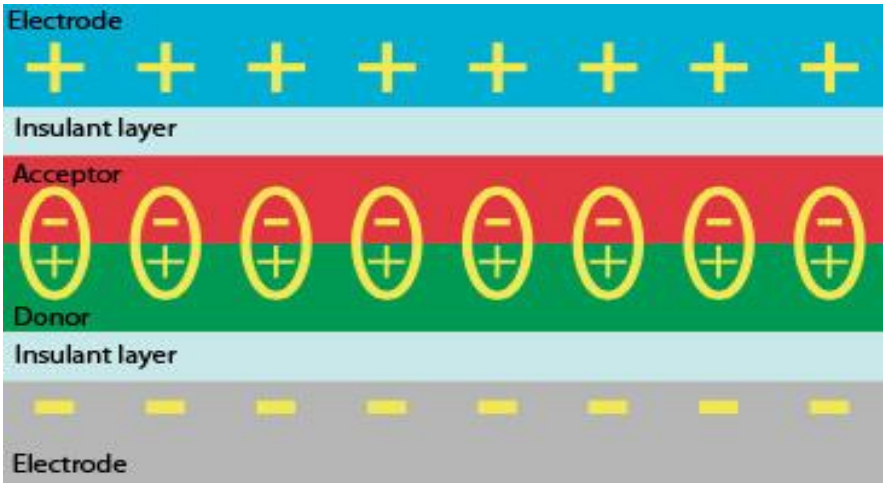


*Figure II.1 View of dipoles orientation and overall resulting polarization.*

The first step is to express the evolution of the dipoles volumetric concentration $S$ in the active bi-layer, when the device is under illumination. This can be done with an ordinary differential equation:

$$\frac{dS(t)}{dt} = \frac{\alpha\phi_{ph}}{d} - \frac{S(t)}{\tau}$$

*Eq. II-1*

where $\alpha$ is the absorption coefficient, $\phi_{ph}$ [1/m²*s] is the incident photon fluency rate, $d$ [m] is the bi-layer thickness and $\tau$ [s] is the characteristic decay time of the dipole. Solving equation II.1 leads to the direct time dependence of the volumetric concentration:

$$S(t) = \frac{\alpha\phi_{ph}\tau}{d}\left(1 - e^{-t/\tau}\right)$$

*Eq. II-2*

Once this specific quantity is known and an average dipole size $a$ [m] is introduced, the potential difference $V_p$ [V] arising across the photoactive layer is then derived as follow:

$$V_p = Fd = \frac{\sigma}{\varepsilon_0}$$

*Eq. II-3*

$$\sigma = eaS(t)$$

*Eq. II-4*

$$V_p(t) = ea\frac{d}{2}\left(\frac{1}{\varepsilon_d} + \frac{1}{\varepsilon_a}\right)S(t)$$

*Eq. II-5*

where $\sigma$ [C/m²] is the surface charge density, $F$ [V/m] is the electric field, $e$ [C] is the fundamental charge, $\varepsilon_d$ [F/m] and $\varepsilon_a$ [F/m] are respectively the dielectric permittivity of the donor and the acceptor material that must be multiplied by the vacuum permittivity $\varepsilon_0$[F/m]. The stored energy in every single-layer, based on the capacitance C is then:

$$E_p = \frac{1}{2}CV_p^2$$

*Eq. II-6*

$$C = A\left(\frac{d}{2\varepsilon_a} + \frac{d}{2\varepsilon_d} + \frac{2h}{\varepsilon_r}\right)^{-1}$$

*Eq. II-7*

introducing $h$ [m] and $\varepsilon_r$ [F/m] as respectively the thickness and the dielectric permittivity of the insulant layers that again must be multiplied by $\varepsilon_0$[F/m]. Once the stored energy is calculated, both the internal and the external energy conversion efficiency of the LHC can be promptly computed:

$$\boldsymbol{\eta_{ext}(t)} = \frac{E_p(t)}{E_{light}(t)}$$

*Eq. II-8*

$$\boldsymbol{\eta_{int}(t)} = \frac{E_p(t)}{AbsE_{light}(t)} = \frac{\eta_{ext}(t)}{Abs}$$

*Eq. II-9*

where $E_{light}(t) = AP_{sun}$t, $P_{sun}$ [W/m$^2$] is the incident light intensity, A [m$^2$] is the area of the device, $t$ [s] is the charging time and Abs is the fraction of the incident spectrum which is absorbed. With these considerations both the efficiencies are time dependent since the charging process itself is not linear. It has been chosen to consider the efficiency at 95% of the charging process, which in turn defines a time $t' = \tau(ln20)$ that will be used in the computation to obtain $\eta_{int}(t')$ and $\eta_{ext}(t')$ [1].

To have a better understanding on how to improve those efficiency values, the overall dependence on the several parameters is also shown ($\varepsilon_d$ and $\varepsilon_a$ are considered to be the same):

$$\boldsymbol{\eta_{ext}(t')} = \frac{1}{2}\boldsymbol{\alpha^2 P_{sun}}\left(\frac{\boldsymbol{\lambda}}{\boldsymbol{hc}}\right)^2 \frac{\boldsymbol{0.95^2 \tau d (ea)^2}}{\boldsymbol{ln20\varepsilon_{a/d}}} \frac{1}{\left(\frac{\boldsymbol{d}}{\boldsymbol{\varepsilon_{a/d}}} + \frac{\boldsymbol{2h}}{\boldsymbol{\varepsilon_r}}\right)}$$

*Eq. II-10*

The parameters directly related to the device are reported in red. To actually improve the efficiency there are several options, as increasing the material absorption or the dipole size. However, those ways just mentioned are not easy to exploit and that is why in the following simulations a third option has been mainly studied. Working on the insulant layers does not affect the charging process itself, but only the final capacitance of the LHC and, as consequence, it is the safest and easiest way to improve the device efficiency. More in details, both the thickness and the dielectric constant will be changed.

A new kind of high-k materials have recently been introduced in the production of transistors to decrease their final size and some of them will be used in this master thesis work. The great advantage of these materials is that having a permittivity constant much higher than normal insulator (like PMMA or Silicon oxide), allows the decrease of the layer thickness down to few nanometers without losing the insulating behavior. Some of them are reported in table II.1 [2].

*Table II.1 Table showing the permittivity constant of both some classical and high-k materials.*

| Material | Permittivity ($\varepsilon_r$) [F/m] |
|---|---|
| $SiO_2$ Silicon dioxide | 4 |
| $Al_2O_3$ Aluminum oxide | 9 |
| $ZrO_2$ Zirconium dioxide | 25 |
| $HfO_2$ Hafnium dioxide | 25 |
| $TiO_2$ Titanium dioxide | 80 |
| PMMA Poly-methyl-methacrylate (polymer) | 4 |

In this master thesis work, zirconium dioxide is the one that will be exploited first as an insulant layer, having it a $\varepsilon_r$ as high as 25 [F/m] and a high enough energy gap. After $ZrO_2$ titanium dioxide will be tried as well. Even though based on his $\varepsilon_r$ (80 [F/m]) $TiO_2$ looks even more promising, his bandgap is too low and this is why it is not usually employed as an insulator in transistors production. However, in the LHC case, the insulant behavior does not need to be very strong and this bandgap might be enough to prevent the charge carriers from flowing to the electrode. Some preventive studies will be done to understand better the behavior of the titania layer within the device.

Other device parameters considered in all the models are the dielectric constant of a D/A couples, namely copper phthalocyanine ($\varepsilon_r$=2.5 [F/m]) [3] and fullerene ($\varepsilon_r$=4 [F/m]). The studied thickness of the active bi-layer is 40 nm. This thickness has been chosen in order to be in the range of the exciton diffusion length which is usually around 25 nm. The insulant layer thickness, instead, is taken as 100 nm for the spin-coated PMMA during the model development and will then be changed in the later sections. The device area is 25 $mm^2$ and finally the characteristic decay time and the average dipoles size are considered to be respectively 10 ms and 4 nm. The effect of changing these last two parameters, that are much more relevant for the device performance but more difficult to control, will be shown at the end of this chapter.

## II.2 Monochromatic light

The two models to be presented in this part are the ones where the incident light is considered to be monochromatic. This approximation is quite far from the reality, but it nonetheless allows to obtain a primary rough prediction of the device efficiency. In these models, the incident power intensity is taken as 100 $mW/cm^2$, which is also the same that will be used later when modelling the sun spectrum. The chosen wavelength is 620 nm, which corresponds to the expected absorption peak of the donor material (CuPc), and the absorption coefficient itself is considered to be 10%.

## II.2.1 Single-layer device

The first model reported, which is also the easiest, represents the single-layer LHC efficiency under monochromatic red light. The parameters considered are the ones previously stated and the efficiencies obtained are reported in table II.2. These efficiencies values are not too high, since the device it is not optimized yet and only a single-layer is considered in this simulation, nonetheless it is possible to observe as the light harvesting capacitors are promising indeed.

*Table II.2 Single-layer LHC internal and external efficiencies.*

| Insulant Layer Material | Internal Efficiency | External Efficiency |
|---|---|---|
| PMMA | 11.4% | 1.1% |

## II.2.2 Multi-layer device

As already anticipated in chapter I, the addition of more active bi-layers to the architecture does not alter the device working mechanism. Since charge transport is not an issue anymore, the effect of adding more D/A layer is to increase the overall absorption and polarization, increasing as consequence the final efficiency as well. To model the absorption in each subsequent layer, the Lambert-Beer absorption law was used. The absorption coefficient $\alpha$ is taken as 10%, as for the single-layer device. More in details the equations proposed in paragraph II.1 have to be modified accordingly to those new assumptions:

$$S_i(t) = \frac{\alpha \phi_{ph} \tau}{d} \left(1 - e^{-t/\tau}\right)$$

*Eq. II-11*

$$V_{p,i}(t) = ea\frac{d}{2}\left(\frac{1}{\varepsilon_d} + \frac{1}{\varepsilon_a}\right) S_i(t)$$

*Eq. II-12*

$$V_{ptot} = \sum_{i=0}^{n} V_{p,i}$$

*Eq. II-13*

$$C = A\left(n\left(\frac{d}{2\varepsilon_a} + \frac{d}{2\varepsilon_d}\right) + (n+1)\frac{2h}{\varepsilon_r}\right)^{-1}$$

*Eq. II-14*

$$E_p = \frac{1}{2} C V_{ptot}^2$$

*Eq. II-15*

where the subscript $i$ refers to each bi-layer, $n$ is the total number of bi-layers and $V_{ptot}$ [V] is the overall potential difference across the device. According to the Lambert-Beer law, each following layer will receive 10% less energy than the previous one, due to the subsequent absorption phenomenon. The obtained simulated values for the external and the internal efficiency are reported in the figure II.2 for both the devices.

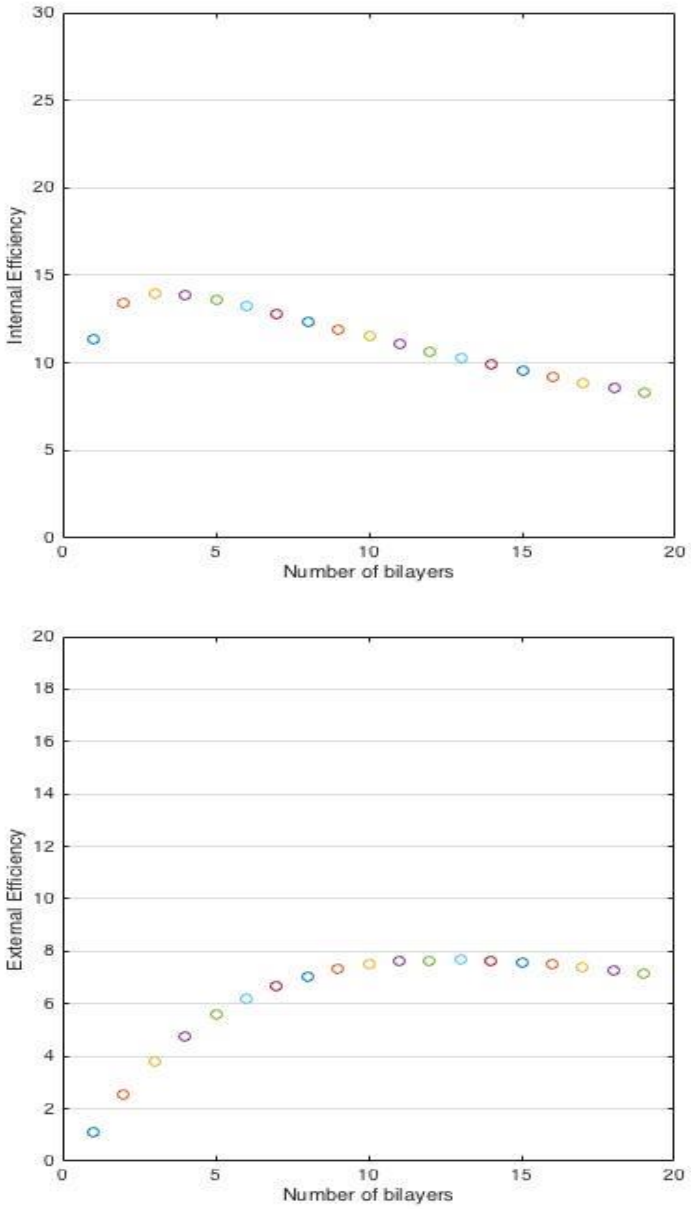


*Figure II.2 Simulated internal and external efficiencies for the multi-layer device.*

The simulated efficiencies values obtained are as high as 7.7% (achieved at 13 layers) for the external and 14.2% (achieved at 3 layers) for the internal one. Although these values have been obtained under monochromatic light and they will definitely be lower under real operating condition, it must be specified once again that the device is not optimized yet. Nevertheless, the improvement obtained by simply stacking more layers is rather relevant. It can also be observed that both the two efficiency trends reach a limit after which they start decreasing again for a further increase of the bi-layers number. That is due to the competition between two phenomena: the decrease in the capacitance of the device and the increase in the potential difference.

Since $V_{ptot}$ is a quadratic term, it should dominate over the decrease in capacitance leading to an unlimited increase in efficiency when stacking more and more thin films. However, since each subsequent layer receives less light radiation than the previous one, it also affects less the overall polarization. When adding an additional layer and the increase in $V_{ptot}$ is smaller than the decrease in the capacitance $C$, the efficiency starts to decrease [1].

With these considerations ends the part of this second chapter dedicated to the monochromatic light simulation. The following step will be the development of a solar spectrum model, based on the black body theory and of an absorption model for the simulated material.

## II.3 Sun spectrum simulation

As already mentioned before, the previous simulation is quite far from the reality. In fact, when a solar energy harvesting device is in operating condition, it is shined with several different wavelengths with different intensity. Moreover, each of the incidence wavelengths is absorbed with a different efficiency depending on the material utilized in the device fabrication process. This is the reason why a simulation accounting for only monochromatic light will not give a good prediction.

In this third part of chapter II, to get closer to reality with the efficiency results, a sun spectrum simulation was implemented in the model. In order to do so, two are the new sections that need to be introduced: the sun radiation itself and the material absorption spectrum.

### II.3.1 Black body radiation

To simulate the sun radiation, a black body spectrum is considered. The realization of this part of the model is based on the Planck's Law where the emissivity is considered to be 1.

$$I(\lambda,T) \approx B(\lambda,T) = \frac{2hc^2}{\lambda^5}\frac{1}{e^{\frac{hc}{\lambda k_b T}}-1}$$

*Eq. II-16*

where $h$ [J*s] is Planck constant, $c$ [m/s] is the speed of light, $k_b$ [J/K] is Boltzmann constant, $T$ [K] is the absolute temperature and $\lambda$ [m] is the wavelength. The formula is actually used to obtain the spectral radiance $B\ (\lambda,T)$ W/(sr*m$^3$)] but, considering the average distance Sun-Earth and the dimension of the Earth itself, it is possible to approximate the spectral radiance with the intensity per unit wavelength $I\ (\lambda,T)$ [W/m$^3$].

Since the temperature on the sun surface is around 5800 K, this is also the temperature used in the model. The plotting of the above equation as a function of $\lambda$ is shown in figure II.3.

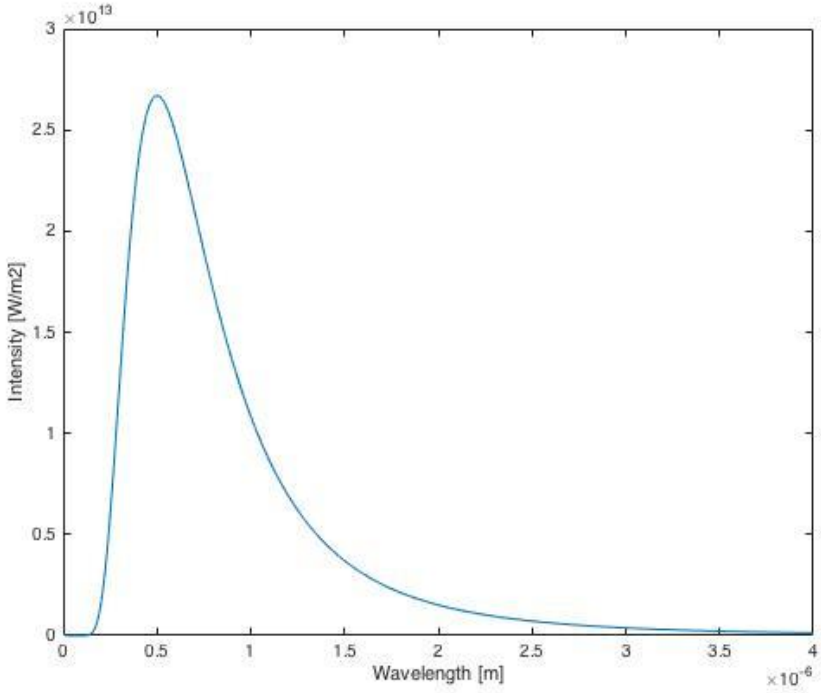


*Figure II.3 Simulated black body spectrum at 5800 K.*

The sun radiation intensity hitting the Earth surface is generally considered to be 100 mW/cm$^2$. That is why a final correction for the black body model is necessary to account for all the dissipations occurring due to the atmosphere. To obtain the final intensity value, the results of the integration over the whole wavelength range of the Planck's law is multiplied by 4.92*10$^{-5}$ [4].

## II.3.2 Absorption spectrum

Once the radiation spectrum is obtained, the following step is to implement an absorption spectrum to determine how much of the incident radiation is actually absorbed. In order to do so a Gaussian profile is assumed as follow:

$$\alpha_i(\lambda) = d\alpha_{i,0}\exp(-\frac{(\lambda - \bar{\lambda}_i)^2}{2\sigma_i^2})$$

*Eq. II-17*

where $\alpha_i$ is the absorption coefficient itself, $d$ [m] is the layer thickness, $\alpha_{i,0}$ [1/m] is the absorption coefficient at $\bar{\lambda}_i$ [m] which is where it reaches is maximum value, $\sigma_i$ [m] determines the width of the distribution and finally $i$ represents the different materials that can be used as active layer. In this MATLAB simulation a CuPc 20 nm thick active layer has been chosen, $\alpha_0$ is considered to be $10^7$ 1/m while $\bar{\lambda}_i$ is set to 620 nm.

These assumptions are based on the real absorption spectrum of CuPc which was measured and that will be presented in later sections. In the real one another absorption peak at lower wavelength is actually present but, since the sun radiation is not very intense in the UV region, it was neglected to simplify the model. The result is reported in figure II.4.

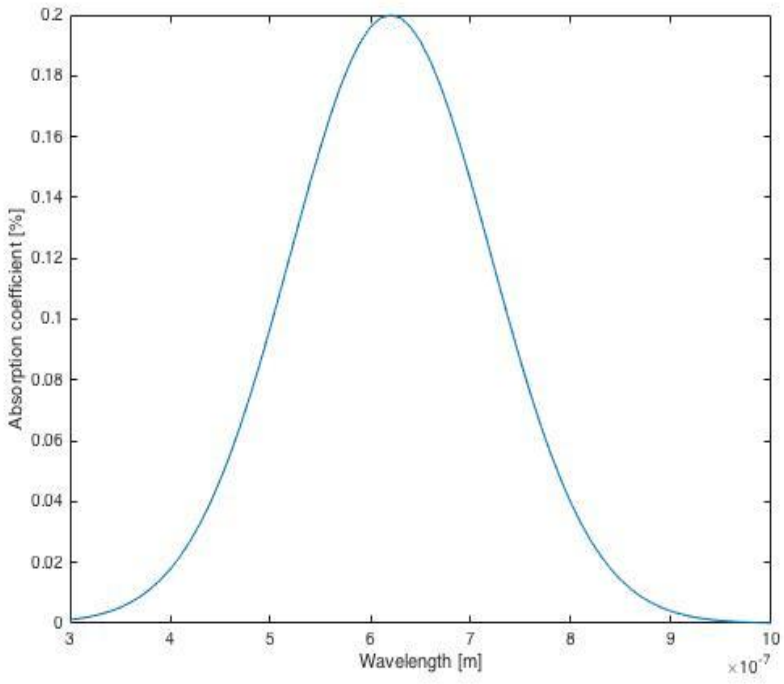


*Figure II.4 Simulated absorption spectrum for CuPc.*

## II.3.3 Multi-layer device

Now that these two premises have been made, the actual model can be developed. The progressive absorption is once again modeled with the Lambert-Beer law as in the monochromatic light case. This time however, each layer will absorb light according to the absorption spectrum introduced in the previous paragraph. Considering this, the formulas presented before were appropriately modified to evaluate the new efficiency values in the case of sun spectrum:

$$S_i(t) = \frac{\alpha(\lambda)\phi_{ph}(\lambda)\tau}{d}\left(1 - e^{-t/\tau}\right)$$

*Eq. II-18*

$$V_{p,i}(t) = ea\frac{d}{2}\left(\frac{1}{\varepsilon_d} + \frac{1}{\varepsilon_a}\right)S_i(t)$$

*Eq. II-19*

$$V_{ptot} = \sum_{i=0}^{n} V_{p,i}$$

*Eq. II-20*

$$C = A\left(n\left(\frac{d}{2\varepsilon_a} + \frac{d}{2\varepsilon_d}\right) + (n+1)\frac{2h}{\varepsilon_r}\right)^{-1}$$

*Eq. II-21*

$$E_p = \frac{1}{2}CV_{ptot}^2$$

*Eq. II-22*

where everything is basically the same as in paragraph II.2.2 except for $\alpha(\lambda)$ and $\phi_{ph}(\lambda)$ that are now a function of the wavelength. More in details $\alpha(\lambda)$ is the absorption spectrum introduced earlier, while the new photon fluency ratio $\phi_{ph}(\lambda)$ is simply taken as the black body spectrum intensity, divided by the photon energy $\frac{hc}{\lambda}$. To obtain the final number of absorbed photon $S_i$, the formula presented above needs to be integrated over the whole radiation spectrum. The same has to be done to obtain the total incident intensity which is necessary to calculate the efficiency values as shown from equation II.9 in paragraph II.1 and also reported as follow [1]:

$$\boldsymbol{\eta_{ext}(t)} = \frac{E_p(t)}{E_{light}(t)}$$

*Eq. II-23*

$$\boldsymbol{\eta_{int}(t)} = \frac{E_p(t)}{AbsE_{light}(t)} = \frac{\eta_{ext}(t)}{Abs}$$

*Eq. II-24*

The results for both the simulated internal and external efficiencies are reported in figure II.5 and II.6. It is possible to observe that the numbers obtained are definitely lower, when compared to the monochromatic case. This is expected because of poorer absorption which is closer to reality and which allows a more accurate prediction of the device actual behavior. However, the resulting efficiencies are nevertheless quite interesting. More in details the maximum values are 1.7% for the external efficiency, achieved at 10 layers, and 7.2% for the internal one, achieved instead at 3 layers.

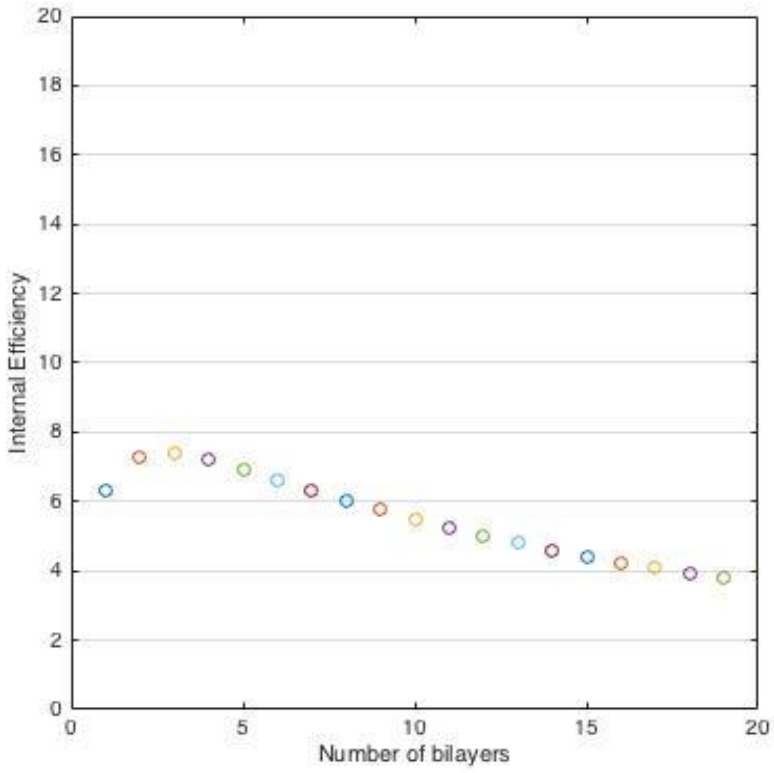


*Figure II.5 Simulated internal efficiencies for the multi-layer device in case of incident solar spectrum.*

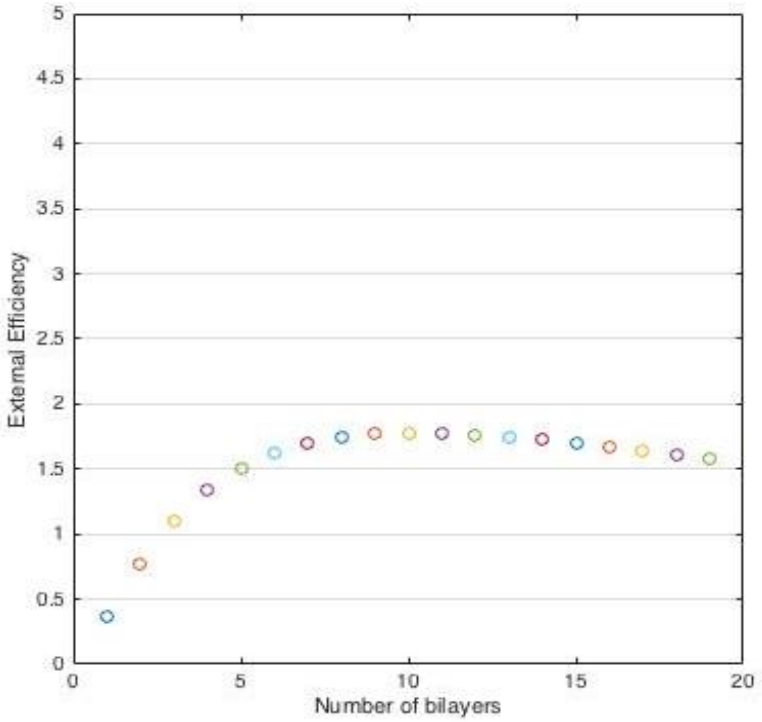


*Figure II.6 Simulated external efficiencies for the multi-layer device in case of incident solar spectrum.*

# II.4 Parameters dependency

With the actual model being developed, the influence of some of parameters reported in the overall efficiency dependency (equation II.10) can be studied. As already mentioned, the easiest way to improve the device is to work exclusively on the insulant layer. As a consequence, the next two paragraphs will be dedicated respectively to the insulant layer thickness and the dielectric constant dependency (namely changing from PMMA to $ZrO_2$ and $TiO_2$). In the last paragraph instead, the effect of changing the lifetime and the dipole size will also be shown, although affecting these parameters in the real device is not as simple.

## II.4.1 Insulant layer thickness

In this first paragraph the thickness dependency on the final external efficiency is studied. Specifically, three different thicknesses are reported for the PMMA insulant layer: 100 nm, 50 nm and 25 nm.
Figure II.7 shows the external efficiencies trend for the three options at the increasing number of bi-layers. It can be observed that the efficiency cap is always at 10 layers. These maxima are 1.78% for 100 nm,

2.70% for 50 nm and 3.63% for 25 nm. The improvement ratio is 1.5 when decreasing the thickness by half and 2.0 when decreasing it to a fourth of the original value. Since this master thesis aim is to work on the single-layer device, the respective efficiencies are also reported: 0.36%, 0.60% and 0.89%. It is worth noting that in this case the improvement ratios are higher, namely 1.7 when changing from 100 nm to 50 nm and 2.5 when passing from 100 nm to 25 nm. This is due to the fact that the capacitance is different in the 3 devices, meaning a different decrease when adding multiple layers.

A first and easy way to improve the efficiency by simply changing the insulant layer thickness was introduced. In the next paragraph the effect of changing the insulant material itself, and therefore the dielectric constant, will be simulated.

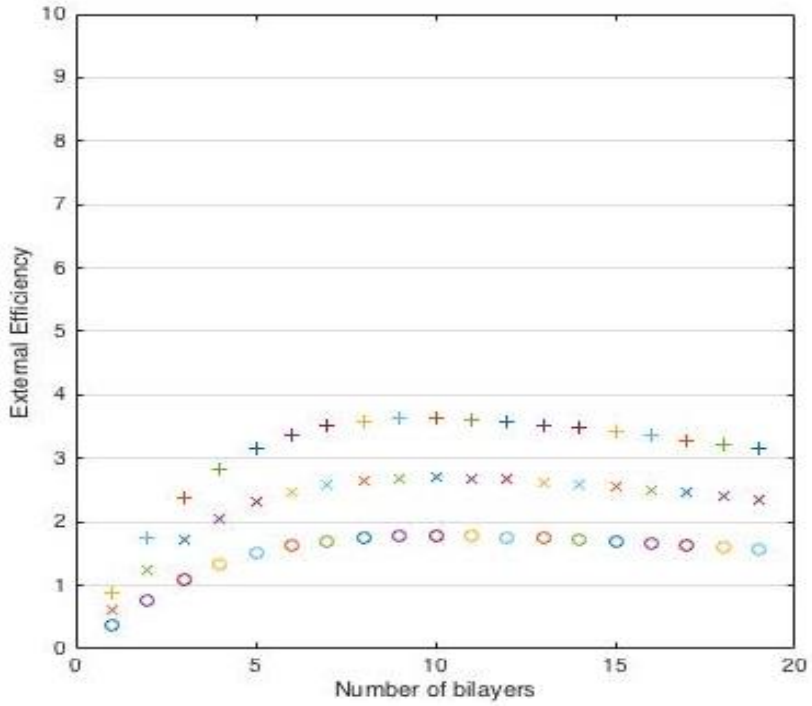


*Figure II.7 Simulated external efficiencies for the multi-layer device in case of incident solar spectrum at three different PMMA thicknesses. 'o', 'x' and '+' represent respectively 100 nm, 50 nm and 25 nm.*

## II.4.2 Insulant layer dielectric constant

As previously stated in paragraph II.1, new insulant materials with a very high K constant have been recently introduced in the production of transistors. In the following section the device simulation will be done for PMMA ($\varepsilon_r$=4) as a reference and for both Zirconium Dioxide ($\varepsilon_r$=25) and Titanium Dioxide ($\varepsilon_r$=80). The thickness considered is 25 nm since it leads to the highest efficiency out of the four simulated in the previous paragraph. The results are illustrated in figure II.8.

The respective maximum external efficiencies are 3.63%, 5.12% and 5.41%, achieved at 10 layers in the case of PMMA and at 9 layers for the other dielectric materials simulated. In this case the increase by more than 6 times of the $\varepsilon_r$ leads only to an improvement ratio of 1.4 and 1.5 when increasing it by 20 times. This is due to the fact that the capacitance considered is already quite high because of the small thickness used in the simulation (25 nm). Once again it is also meaningful to report the efficiency values for the simulated single-layer device: 0.89%, 1.52% and 1.67%.

Now that the effect of changing both the insulant layer parameters have been described, it is possible to combine them to optimize the dielectric layer itself. To conclude this chapter dedicated to device simulations, the consequences of changing the lifetime and the size of the dipoles will be shown.

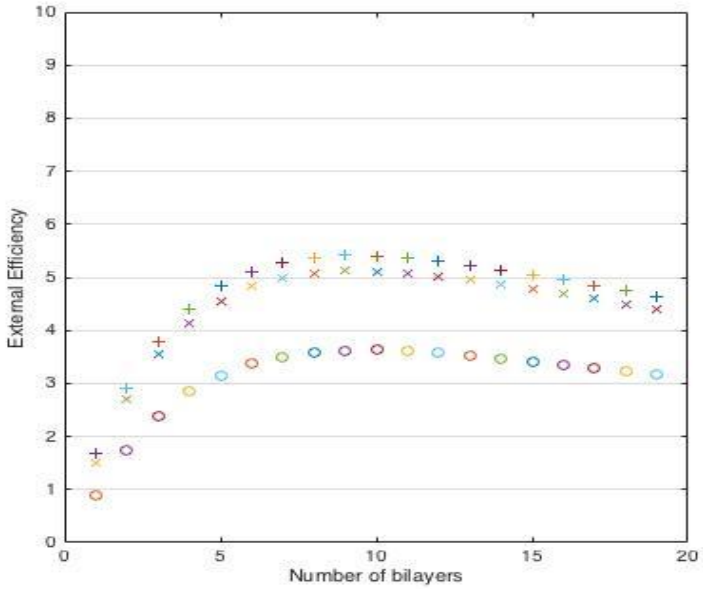


*Figure II.8 Simulated external efficiencies for the multi-layer device in case of incident solar spectrum for three different insulant materials. 'o', 'x' and '+' represent respectively PMMA, $ZrO_2$ and $TiO_2$.*

## II.4.3 Active layer parameters

Changing the parameters directly involved with the active materials is not as easy as with the dielectric layer. Moving from a donor molecule to another might completely change the behavior of the device itself, either in a positive or a negative way. This is why in the present work the active layer will be keep fixed. Nonetheless, since this is the way to increase the efficiency the most, it is interesting to try to simulate these effects. Both the lifetime ($\tau$) and the size ($a$) of the dipoles were varied in two different simulations in order to show the two separated outcomes. Since in the previous simulations the insulant layer made of 25 nm thick $TiO_2$ was the best out of all the others reported, it is also the one considered in this paragraph.

Figure II.9 reports the effect of changing the first of the two mentioned active layer parameters: the lifetime. The efficiency cap is at 9 layers in each of the cases and respective values for 1 ms, 10 ms and 30 ms are 0.54%, 5.41% and 16.24%. As already shown by equation II.10, the dependency in this case is linear. Further increase of the lifetime will lead to even better performances, but even for 30 ms, which is a reasonable decaying time value [5], the efficiency achieved is already quite promising. A possible way to affect $\tau$ is to make the interface between donor and acceptor as sharp as possible, to promote the charge separation and increase their stability as single charges.

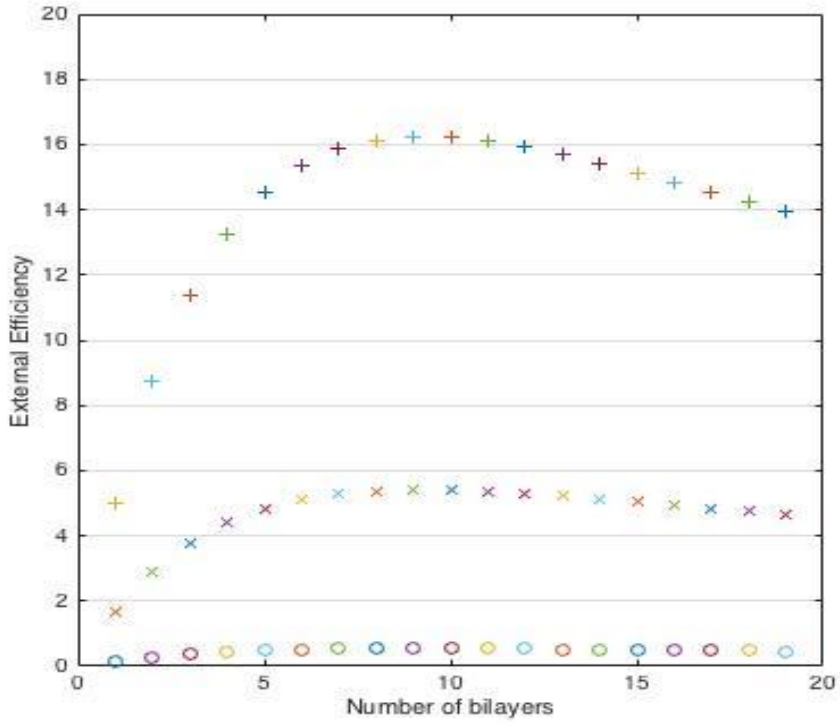


*Figure II.9 Device simulations for different lifetime of the photo-generated dipoles. 'o' is 1 ms, 'x' is 10 ms and '+' is 30 ms.*

It must be noted though, that varying the lifetime, also the charging time of the device itself changes. Namely, increasing $\tau$, the time required to reach the steady state increases. When working on a possible application it is worth to further analyze this trade-off between efficiency and charging time.

An even more impactful active layer parameter is the average size of the photo-generated dipole. In fact, this second factor enters squared in the overall efficiency formula (eq. II.10). Figure II.10 shows the results of the simulation. Once again, the efficiency cap occurs at 9 layers and the values range from 1.35% (1 nm) to 5.41% (4 nm) and 21.65% (8 nm). It is rather obvious that this is by far the best way to improve the device performance, however it is also the most difficult to control. Specifically, while in the case of the lifetime it is possible to obtain a rough idea of the actual $\tau$ value with some transient photo-induced absorption (PIA) experiments, measuring the average dipole size $a$ in the active layer is not so trivial [6].

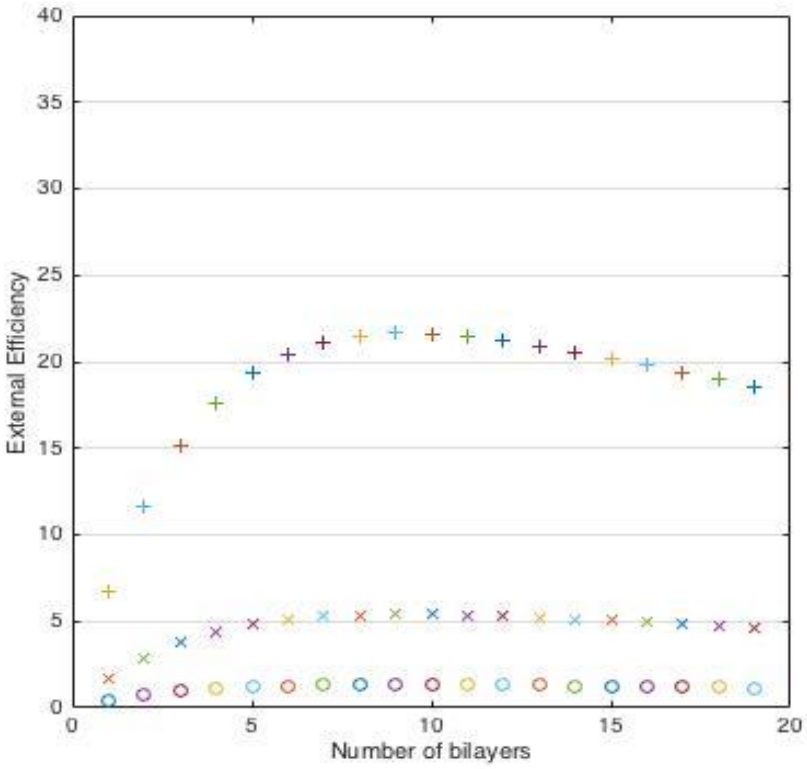


*Figure II.10 Simulated device efficiencies for different size of the photo-generated dipoles. 'o' is 2 nm, 'x' is 4 nm and '+' is 8 nm.*

A potential way to achieve an increase of $a$ may be obtained exploiting the huge dipoles moment that is found in the new hybrid-perovskites used in the case of normal PV. In the usual kind of devices this dipole moment caused by the organic cation is actually a problem. It has been observed that these cations take longer times to reorganize, affecting the electronic carrier dynamic. This leads to an undesired hysteresis cycle in the J-V curve. As already mentioned though, these extra dipoles moment might be helpful in the case of the light harvesting capacitor [7]. Finally, it must also be remarked that increasing the time before the recombination of separated charges ($\tau$), they are allowed to diffuse for longer distances hence influencing $a$ as well.

In this chapter, several simulations have been reported to better understand and to model the physics behind the working principle. The viability of the device itself has been theoretically proved and few options to improve the efficiency have also been introduced. In the next chapter the materials, the fabrication and characterization techniques used will be presented.

# Bibliographic References

[1] M. Garbugli *et al.*, "Light energy harvesting with nano-dipoles," *Nanoscale*, vol. 4, no. 5, p. 1728, 2012.

[2] H. L. Lu and D. W. Zhang, "Issues in High-k Gate Dielectrics and its Stack Interfaces," *High-k Gate Dielectr. C. Technol.*, pp. 31–59, 2012.

[3] H. Vázquez, W. Gao, F. Flores, and A. Kahn, "Energy level alignment at organic heterojunctions: Role of the charge neutrality level," *Phys. Rev. B - Condens. Matter Mater. Phys.*, vol. 71, no. 4, pp. 1–4, 2005.

[4] G. Toon, "The Solar Spectrum : an Atmospheric Remote Sensing Perspective," 2013.

[5] D. Taguchi *et al.*, "Analyzing carrier lifetime of double-layer organic solar cells by using optical electric-field-induced second-harmonic generation measurement," *Appl. Phys. Lett.*, vol. 98, no. 13, pp. 2009–2012, 2011.

[6] M. Vengris, "Introduction to time-resolved spectroscopy."

[7] R. S. Sanchez *et al.*, "Slow dynamic processes in lead halide perovskite solar cells. Characteristic times and hysteresis," *J. Phys. Chem. Lett.*, vol. 5, no. 13, pp. 2357–2363, 2014

# Chapter III. Experimental methods

The following chapter aims to present the materials exploited in this master thesis work, together with the fabrication and characterization techniques employed. The research has been focused on two active materials: copper phthalocyanine (CuPc) and fullerene ($C_{60}$). Both the active layers have been fabricated through thermal evaporation. On the other hand, the materials utilized for the insulant layers are several and they have been deposited with different techniques. The first one is Poly (methyl methacrylate) by spin-coating, the second one is zirconium dioxide by thermal evaporation and the last one is titanium dioxide by atomic layer deposition (ALD). The final purpose was to create and test a complete device, this is why after the fabrication process a special set up has been developed to study the efficiency.

## III.1 Materials

In this first paragraph, all the materials used in device fabrication for both the active and the insulant layers will be presented. First the acceptor and donor small molecules used for the dipoles generation and then the three dielectric materials exploited for the insulant films. Information about their physical and chemical properties will be given. Some common applications will be reported as well, together with the suppliers which they were purchased from.

### III.1.1 Active bi-layer

The materials used as active layers are CuPc and $C_{60}$ and both their structures are reported in figure III.1, together with the bandgaps of the most common materials used in OPV devices. Fullerene and its derivatives are the main class of materials used as acceptors for organic devices. As shown in the figure III.1, the molecule structure is basically a ball made of carbon atoms. Those carbon atoms are of the $sp^2$ kind, the same present in graphite. However, while the atoms in graphite are arranged with hexagonal structures only, in fullerene, pentagons are needed. Without pentagons, it would not be possible to achieve the curvature, hence, the spherical structure.

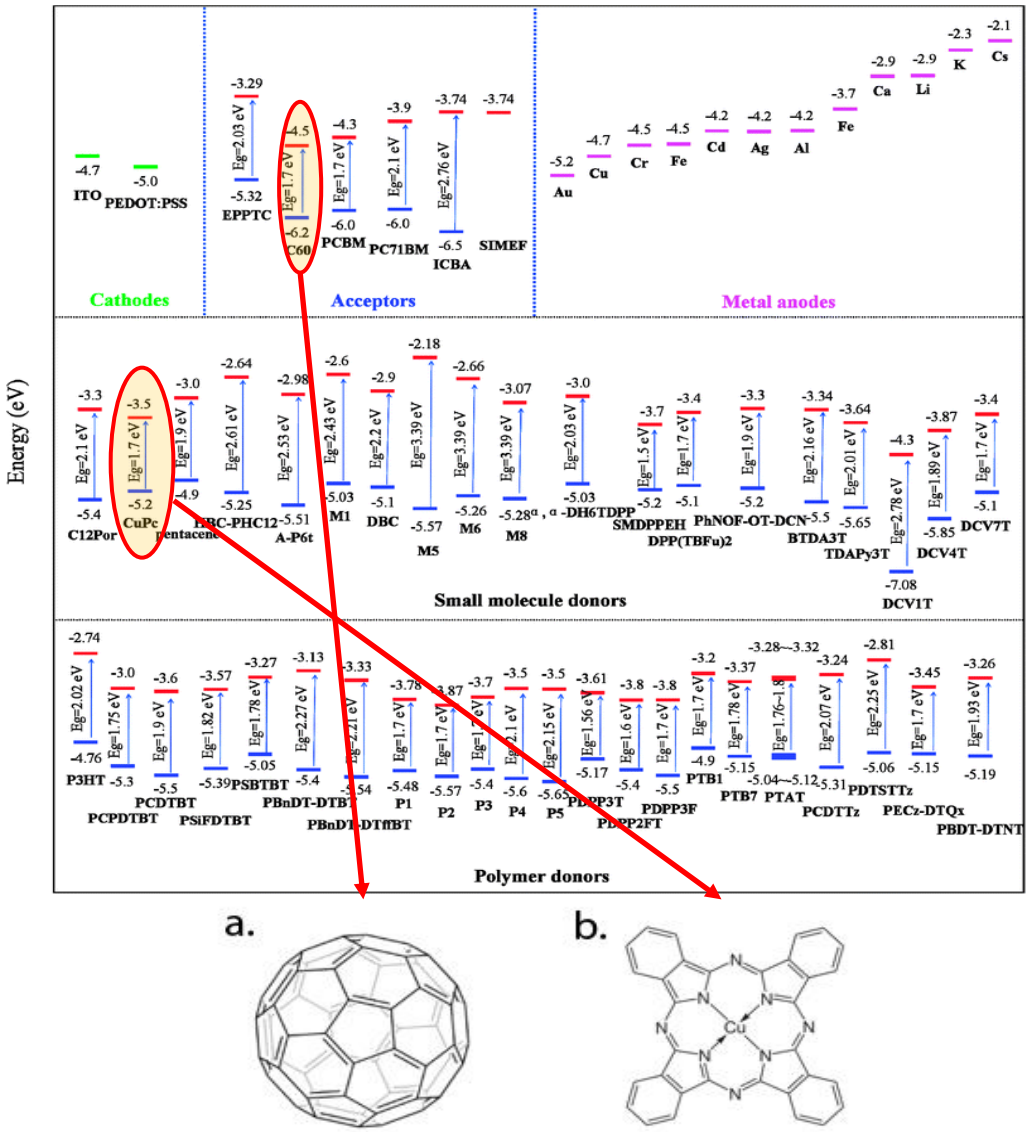


*Figure III.1 Band gaps of the most common materials used in OPV devices and chemical structures of fullerene (a) and copper phthalocyanine (b) [4,5].*

Usually a fullerene molecule with an organic chain attached is preferred, in order to have enhanced solubility and allow the molecule to be spin-coated [1]. In this case however, the interface donor/acceptor needs to be as sharp as possible to allow the dipoles formation and the thickness needs to be smaller than the diffusion length. For this reason, an evaporation procedure is preferred and that is why a simple $C_{60}$ molecule has been chosen. The fullerene powder, that appears black in color, was purchased from Sigma-Aldrich with a purity degree of 99.5%. Other parameters related to it are: a density of 1.6 g/cm$^3$, a dielectric constant of 4 F/m and a Z-factor (used to match the acoustic properties of the material with the sensor crystal during evaporation) of 3.45 [2]. Regarding the optical properties instead, fullerene mainly absorbs in the UV around 350 nm while in the visible range the absorption is rather low [3].

When it comes to organic donor material, as shown in figure III.1, the choice is much broader, ranging from conductive polymers to small molecules. Once again, thermal evaporation is the technique used and that is why another insoluble small molecule was chosen: copper phthalocyanine. Other alternatives could have been selected, but since the effect of changing them on the device properties is not clear yet, the one used in the reference paper [4] was designated. CuPc was also the molecules utilized in the first OPV milestone for the production of the single heterojunction solar cell. It is a metal complex between copper and phthalocyanine, which is instead classified as an aromatic macrocyclic compound. It was purchased from Sigma-Aldrich with a purity degree of 99% and it appears as dark blue flakes. In this case the density is 1.62 g/cm$^3$, the dielectric constant is 2.5 F/m [5] and the Z-factor is 15 [2]. Since the donor material is the one with the higher absorption properties in the visible range, when compared to the acceptor, it is also called the absorber and that is why the absorption spectrum obtained through the ellipsometer is reported here in figure III.2. It is possible to observe as CuPc presents two absorption peaks: one in the UV range at 350 nm and one in the visible range at 620 nm. The second one is clearly the one that matters for the solar device performance, since the solar spectrum is more intense in the visible range itself. The material shows an absorption peak of 40%, which is a rather good value for an absorber.

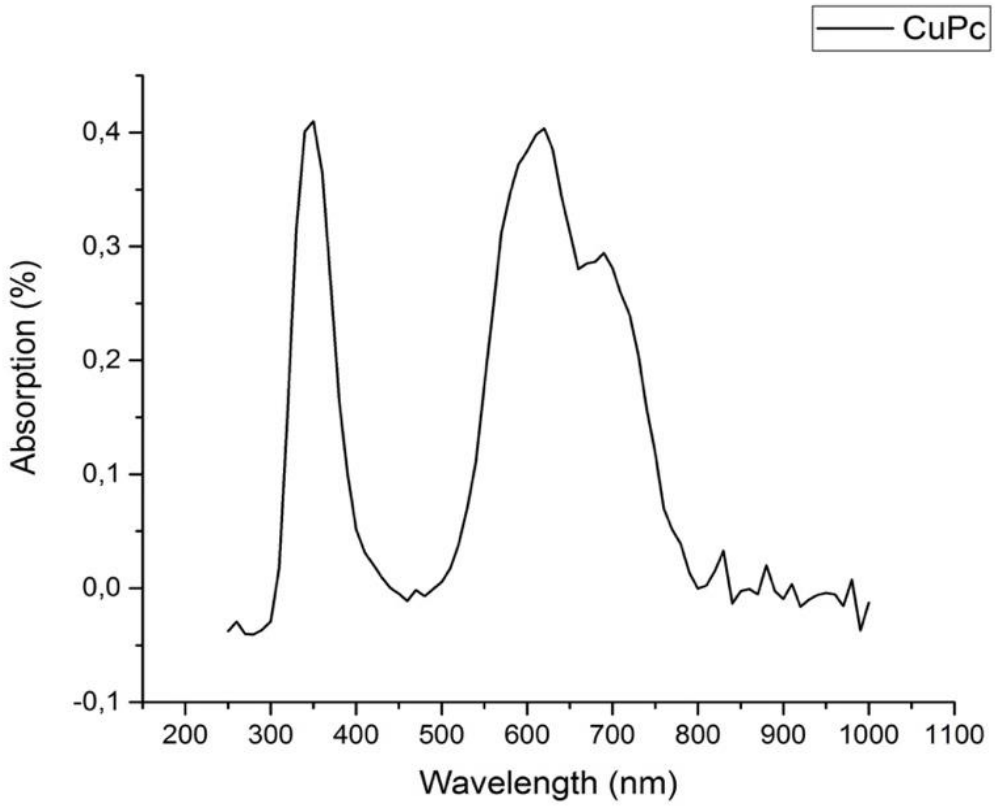


*Figure III.2 CuPc linear absorption spectrum.*

## III.1.2 Poly (methyl methacrylate)

Poly (methyl methacrylate), mostly known through its acronym PMMA, is a widely spread thermoplastic transparent polymer with a glass transition temperature in the range 105-120 °C. It is a chain-growth polymer obtained by free radical polymerization of its monomer methyl methacrylate and its structure is reported in figure III.3.

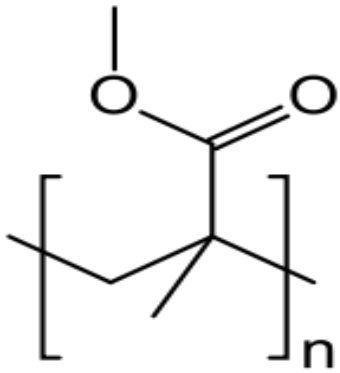


*Figure III.3 Chemical structure of PMMA [6].*

The polymer posseses strongly polar and flexible ether side chain attached to a non-polar backbone. Some of its most common solvents are chloroform, dichloromethane, toluene, benzene, butyl acetate and isobutyl ketone. Regarding the optical properties, PMMA is highly transparent in the visible and near-IR regions and its dielectric constant is 4 F/m. The bandgap is high enough to be chosen as one of the insulant materials to use in the LHCs fabrication. It was purchased from Sigma-Aldrich in the form of small pellets with an avarage molecular weight of 120000 g/mol [6].
It is often preferred to other transparent polymers due to the good balance between properties, usage and cost. Some possible applications range from glazing, to display and optical fibers, but also in more advanced fields like biomedicine.

## III.1.3 Zirconium dioxide

Zirconium dioxide, which is also called zirconia, is a white crystalline oxide of zirconium. It possesses three different crystalline phases (figure III.4) stable in three different temperature ranges: monoclinic, up to 1170 °C; tetragonal, between 1170 °C and 2370 °C; cubic, above 2370 °C. The density is 5.68 g/cm$^3$ and the melting point is 2700 °C. Given the very high temperature needed, thermal evaporation of this

material is not easy and requires a rather thick tungsten boat. It is characterized by a band gap as high as 5.8 eV and that is why it was chosen as the second insulant material to try. For this reason, it is highly transparent in the visible and IR-region. The dielectric constant is 25 F/m which classifies it as one of the new high-K materials, as already explained in chapter II [7]. Since the thin films fabrication technique is once again thermal evaporation, it was purchased as small pellets, white in color, from Kart J. Lesker company.

The main applications for zirconia are in the production of hard ceramics, both for abrasives and refractories. It is also widely used as a electroceramics and, being it totally biocompatible with the human body, it can also be used in prostheses production. Finally, if calcium or yttrium oxides are added, it can be stabilized in the cubic form, and can be used as a diamond simulant [8].

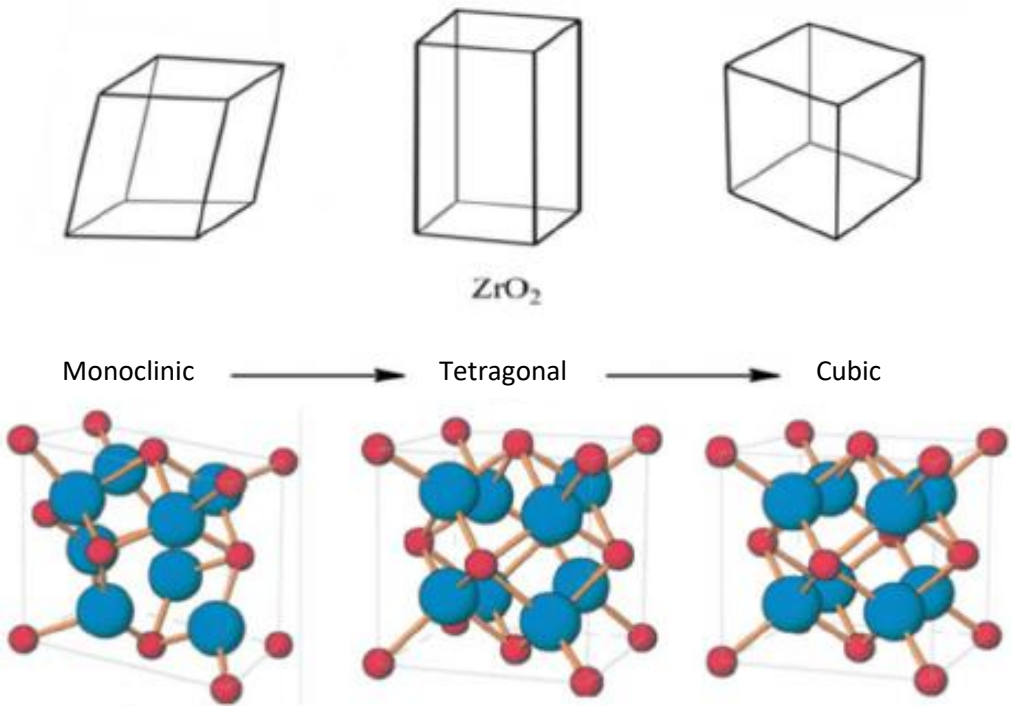


*Figure III.4 A representation of the three crystalline phases of zirconium dioxide [8].*

## III.1.4 Titanium dioxide

Titanium dioxide, also known as titania or titanium(IV) oxide, is one of the possible oxides of titanium and it appears white in color. It possesses several different crystalline phases, but the main ones are three: rutile, anatase and brookite. The first two are the most used and present a tetragonal structure, while the third one is orthorhombic. Both anatase and brookite are metastable and will eventually turn back into rutile, the crystalline structure of which is reported in figure III.5.

The density of rutile is 4.23 g/cm$^3$ and its melting point is 1843 °C. Regarding the optical properties, it presents a bandgap of 3.05 eV which is small enough to classify it as semiconductor and not as an insulant anymore. However, given the extremly high dielectric constant (80 F/m), it has still been chosen as one of the insulant material to try in the LHCs fabrication, since the insulant behaviour needed should not be too strong [7]. Some preventive studies will be done on this kind of material. Concerning the production technique, in this case atomic layer deposition (ALD) was chosen to try to obtain an even higher control during the fabrication process. More details will be presented in the following paragraph.

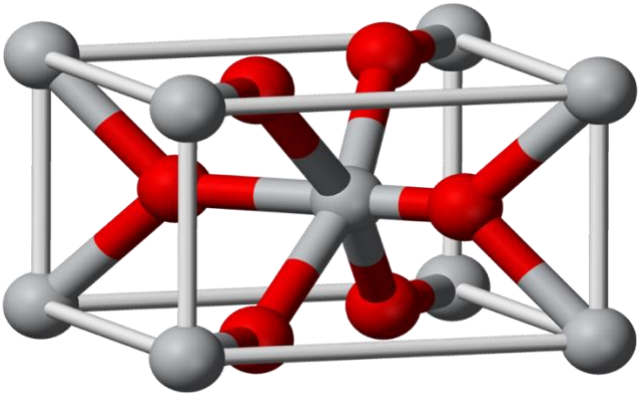

*Figure III.5 Crystalline structure of rutile [9].*

The most common application for titanium dioxide is as a white pigment for food, beverage and cosmetics, given the high refractive index. Another common one is as bones prostheses, due to the formation of hydroxyapatite that promotes the integration with the bone itself. Moreover, specifically to anatase, it can also be used for its photo-induced properties in the self-cleaning and photocatalytic application. Finally, it is also utilized in photovoltaic devices as electron transport layer, mainly with perovskites, or in its mesoporous form, in the so-called dye-sensitized solar cells [9].

## III.2 Fabrication techniques

In this second paragraph, all the fabrication techniques exploited will be illustrated starting from the spin-coating. The second one will be the thermal evaporation that was the most used process during the whole master thesis project. Since it was used to deposit new materials, it required a calibration process that will be also reported in this paragraph. Atomic layer deposition is the last one to be presented. To conclude the paragraph, the overall fabrication process for one device, including all the single and subsequent steps from cleaning to the gold electrode deposition, will be explained.

## III.2.1 Spin-coating

Spin-coating is a fabrication process that allows to deposit thin films on substrate in a quick and rather uniform way. The working principle is relatively simple as illustrated in figure III.6. An excess of solution is deposited on the substrate which is then rotated at high speed in order to spread the fluid via centrifugal force. During the rotation the solvent evaporates leaving a thin solid film of the desired material.

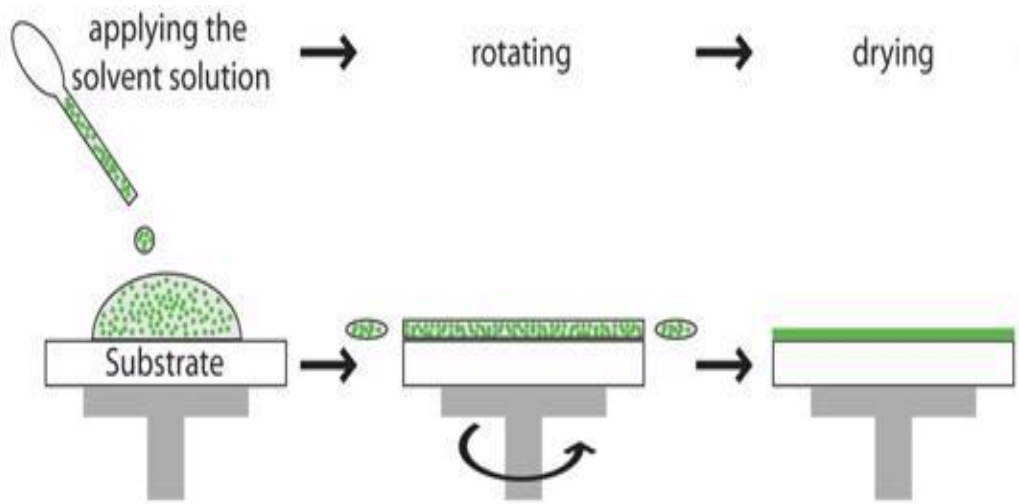


*Figure III.6 Schematic view of the spin-coating process.*

The final film thickness and quality depends on both the solution and rotation parameters. Concentratrion, drying rate and surface tension regard the first. More in details the wettability needs to be good enough to have a homogenous distribution of the film, while concentration affects the layer thickness. Increasing the concentration and so the viscosity, the final thickness obviously increases. On the other hand the effect of the drying rate is not that discernable. First of all, it is not easy to control since, even if it is true that it mainly depends on the solution, the air surrounding the substrate matters as well. Second, the quality of the film is the one being affected and not in a very predictable way. However, the effect of the drying rate is secondary when compared to the others parameters.

Rotational speed and acceleration are instead related to the spin-coating process itself. The first is directly related to the thickness: the higher the speed, the thinner the film. Acceleration instead affects other properties as well, but as in the case of the drying rate, the effect is not that easy to discern.

In the current work, a SCS 6800 Spin-Coater Series was used for the fabrication of the thin insulant layers of PMMA. Specifically, two different solutions were prepared: one for the bottom and one for the top layer. The first one was in toluene while the second one was in butyl acetate. The rotation parameters are set to 4000 rpm for 60 seconds with an “infinite” acceleration.

## III.2.2 Thermal evaporation

The most used fabrication technique during this project was thermal evaporation (schematic view in figure III.7). Although two different evaporators were used, one for organic and one for inorganic materials, the working principle is basically the same and will be only described once.

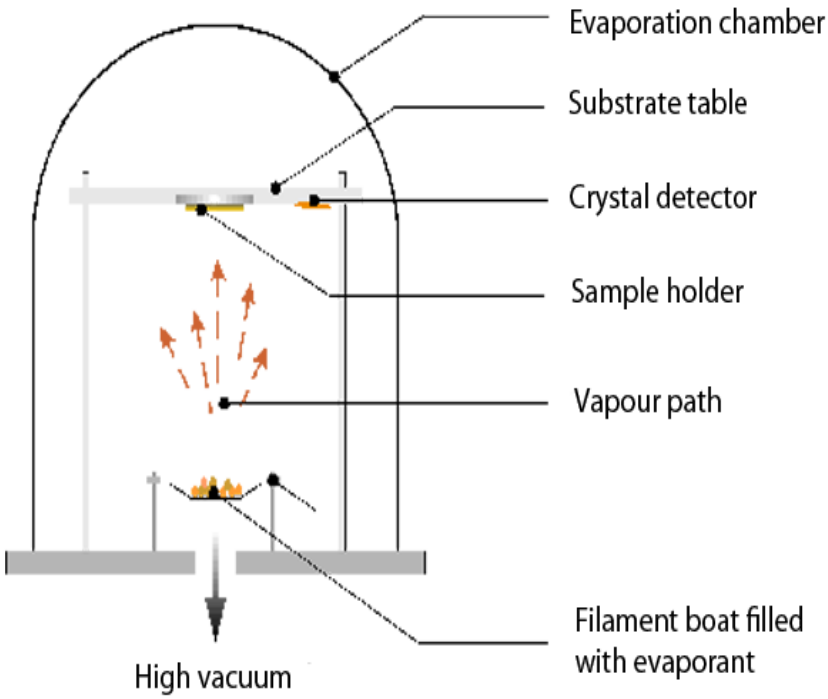


*Figure III.7 Schematic view of a thermal evaporator.*

This technique is part of the physical vapour deposition family (PVD), since no chemical reaction is involved in the process. The material to evaporate, usually in the form of a powder or small pellets, is placed inside a "boat". Depending on the material, different kinds of boat must be used: organic compounds require quartz boat, zirconium dioxide requires a thick tungsten boat and gold has no specific requirements. Once this is done, the material holder is positioned inside the machine in a way to close the electric circuit, so that the current may flow through it. Before turning on the machine, it is essential to bring the evaporation chamber in a vacuum level of $10^{-4}/10^{-5}$ Pa. This is necessary for two main reasons: firstly, any gas present in the evaporation chamber may contaminate the thin film; secondly, lower pressure means lower minimal evaporation temperature of the material. After the right vacuum level is reached, a potential is applied to the boat, leading to a current circulation and as a consequence, to the heating phenomenon. Different evaporants require different temperatures, which are controlled through

the applied voltage. The deposition rate and the film thickness during the whole process are measured via a crystal detector which is positioned near the sample holder. This crystal detector needs to be calibrated when a new material is being deposited.

The calibration is done by checking the actual film thickness and updating the so-called tooling factor (TF):

$$New\ TF = TF \times \frac{Actual\ thickness}{Desired\ thickness}$$

*Eq. III-1*

the procedure is repeated few times. During the first calibration process the starting tooling factor $TF$ is taken as 100%. The calibration processes done for CuPc, $C_{60}$ and $ZrO_2$ are reported here [10].

### *III.2.2.1 Thermal evaporation calibration*

Whenever a new material is deposited a few calibration steps need to be done in order to be sure of the final thickness obtained. Checking the film thickness can be done in several different ways, but in this case an atomic force microscope (AFM) has been used on a scratched film . The working principle of the microscope will be reported briefly in the following paragraph, but in the current one the focus will be on the calibration itself. The different thicknesses and the subsquent tooling factor for the considered materials are reported in table III.1, while figure III.8 shows some of the AFM measurements.

*Table III.1. Different calibration steps for CuPc, $C_{60}$ and $ZrO_2$.*

| Calibration n° | Material | TF [%] | Desired [nm] | Actual [nm] | New TF [%] |
|---|---|---|---|---|---|
| I | CuPc | 100 | 20 | 16 | 80 |
| | $C_{60}$ | 100 | 20 | 34 | 170 |
| | $ZrO_2$ | 100 | 40 | 45 | 113 |
| II | CuPc | 80 | 50 | 20 | 32 |
| | $C_{60}$ | 170 | 50 | 40 | 136 |
| | $ZrO_2$ | 113 | 20 | 24 | 135 |
| II | CuPc | 32 | 16 | 16 | 32 |
| | $C_{60}$ | 136 | 40 | 48 | 163 |
| | $ZrO_2$ | 135 | 50 | 50 | 135 |
| IV | CuPc | 32 | 30 | 30 | 32 |
| | $C_{60}$ | 163 | 30 | 30 | 163 |
| | $ZrO_2$ | 135 | 40 | 40 | 135 |

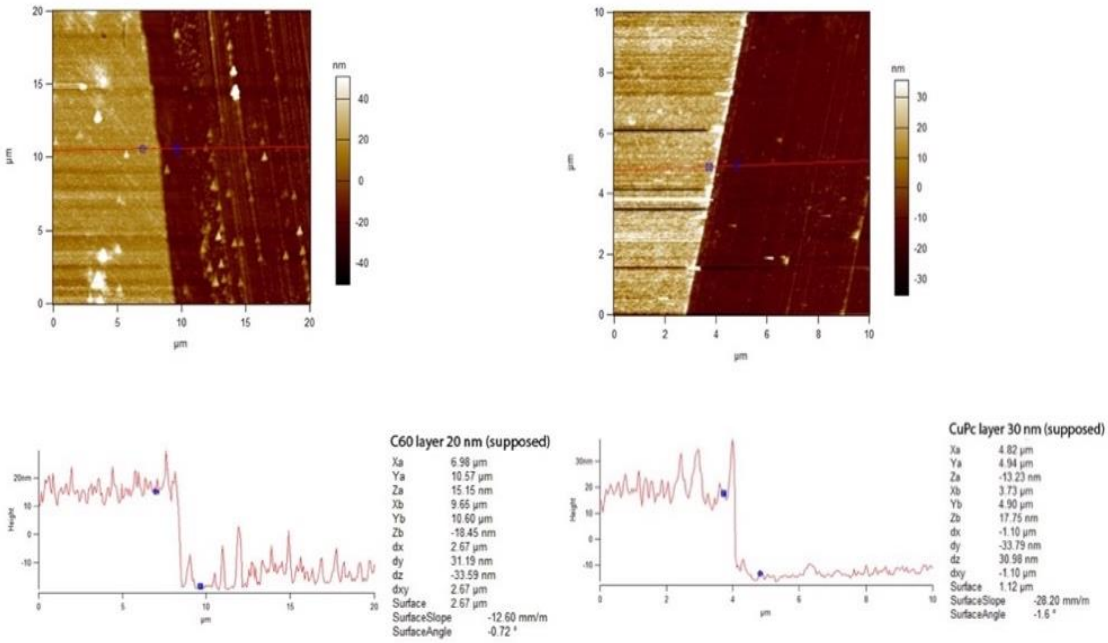


*Figure III.8 Two of the AFM thickness measurements respectively for $C_{60}$ (left) and CuPc (right).*

## III.2.3 Atomic Layer Deposition

The last technique used during the fabrication of the LHCs was the atomic layer deposition (ALD). It is part of the chemical vapor deposition family, since in this case a chemical reaction takes place during the process itself. It is a rather advanced method, which offers atomic-level controllability together with a very good homogeneity of the grown films. Every cycle approximately deposits a 0.1 nm thick layer, thus the atomic-level control. The working principle is more complicated than the previous ones reported since it involves more than one step. Moreover, even though it presents these above cited advantages, it possesses certain disadvantages as well. First and foremost, finding suitable reactants for the production of the desired material is not always easy, or worse, possible. Secondly, the nature of the substrate is crucial since it might spoil or completely hinder the ALD process [11]. That is the reason why a functionalization is usually performed before starting with the deposition itself.

Going a bit more into the details of the procedure, in can be divided into 4 main steps per cycle which are summarized in figure III.9. After inserting the substrate and closing the chamber, the first precursor can be pulsed in and adsorbed on the surface. It is a self-limited process meaning that only one layer at a time will adhere on the sample. The excess gas is then purged with an inert one like $N_2$ or Ar. Once this is done, the second precursor is inserted in the chamber and, reacting with the adsorbed one, will form the desired material. An inert gas is used one more time to remove all the extra reactants and then the cycle must be repeated until the final thickness is reached [12].

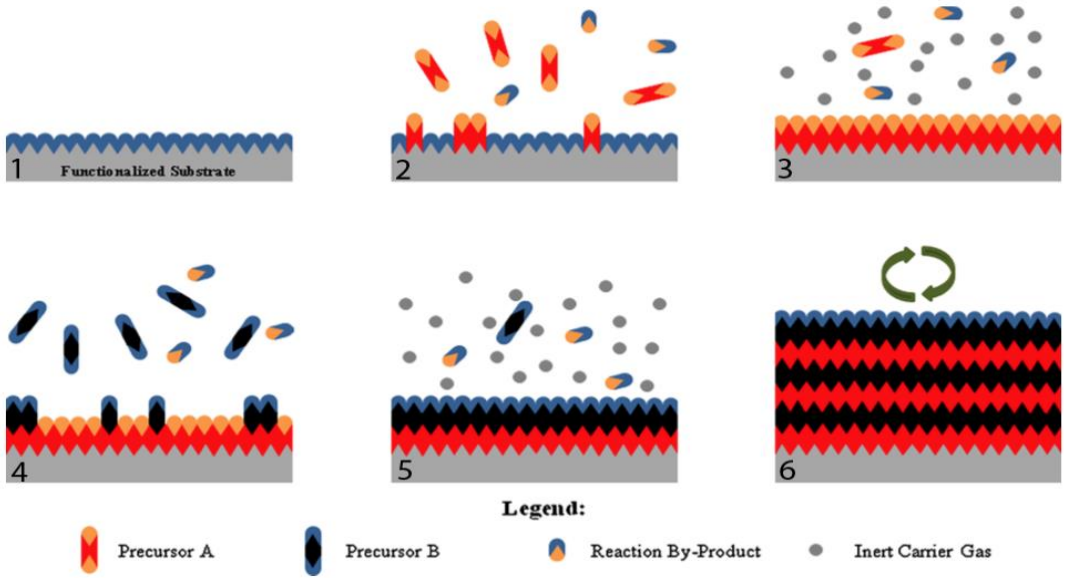


*Figure III.9 Schematic view of the ALD different steps [12].*

Specifically to this master thesis work, the target material to deposit was titanium dioxide and a Beneq TFS 200 was employed. Several precursors with different pros and cons can be used, but in this case $H_2O$ and $TiCl_4$ were chosen. $TiCl_4$ is one of the most used since it possesses a very high reactivity and thermal stability, even though it might lead to the presence of chlorine impurities. The temperature required for the process is 120 °C. Since the precursor associated to $TiCl_4$ is water, the functionalization performed on the substrates was a simple oxygen-plasma treatment to enhance the wettability [11,13].

## III.2.4 Device fabrication

Now that all the production techniques have been introduced, the overall process for the device fabrication can be explained as well. The first step is the substrate cleaning. Every glass substrate had an ITO pattern already present on it and from each sample, two final devices could be fabricated. The cleaning procedure consisted in a sonication for 10 minutes in acetone, then in isopropyl alcohol and finally in distilled water. Every substrate was then treated with an oxygen plasma cleaner to remove all the possible organic residuals and moreover to enhance the wettability. After these general steps, three different paths were followed depending on the insulant material to use: spin-coating for PMMA, thermal evaporation for $ZrO_2$ and ALD for $TiO_2$. When the first layer was fabricated, the evaporation of the two active materials was performed: $C_{60}$ first and CuPc second. The final dielectric layer was then fabricated with the same technique used in the bottom one. It must be specified that although the dielectric thicknesses were varied to study the effect of it, the active layer ones were kept fixed to 20 nm. The final

gold electrode was then thermally evaporated on top of everything using a specific shadow-mask. Each substrate contained two working devices with a final area of 4 $mm^2$. Before testing, the samples needed to be assembled upside down in order to let the light hits it from the glass side. To do so, the ITO contact was first exposed and then a small copper wire was soldered with silver paste both to it and to the gold one. After that, the sample was turned and attached to another glass substrate using the copper wires as new contacts.

## III.3 Characterization techniques

In this last paragraph, all the different instruments and techniques used for the characterization of the samples will be presented. Firstly, the ones directly related to the device testing. These include a lock-in amplifier and the set-up for the current measurement, which consists in a lamp, an amplifier and an oscilloscope.
After that, all the techniques used for the materials characterization will be illustrated starting from the apparatuses to measure the material absorption spectra, followed by the working principle of the AFM and finally, the two spectroscopies, transient and steady-state photo-induced absorption.

### III.3.1 Time-resolved current measurement

The most important characterization technique is the one used to measure the current flowing from the device shined with light, and hence the efficiency. To do this, the device was placed in a probe station and the two probes were connected to the copper wires previously soldered to the two contacts. The probes were then connected to the oscilloscope through a current preamplifier. As previously explained in the first chapter, the light harvesting capacitor is a device that works with cycles of light and dark. For this reason, a mechanical chopper with controllable frequency was installed between the light source and the sample. As a consequence of this, the current will flow first in one direction and then in the opposite one. In order to achieve a good quality measurement, the passage between light and dark must be as sharp as possible. This means that the light beam going through the chopper needs to be much smaller than the chopper aperture. To achieve that, a lens and mirrors system was used to focus the beam right before the chopper and then enlarge it again to cover the whole device surface.

### *III.3.1.1 Light Sources*

The light source used for the device characterization was a xenon lamp generating white light. Its own spectrum is reported in figure III.10 together with the solar one (measured in the past) in order to compare the two. The data were obtained with a lock-in amplifier and a calibrated photodiode. It can be observed that the two are rather similar, specifically considering which is the part of the spectrum absorbed by the active layer. A green LED emitting at 532 nm was also used to calculate the internal quantum efficiency for a reference device. The light intensity was checked before every measurement with a power-meter, but only after the lamp warmed up for 30 minutes.

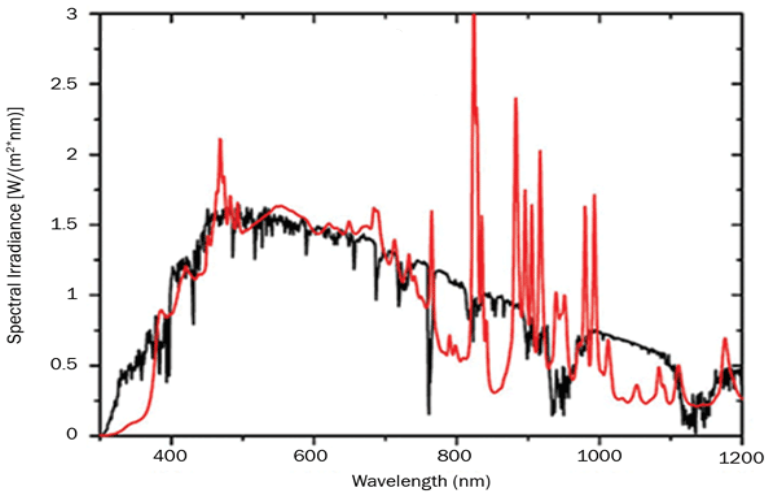


*Figure III.10. Xenon lamp spectrum (red) compared with the solar spectrum (black).*

### *III.3.1.2 Low-noise current preamplifier*

Since the current produced by the LHC was rather small, ranging from nA to μA depending on the different types, an amplifier was required. Another reason to place this instrument between the probe station and the oscilloscope, was that the final reading needed to be done on a voltage value. In this master thesis , a model SR570 low-noise current preamplifier from Stanford Research Systems was used.

### *III.3.1.3 Oscilloscope*

The oscilloscope is an instrument that allows the observation of a signal voltage varying over time. The waveform can then be studied for such properties as amplitude, frequency or shape. Even tough in the past they were analogic, nowadays the most used are digital, as the one exploited to measure the LHCs current. Specifically, a LeCroy WaveSurfer 104MXs-B was the one employed for this analysis. An example of a measurement obtained with it, it is shown in figure III.11.

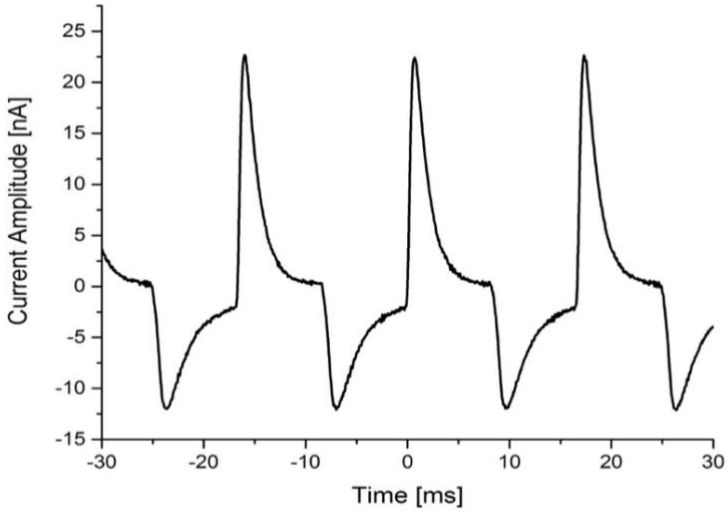


*Figure III.11. Example of an LHC current measurement obtained through the oscilloscope.*

## III.3.2 Lock-in amplifier

Lock-in amplifiers are used to detect and measure very small AC signals even when obscured by a noise source thousands of times larger. This kind of instruments use a technique known as phase-sensitive detection to single out the component at the specific frequency desired.

Lock-in measurements always require a frequency reference which, together with the signal, goes into the phase-sensitive detector/multiplier (PSD). Its output is simply the product of the two waves:

$$\begin{aligned} V_{PSD} &= V_{sig}V_L \, sin\big(\omega_{sig}t + \theta_{sig}\big) \, sin(\omega_L t + \theta_L) \\ &= {}^1\!/_2 \, V_{sig}V_L \, cos\big(\big[\omega_{sig} - \omega_L\big]t + \theta_{sig} - \theta_L\big) \\ &- {}^1\!/_2 \, V_{sig}V_L \, cos\big(\big[\omega_{sig} + \omega_L\big]t + \theta_{sig} + \theta_L\big) \end{aligned}$$

*Eq. III-2*

where *L* stands for the lock-in reference and *sig* stands for the signal to measure. It is possible to observe as the result is basically two AC signals, one with frequency $(\omega_{sig} - \omega_L)$ and one with frequency $(\omega_{sig} + \omega_L)$. If a low pass filter is added, all the AC signals are cut out. If $\omega_{sig}$ equals $\omega_L$ the difference frequency component turns into a DC signal which is not filtered. The output of the PSD plus the filter is then:

$$V_{PSD} = {}^1\!/_2 \, V_{sig}V_L \; cos\big(\theta_{sig} - \theta_L\big) \sim V_{sig} \cos(\theta)$$

*Eq. III-3*

To maintain this as a DC signal though, the difference between the two phases $\theta$, must be constant. In other words, the reference needs to be phase-locked to the signal, hence the name of the instrument "lock-in amplifier". This phase dependency can be eliminated adding a second PSD that shifts the output of the first by 90° giving as a result:

$$V_{PSD2} = {}^{1}/_{2}\, V_{sig} V_L \; sin(\theta_{sig} - \theta_L) \sim V_{sig} \sin(\theta)$$

*Eq. III-4*

Now two different outputs exist, one proportional to $\cos(\theta)$, renamed X, and one proportional to $\sin(\theta)$, renamed Y. At this point it is obvious which is the next step to do in order to obtain the signal amplitude:

$$V_{sig} = (X^2 + Y^2)^{1/2}$$

*Eq. III-5*

The lock-in amplifier, because it multiplies the signal with a pure sine wave, measures the single Fourier (sine) component of the signal at the reference frequency. Meaning that if the signal is not a pure sine, only the first harmonic will be measured. For example, a simple square wave with frequency $\omega$ can be considered as input signal. This is actually composed of many sine waves (Fourier series) at multiples of $\omega$ with carefully related amplitudes and phases. A 2V peak-to-peak square wave can then be expressed as:

$$V_{sig} = 1.273 \sin(\omega t) + 0.4244 \sin(3\omega t) + 0.2546 \sin(5\omega t) + \cdots$$

*Eq. III-6*

and the instrument will only measure the first component of the Fourier series [14]. A Stanford Research Systems MODEL SR830 was used.

## III.3.3 Absorption Spectrum

When working with solar energy harvesting devices, it is always useful to know the absorption spectra of the materials involved in the process. In this way, it is possible to understand whether the efficiency is limited by the low absorption or by other factors. The spectrum itself can be obtained with several different methods and in this case an ellipsometer was chosen. This particular instrument is usually employed for other purposes, as the investigation of dielectric properties or material composition. It exploits the change of the light polarization upon reflection or transmission and compares it to a model. Since it can simply measure the pure transmission and reflection, it can also be used to obtain the absorption spectrum of a sample.

When radiation strikes a surface, three different phenomena can happen: transmission, absorption and reflection. If these three are expressed as a percentage of the total incident energy, the sum must be always 100 as follow:

$$a + r + t = 100$$

*Eq. III-7*

where $a$ is the absorptivity, $r$ is the reflectivity and $t$ is the transmissivity. More in details, a body is considered transparent when it can transmit some of the radiation waves hitting the surface. It is called instead opaque, when none of the electromagnetic radiation passes through the material itself. In this case the light incident on the surface can only be reflected back or absorbed by the sample and thus the previous equation becomes:

$$a + r = 100$$

*Eq. III-8*

It must be specified that reflectivity differs from the other properties, since it depends on the incident angle. In practice, surfaces are assumed to reflect in two possible ways: diffused and specular. In the first case the radiation is reflected equally in all the directions, while in the second one the incident and the reflection angle are the same [15]. Particularly in the case of this project, the reflection measurement was done at a 90° incident angle assuming then a specular reflection. The instrument employed was a VASE Ellipsometer from J.A. Woollam and a schematic view of the working principle of the measurement is reported in figure III.12.

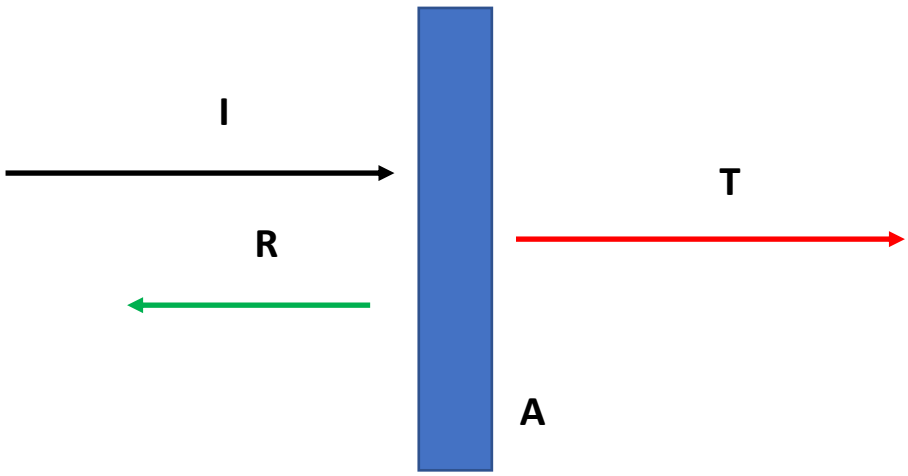


*Figure III.12. Schematic view of the working principle of the absorption spectrum measurement based on equations III.7-8.*

## III.3.4 Atomic Force Microscope

The atomic force microscope (AFM) is part of the scanning probe microscopes family. It possesses an extremely high resolution in the order of nanometer fraction and it is used to analyze the sample topography. It can also be used in other set-ups like the force spectroscopy one, where it measures the force between the sample and the probe (e.g. the stiffness).

The working principle is rather simple and it is summarized in figure III.13. A cantilever carrying a sharp tip is fixed to the support which usually contains a piezoelectric element oscillating the beam itself. A laser is then pointed at the far end of it, where the tip is placed as well, and it is reflected to a detector. The cantilever is then moving across the surface following the topography and, going up and down as consequence of it, an image is created detecting these changes. This contact mode presents a main problem when working in ambient condition: the tip may stick to the sample. To prevent this from happening, the AC/tapping mode was developed. In this kind of AFM measurement, the one that requires the piezoelectric element, there is far less contacts between the instrument and the surface. The cantilever is oscillating near its resonance frequency and its amplitude is kept constant. When the tip comes closer to the surface though, the small interactions forces, as Wan der Waals or dipole-dipole forces, interfere with the oscillation. These interferences are detected and a final image is created [16].

The AFM, a Cypher ES SPM (Asylum Research), was mainly used to measure the sample thickness during the calibration of the thermal evaporation. In order to do so, the evaporated thin film was scratched with a needle, the scan was run near this mark to measure the height difference and hence obtaining the film thickness.

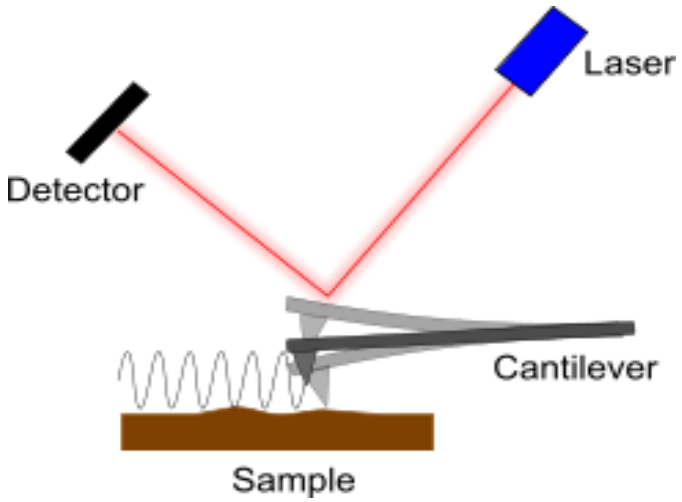


*Figure III.13. Atomic force microscope schematic view of the working principle [16].*

## III.3.5 Ultrafast transient absorption spectroscopy

In this paragraph, a widely used technique of time-resolved spectroscopy based on absorption measurement will be introduced: ultrafast transient absorption spectroscopy. It is part of the so-called pump-probe (PP) spectroscopy family. The idea of a pump-probe measurement is quite easy: a sample (i.e. inorganic semiconductors, organic compounds and biological systems) is excited using a short laser pulse, the pump. Another pulse, which arrives sometimes after the first one, is used to probe how the absorption of the sample was altered by the pulsed laser. Varying the arrival time of the probe within respect to the pump, it is possible to measure the whole time-dependence of the absorption change [17,18].

In the case of ultrafast measurements, an ultra-short (~100 fs) pump pulse is used to excite the material. As a probe, an ultra-short, low intensity white light pulse is exploited instead. Obviously, the pump should be more intense than the probe, since its purpose is to excite the sample while the probe merely interrogates it. Ideally the second pulse should have no influence at all. It is clear that this technique is a very powerful investigation tool, but as a consequence of that, it is also very complicated to interpret [18]. Typically, photo-excited carriers can go through different relaxation pathways before returning to their initial thermal equilibrium state. In inorganic semiconductors, the timescale for transient processes as carrier-carrier scattering is usually in the order of few to hundred femtoseconds. Slower optical processes instead, as carrier diffusion, occurs in the picoseconds range. However, in the case of organic semiconductors, due to the typical strong electron-phonon coupling, photon absorption leads to the formation of polarons. The existence of these polarons generates new sub-gap electronic states that give rise to new features in the transient absorption measurement. Charged photo-excitation can be investigated by pump-probe techniques. The principle of the photo-induced measurement can be illustrated by a simplified two excited levels system, as shown in figure III.14. Level 2 is the electronic state generated after the excitation that leads to the transition from the ground state (1 -> 3). Monitoring the evolution of such system, one can observe the emergence of a new absorption feature (2 -> 3). Both these states have their own characteristic times [17].

What is actually measured during the experiment is the transmission spectrum of the probe when the pump is on and when the pump is off. The normalized transmittance variation is done as:

$$\frac{\Delta T}{T} = -\frac{T^{on} - T^{off}}{T^{off}} = \Delta\alpha$$

*Eq. III-9*

where $T^{on}$ is the transmittance of the probe light when the pump pulse is on and $T^{off}$ is the transmittance of the probe light when the pump is off. In figure III.14 it is possible to observe both a negative and a positive transient absorption signal. When the pump excites the sample, some molecules leave the ground state and transfer to the excited one (1 -> 3). As a consequence, the concentration of molecules in the ground state decreases and part of the absorption signal from this state disappears. Therefore, at the wavelength where this absorption occurs, the signal $\Delta\alpha$ becomes negative. The spectral shape of this negative signal is identical to the linear absorption measured with a spectrophotometer. This contribution is called *ground state bleaching* (GSB) [18].

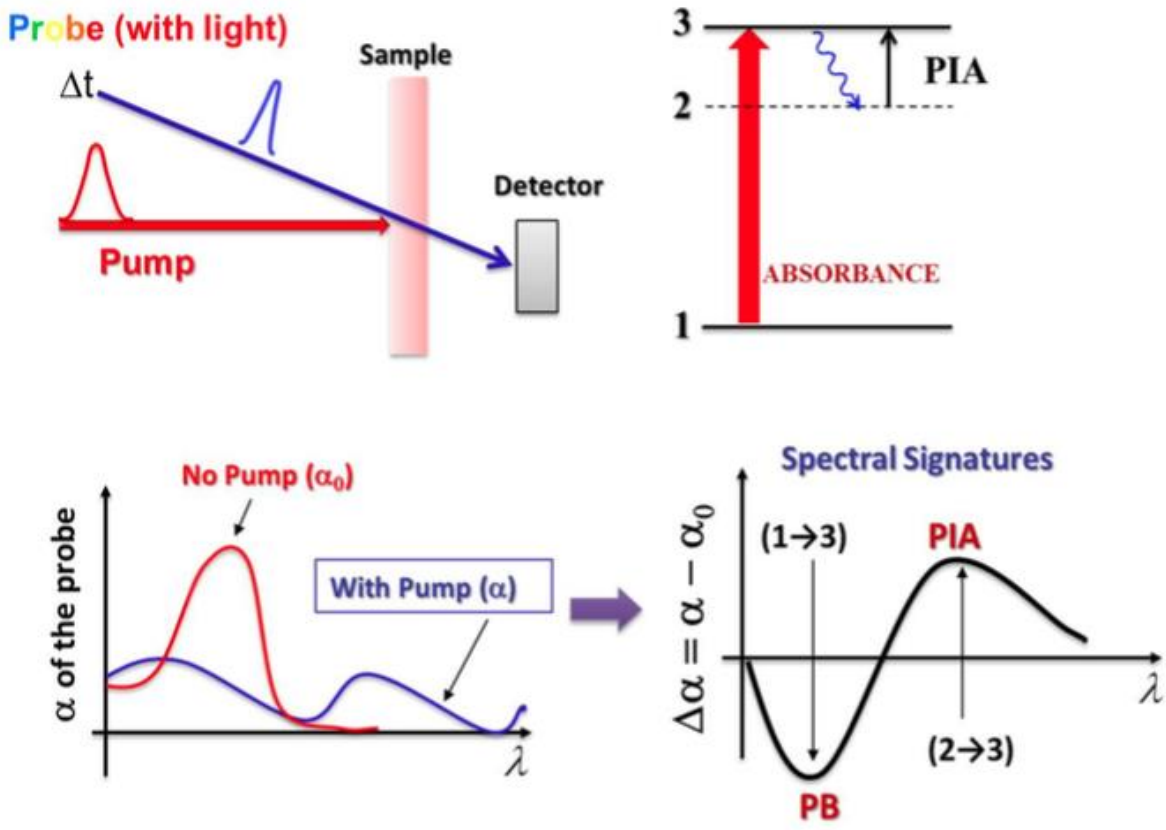


*Figure III.14. Schematic view of the pump-probe set-up and its working principle [17].*

The positive contribution to the PP signal is instead called *induced absorption* (IA) and it derives from the fact that a molecule in the excited state, can further absorb photons and jump to an even higher state or relax to level 2 and then absorb back to level 3. This process can only occur with an excited molecule, therefore, after the excitation, an additional positive absorption feature appears. It must be specified, that IA can be caused not only by a singlet excited state, but it can also occur, after an intersystem crossing, from a triplet excited state. Furthermore, even when the molecule is back to the ground state, but a slightly different environment from the initial one, a different induced absorption can also be

observed. All these possible contributions are able to provide a lot of information about the sample which is being analyzed, but they also make the interpretation of the results much more difficult as already mentioned [18].

In relation to this master thesis work, a home-built femtosecond pump-probe transient absorption spectrometer was used for the characterization. Since the excited state species are typically short-lived, short (~100 fs) duration pump and probe pulses were needed to get the temporal evolution of excited states. The schematic view of the spectrometer used is shown in figure III.15. The set-up was comprised of four main parts which are a white light generator, an optical parametric amplifier (OPA), a delay-stage and a processing software. The OPA is a frequency converter where the parametric amplification consists in a three-waves mixing process in nonlinear crystals. White light was generated first and then, the required wavelength was selected and amplified in the second stage. The optical delay between pump and probe was achieved and controlled by a delay-stage that was used to monitor the temporal dynamics of the system. The overall set-up was controlled by a LabVIEW program where the normalized transient transmission was measured in a time-resolved domain. An OPA (Palitra, Quantronix) was employed as an excitation source. The Palitra was seeded by a 1 kHz Ti:sapphire regenerative amplifier (800 nm fundamental wavelength; 1 W average power; ~100 fs pulse width). The pump beam was chopped at 83 Hz and referenced to a lock-in amplifier. For the measurement directly related to this thesis, a pump with a 400-nm wavelength and a photon density of $7.82*10^{18}$ photons/cm3 was selected [17].

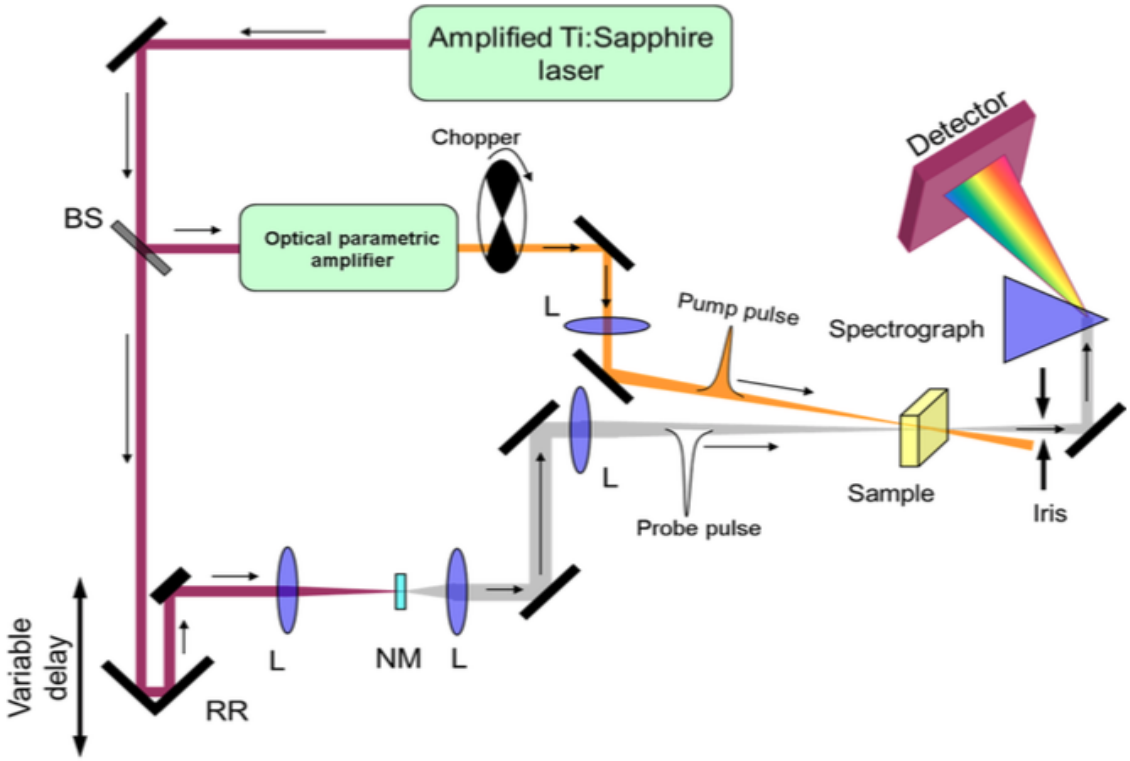


*Figure III.15. Schematic view of the home-built femtosecond pump-probe transient absorption spectrometer [18].*

## III.3.6 Steady-state photo-induced absorption spectroscopy

The last technique presented in this chapter is the steady-state photo-induced absorption spectroscopy. It measures the transmittance (and as a consequence the absorption) difference of the samples between two equilibrium states: namely, between the pump light illumination state and the dark one. Although the working principle itself is rather similar to the time resolved measurement, this one focuses on the long-lived charges, which have strong correlation to devices applications. Once again, a pump laser is required to populate the excited states, while a probe is used to interrogate the sample. In this case however, they are used in a continuous wave set-up. After collecting the transmission spectrum with both pump on and off, the normalized transmittance difference is calculated again as:

$$\frac{\Delta T}{T} = -\frac{T^{on} - T^{off}}{T^{off}} = \Delta\alpha$$

*Eq. III-10*

where, as in the case of the transient measurement, $T^{on}$ is the transmittance of the probe light when the pump pulse is on and $T^{off}$ is the transmittance of the probe light when the pump is off. The spectrum obtained is of the same kind as for the other PP measurements. More in details, a negative signal means a ground state population reduction and so a GSB. On the other hand, a positive one is related to the new additional absorptions that appear upon excitation, the IA [19,20].

Figure III.16 shows the experimental set-up for the steady-state photo-induced absorption spectroscopy. A Nd-YAG continuous wave laser (green, λ=532 nm) was used as a pump and a vacuum FT-IR spectrometer (Bruker Vertex 80v) as a probe. The laser beam was deflected by an acousto-optic modulator (ME-402) that is triggered by the FT-IR itself for each state (“on” and “off”). The laser beam was then expanded by a beam expander to ensure that the spot size was larger than the IR probe dimension.

To obtain a higher signal to noise ratio, samples are usually measured under low temperature condition (78K) in a liquid nitrogen cooled cryostat kept in a vacuum level around $10^{-3}$ Pa. Depending on the desired spectral region, different detectors and beam splitters in the FT-IR can be used to have spectra from the visible to the mid-IR region. In the case of this work however, the experiments were run at room temperature and only one kind of set-up was used. Specifically, the one which allows to obtain spectra in the Vis-NIR range (415 nm to 1250 nm) was selected. In this particular configuration, the detector was a RT-Si, the light source was a tungsten lamp and the beam splitter was a $CaF_2$-UV enhanced. A proper long pass filter was used to cut out the pump. Measurements were done with a Bruker reflection/transmission accessory (A510/Q-T), where the probe beam has an 11° incidence angle while the pump one is normally incident to the sample. The transmitted light intensities were recorded with and without photoexcitation

by the FT-IR under rapid scan mode. In order to reduce the heating effects induced by the laser, each cycle of measurement contains 5 to 10 scans for each “on” and “off” state and it is repeated 600 times. Therefore, a total 6000 scans were taken and averaged in order to achieve the desired signal to noise ratio [19].

With this last pump-probe technique described, all the materials and instruments used either in the fabrication or the characterization have been reported. All the working principles have been explained and analyzed as well. In the next chapter the results obtained will be presented and discussed.

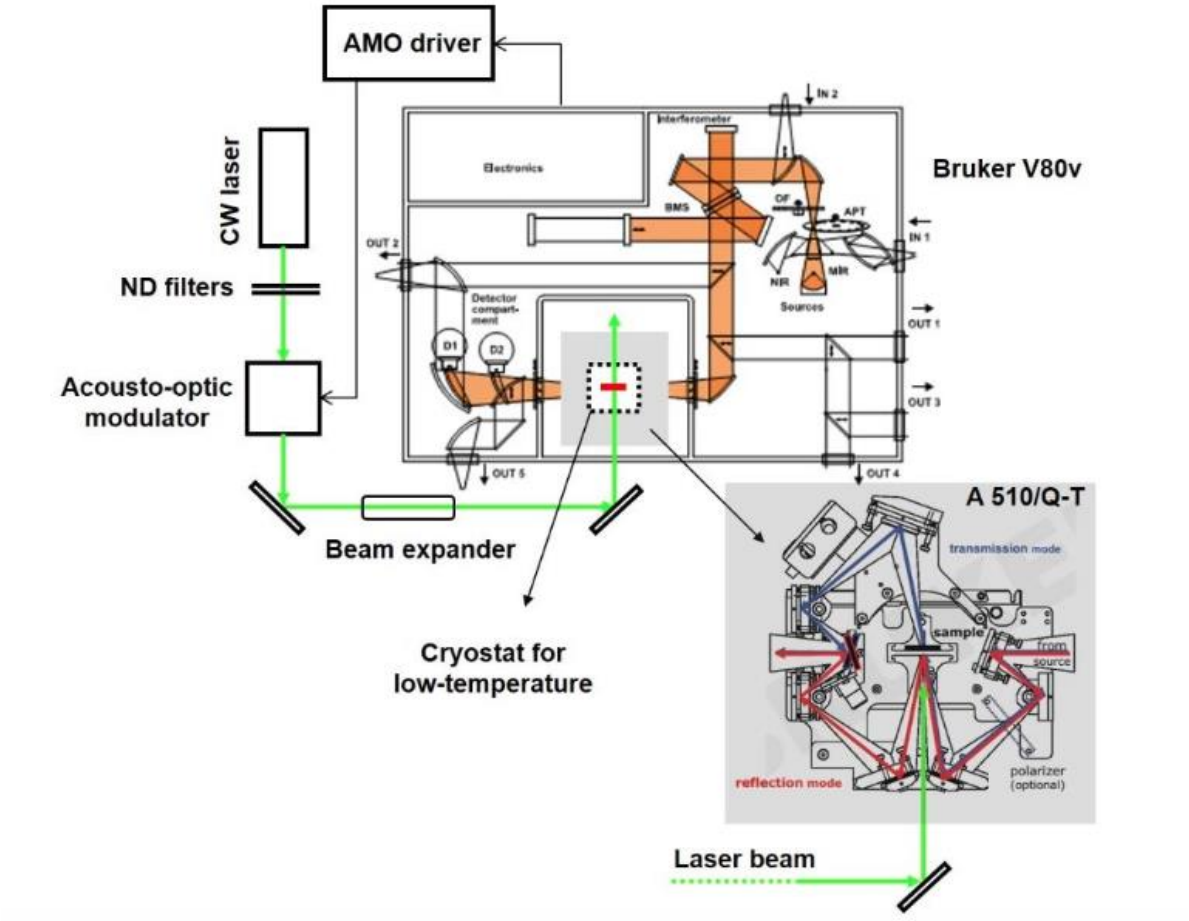


*Figure III.16. Experimental set-up for the steady-state photo-induced absorption spectroscopy. The light grey area indicates the position of reflection/transmission accessory in the FT-IR [19].*

# Bibliographic References

[1] T. Enoki, S. Miyajima, M. Sano, and H. Inokuchi, “Fullerenes,” J. Mater. Res, 1990.

[2] J. Kroeze, I. Erwin, and J. G. Peterman, “Small molecule thin films for photodynamic anti-bacterial therapy,” vol. 1, pp. 1–15, 2016.

[3] Q. L. and L. W. ZHOU Weiya, XIE Sishen, QIAN Shengfa, ZHOU Tang, ZHAO Ri’an, WANG Gang, “Absorption spectra of C60 and C70 thin films.” 1996.

[4] M. Garbugli *et al.*, “Light energy harvesting with nano-dipoles,” *Nanoscale*, vol. 4, no. 5, p. 1728, 2012.

[5] H. Vázquez, W. Gao, F. Flores, and A. Kahn, “Energy level alignment at organic heterojunctions: Role of the charge neutrality level,” *Phys. Rev. B - Condens. Matter Mater. Phys.*, vol. 71, no. 4, pp. 1–4, 2005.

[6] U. Ali, K. J. B. A. Karim, and N. A. Buang, “A Review of the Properties and Applications of Poly (Methyl Methacrylate) (PMMA),” *Polym. Rev.*, vol. 55, no. 4, pp. 678–705, 2015.

[7] H. L. Lu and D. W. Zhang, “Issues in High-k Gate Dielectrics and its Stack Interfaces,” *High-k Gate Dielectr. C. Technol.*, pp. 31–59, 2012.

[8] O. S. Abd El-Ghany and A. H. Sherief, “Zirconia based ceramics, some clinical and biological aspects: Review,” *Futur. Dent. J.*, vol. 2, no. 2, pp. 55–64, 2016.

[9] X. Chen and S. S. Mao, “Titanium dioxide nanomaterials: Synthesis, properties, modifications and applications,” *Chem. Rev.*, vol. 107, no. 7, pp. 2891–2959, 2007.

[10] M. Ohring, “Thin-film evaporation processes,” in *Materials Science of Thin Films (Second Edition)*, 2002, pp. 95–144.

[11] S. W. Lee *et al.*, “Influences of metal, non-metal precursors, and substrates on atomic layer deposition processes for the growth of selected functional electronic materials,” *Coord. Chem. Rev.*, vol. 257, no. 23–24, pp. 3154–3176, 2013.

[12] R. W. Johnson, A. Hultqvist, and S. F. Bent, “A brief review of atomic layer deposition: From fundamentals to applications,” *Mater. Today*, vol. 17, no. 5, pp. 236–246, 2014.

[13] A. Kaariainen, Tommi; Cameron, David; Kaariainen, Marja-Leena; Sherman, “Fundamentals of Atomic Layer Deposition,” *At. Layer Depos. Princ. Charact. Nanotechnol. Appl.*, pp. 1–31, 2013.

[14] Stanford Research Systems, “Model Sr830,” *Instrument Manual*, 2011.

[15] J. Peatross and M. Ware, “Physics of Light and Optics: A Free Online Textbook,” *Front. Opt.*, p. JWA64, 2010.

[16] N. Jalili and K. Laxminarayana, “A review of atomic force microscopy imaging systems: Application to molecular metrology and biological sciences,” *Mechatronics*, vol. 14, no. 8, pp.

907–945, 2004.

[17] M. P. Fard, “Ultrafast Charge Transfer at GaAs/P3HT as a Model System for Hybrid Organic-Inorganic Heterointerfaces,” 2015.

[18] M. Vengris, “Introduction to time-resolved spectroscopy.”

[19] W. Zilong, “PLASMON-POLARON COUPLING IN CONJUGATED POLYMERS ON,” 2015.

[20] X. Y. Chin, “CHARGE MODULATION SPECTROCOPY OF SOLUTION PROCESSABLE FIELD-EFFECT TRANSISTORS,” 2016.

# Chapter IV. Results and discussions

In this fourth chapter, all the results obtained during this master thesis project will finally be presented and discussed. The chapter is divided into two parts, one for the active layer study and one for the device characterization. The first part, which is also the shortest, will present the results obtained through the ultrafast and the steady-state spectroscopy. Specifically, these two kinds of spectroscopy will help to better understand the charge carriers behavior and thus the working principle of the device. Once this is done, the device fabrication can start and the LHCs can then be tested with the time-resolved current measurement. A reference device, the one presented in the Garbugli et al. paper [1], will be tested first. After that, all the different insulant layer thickness and materials will be studied from a behavior point of view initially and an efficiency one after. It must be specified that a preventive investigation will be done on titanium dioxide to better understand its effectiveness as an insulant. More in details, a device will be fabricated with only the donor layer and an asymmetric structure $TiO_2/ZrO_2$. Finally, a paragraph focused on the light intensity effect on LHCs performance will be presented where both the time resolved current measurement set-up and the lock-in amplifier will be used.

## IV.1 Active layer study

This first paragraph will be dedicated to the study of the active layer and thus the charge carriers behavior within the donor/acceptor interphase will be studied and presented. Two different techniques will be used to focus on two different aspects of the process: ultrafast transient absorption spectroscopy (TA) and steady-state photo-induced absorption spectroscopy. The first one is used to study ultrafast processes and hence the charge transfer from the donor to the acceptor layer, which usually occurs within few picoseconds. On the other hand, the second experiment allows the study of long-lived dipoles. This will help to understand if the separated charges are stable enough to survive for long time before the recombination, a desired characteristic for light harvesting capacitors. This effect was simulated in chapter II, where the linear dependency between efficiency and recombination time was shown.

## IV.1.1 Ultrafast transient absorption spectroscopy

A large interface between electron-donor and acceptor materials is a key requirement for obtaining effective exciton splitting and charge generation in organic photovoltaic devices. Although the bulk heterojunction has been proven to be one of the most efficient architecture for exciton splitting, it is a rather complex nanocomposite system whose nanoscale arrangement is extremely sensitive to a number of process conditions (i.e. annealing temperature/time, deposition technique, solvent choice among others) [2]. For this reason, a less complex planar interphase between CuPc and $C_{60}$ is investigated, the same used for LHCs [3]. The aim of this study is to observe the possible occurrence of charge transfer processes at the fabricated interface, therefore proving the effectiveness of such geometry. For this purpose, an ultrafast transient absorption spectroscopy is performed on both the single electron donor layer and on the electron donor/acceptor bilayer.

The first step of the analysis is the interpretation of the single CuPc layer transient absorption spectrum. Understanding all the present features, with the help of other publication on the matter [4], is fundamental for a correct study of the bilayer system that will be performed afterwards. The transient spectra for both short and long times are reported in figure IV.1 and IV.2 together with the linear absorption spectrum that also helps with the final interpretation.

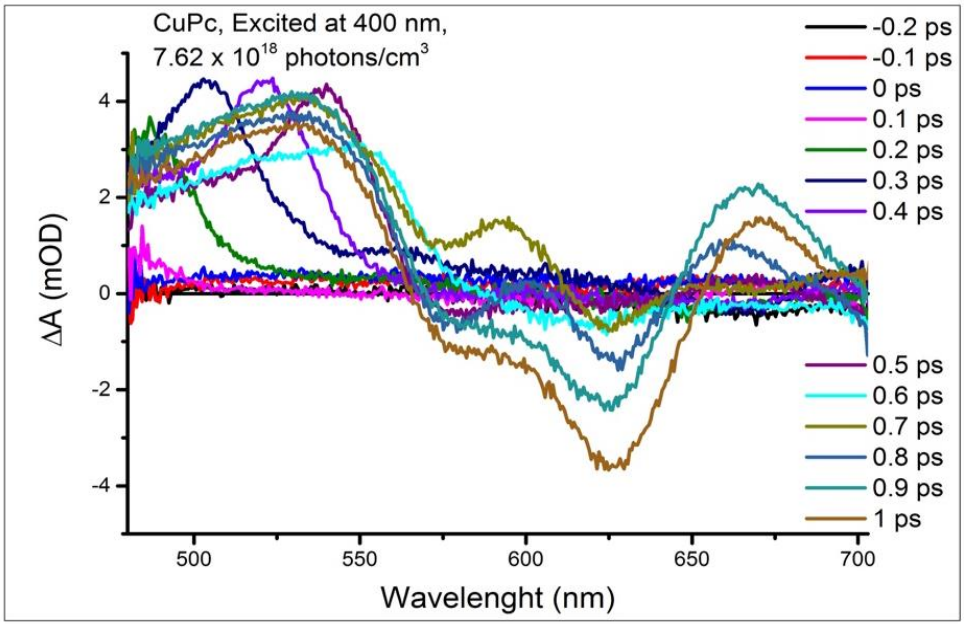


*Figure IV.1 Transient photo-induced absorption for CuPc for pump-probe time-delays ranging from -0.2 ps to 1 ps.*

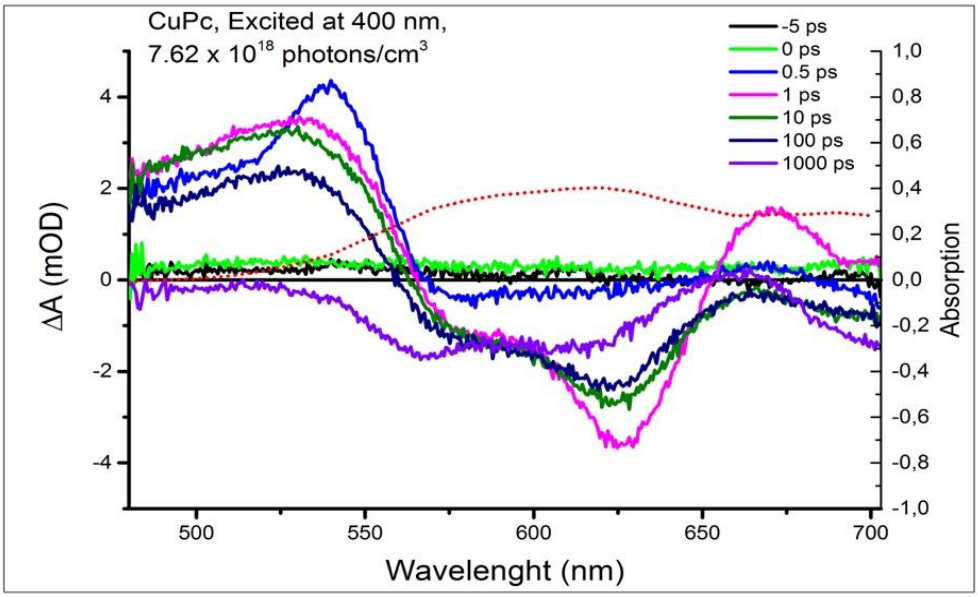


*Figure IV.2 Transient photo-induced absorption for CuPc for pump-probe time-delays ranging from -5 ps to 1 ns.The dotted line denotes the linear absorption. The two different scales do not allow a direct comparison.*

The transient spectra show two broad positive induced absorptions (IA) centered around 520 nm and 680 nm. They also show a negative signal peaked at 620 nm that can be associated to a ground state bleaching (GSB) and that is why the linear absorption spectrum is reported as well. Comparing the two signals shape, it is evident that they do not perfectly match and thus it can be surmised that the IA overlaps with the GSB. In any case, for longer pump-probe delay time the GSB spectral shape gets closer to the linear absorption one, an effect that can be attributed to the depopulation of the excited states [4].

Given that most of this master thesis project was devoted to the study of the charge transfer phenomenon occurring at the donor/acceptor interface, the focus will now switch to the spectroscopic characterization of the bilayer heterojunction structure. Looking at the TA spectra for CuPc/$C_{60}$ (figure IV.3), it is possible to observe a new and short-lived GSB feature (488nm) that decays in less than 0.5 ps and that is concomitant with the growth of a positive signal at around 560 nm. This behavior can be usually associated to a charge transfer process, since such IA was not present in the CuPc-only system. In a second place, the intensity of the overall positive signal is higher when the acceptor is added, while the negative one is lower. This means that there is a broad positive signal overlapping with the CuPc one. As a consequence, it can be safely assumed that there are more excited states present due to the charge transfer from donor to acceptor.

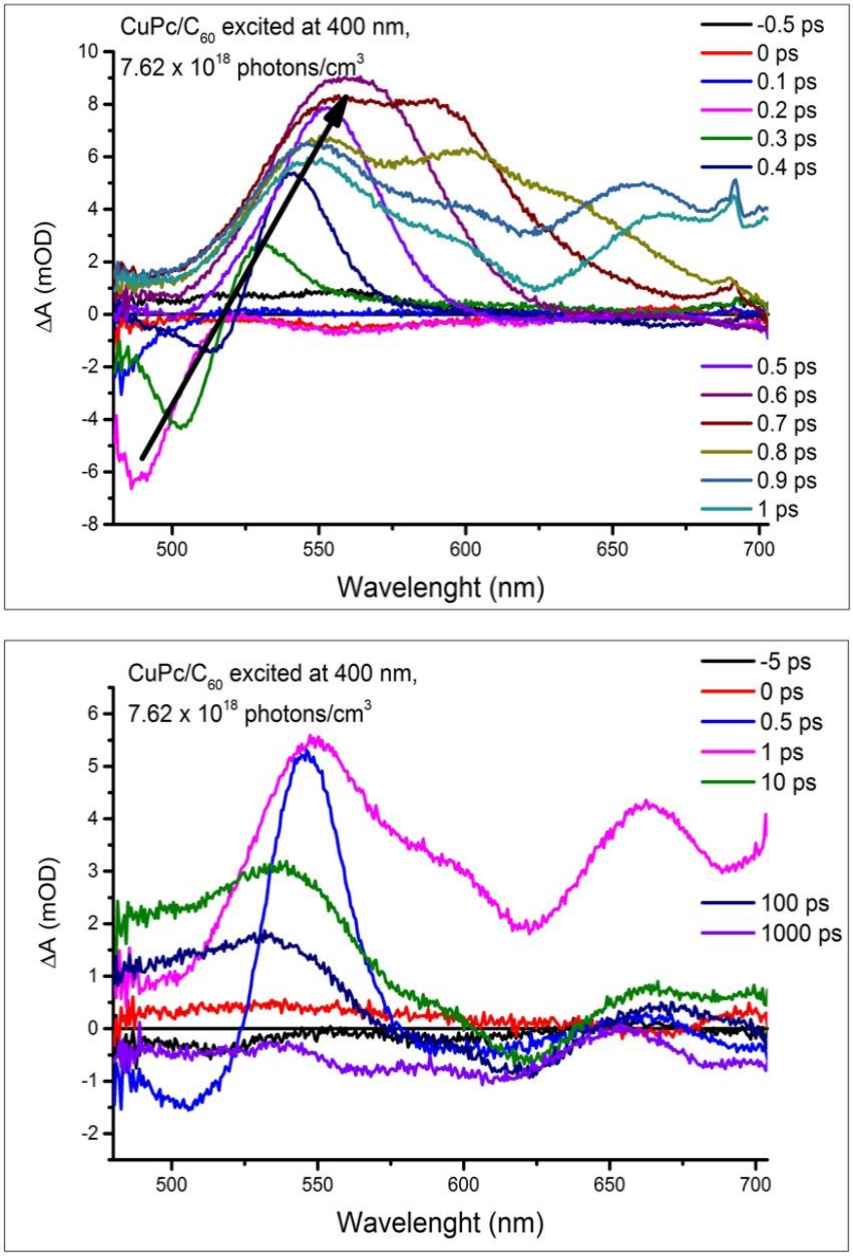


*Figure IV.3 Transient photo-induced absorption for the CuPc/$C_{60}$ interface at shorter (above) and longer (below) times. The arrow represents the possible charge transfer.*

Such a transfer can be visualized better in the TA dynamic plots (figure IV.4), in which the time evolution of the transient signal over the pump-probe delays (up to 1 ns) is reported. It is possible to estimate a characteristic time of 0.3 ps for this process, as the decay of the GSB at 488 nm and the rise of the IA at 560 nm occur within this time-frame.

Having observed the charge transfer process, in the next paragraph the nature of such charged species (i.e. long-lived dipoles) is investigated by means of steady-state photo-induced absorption spectroscopy [5].

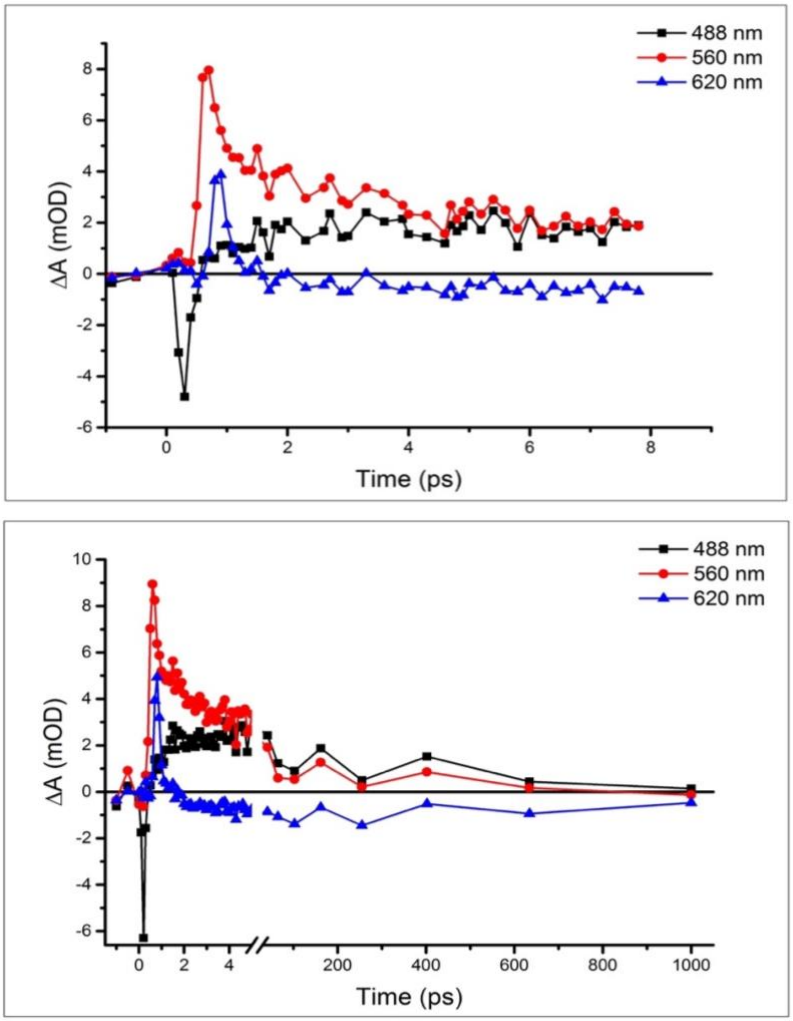


*Figure IV.4 Transient signal for three specific wavelengths reported to observe the different states life. The first graph shows the range from 0 to 8 ps while the second covers the 1-1000 ps range.*

## IV.1.2 Steady-state photo-induced absorption spectroscopy

In the last paragraph of chapter II, the effect of changing the active layer parameters was simulated. Specifically, the linear dependency between the efficiency and the decay time of the separated charges was presented. The goal of this second spectroscopy technique is to study the presence of long-lived dipoles after photo-excitation. In a similar way to the transient analysis, both the CuPc single-layer and the donor/acceptor interface are studied, but herein the $C_{60}$ single-layer is additionally investigated. This is necessary in order to disentangle the contribution of free charges from bound charge states. Three different pump powers are employed to better separate true signal from pure artifacts since, as a general trend, increasing the power the intensity detected should increase. The three spectra are reported in figure IV.5

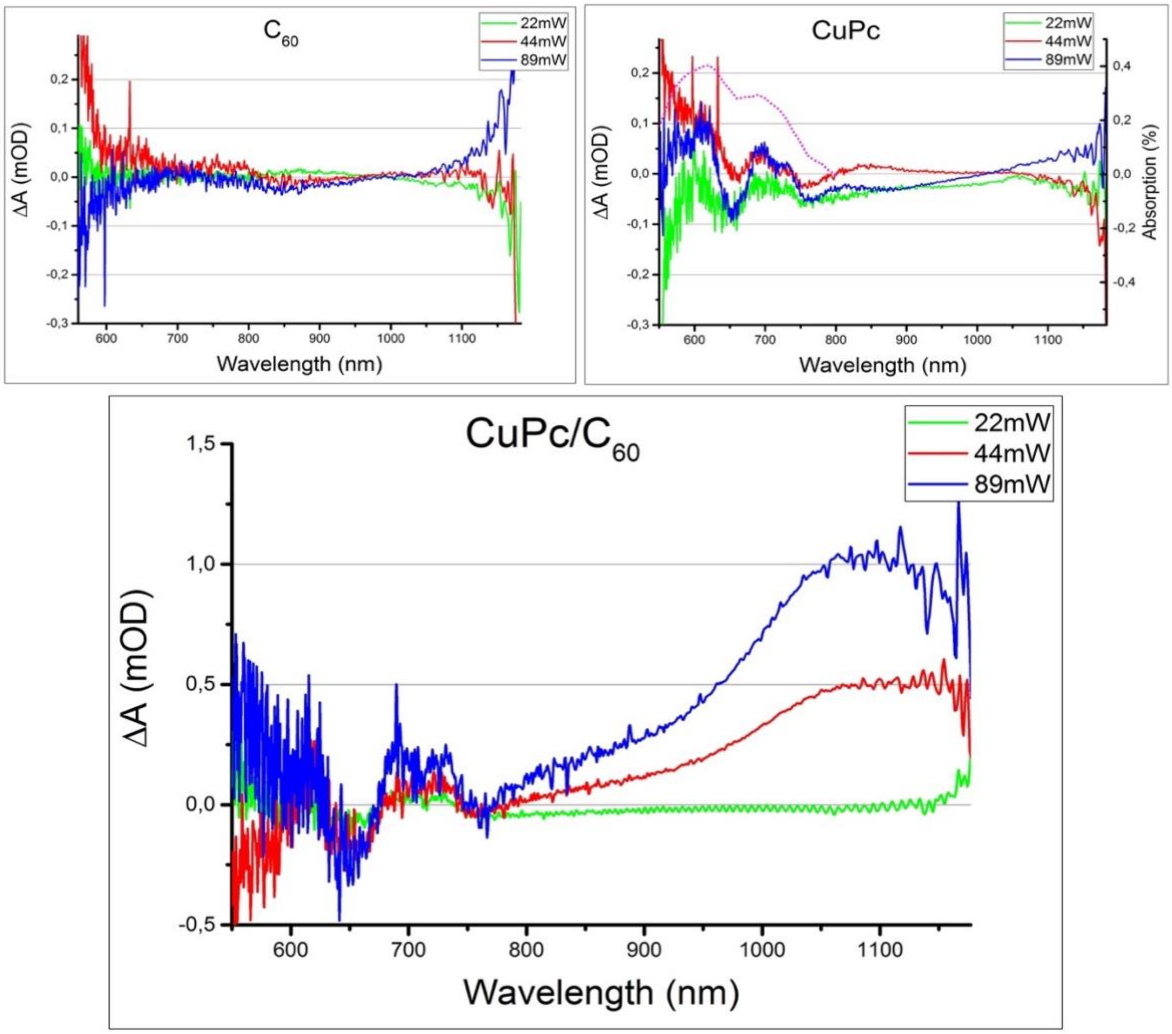


*Figure IV.5 Steady-state photo-induced absorption spectra for the three different systems. Three different power values of the pump laser are reported for each spectrum. $C_{60}$ is at the top left, CuPc is at the top right and the bi-layer is at the bottom. The dotted line denotes the linear absorption. The two different scales do not allow a direct comparison.*

Concerning the CuPc single-layer, it is possible to discern rather similar features to the ones witnessed in the ultrafast TA measurements. Specifically, a GSB in the 600-650 nm range can be observed, although the noise is moderately high due to the low sensitivity of the Si-detector in such spectral region. The second feature is a photo-induced absorption at 700 nm that was not present in the TA spectra, likely due to the profound difference in the probed time-window. When entering the infrared region, the signal seems to lose any specific trend at all the three powers. Regarding the $C_{60}$-layer instead, it is not possible to observe any discernible signal, since fullerene does not absorb much in the visible range.

As a consequence, it can be safely assumed that all the differences introduced with the interface system are due to the presence of the interface itself. Firstly, an increase in the signal intensity can be noticed. For instance, when passing from the CuPc single-layer to the CuPc/$C_{60}$ one, the photo-induced absorption

at 700 nm increases in intensity by almost three times. This intensification can be explained by the increase of the excited states related to the charge transfer process from donor to acceptor. The second difference present in the bi-layer spectrum is the appearance of an extremely intense feature in the near-IR at 1070 nm, that can be linked to the charge transfer process, as confirmed by the scientific literature [6]. Specifically, with a transient photo-induced absorption in the nanoseconds range, it is possible to observe the manifestation of an intermediate state for $C_{60}$ after the charge transfer. This feature peaks at 750 nm, but it is not observable with a steady-state technique since it transfers to another state which instead peaks at 1070 nm. This second signal is instead discernible even at longer times and it is the one measured in this case [6]. The broadness of such signal is another typical signature of separated charges states. Now that the active layer has been studied and long-lived charge transfer states have been observed, the fabrication and characterization of the actual devices can start.

## IV.2 Reference device

At this point, the first step in the LHCs study is the characterization of a reference device that will be then used as a comparison for all the other presented in the following sections. The reference structure is illustrated in figure IV.6 together with its time resolved photo-current measurement.
The current obtained, and thus the efficiency, is definitely lower if compared to the one reported in the Garbugli et al. paper. This is due to the fact that, even though the device structure is exactly the same, in the present work a white light is used for the characterization instead of a laser emitting in the absorption maximum wavelength [1].

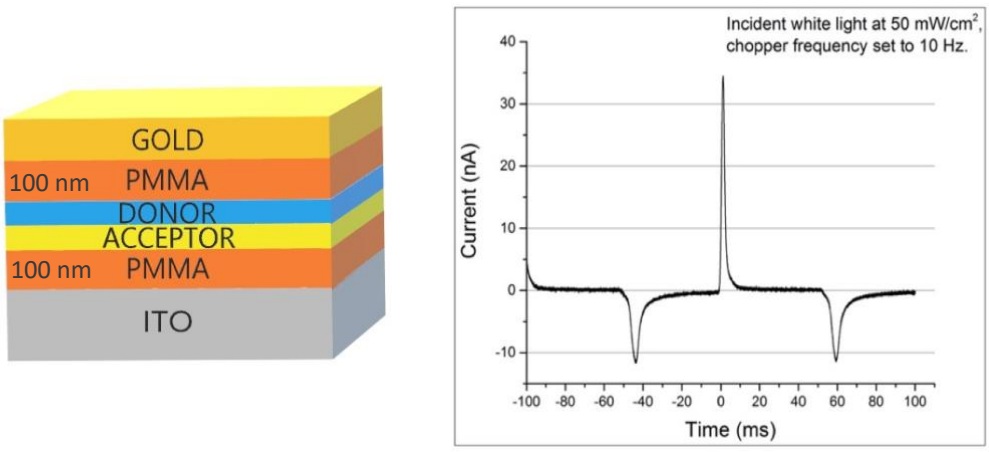


*Figure IV.6 Reference device structure and time resolved photo-current measurement performed under white light (I=50 mw/cm²) and with a chopper frequency of 10 Hz.*

It is possible to observe as the transient current does not match with the expected trend for an ideal capacitor. Specifically, the charging and the discharging features are not symmetric, since the positive one is much sharper than its negative counterpart. This might be due to the free charges recombination mechanism in the active bi-layer which is not present in the classic capacitor.

Despite this fact, the integrated area below the curve, and hence the stored charge, are exactly the same for both the positive and negative peak. For this reason, the two are equally valid for the efficiency calculation, but the charging cycle has been chosen as a standard.

It is now interesting to note that even though the device is shined for 50 ms total (10 Hz), it only takes it around 10 ms to charge. This means that four fifth of the incident radiation energy goes to waste, decreasing the final $\eta_{ext}$ value. Before proceeding with further considerations, the way in which the light harvesting capacitor efficiency is computed is introduced:

$$E_p = \frac{Q^2}{2C}$$

*Eq. IV-1*

$$\eta_{ext} = \frac{E_p}{E_{light}} = \frac{E_p}{I_{light}\left({}^{1}/_{2f}\right)A}$$

*Eq. IV-2*

where $Q$ [C] is the stored charge, $C$ [F] is the overall capacitance, $I_{light}$ [W/m$^2$] is the light intensity, $A$ [m$^2$] is the device active area and $f$ [Hz] is the chopper frequency. From this it follows that increasing the frequency, up to a certain cap value, less light energy will go to waste improving the device performance as well. The effect of varying the chopper frequency on the transient current trend is shown in figure IV.7. Quite surprisingly, increasing the chopper frequency the photo-current trend itself changes. This is unexpected because, in theory, the charging and discharging cycles should only depend on the decay time of the separated charges. In the real device characterization, they should actually depend on the equivalent RC circuit time constant as well. However, in this case the device measured is always the same and only the frequency is changing. A possible explanation for this can be found in the way the dark-light cycles are generated through the chopper. More in details, even if the beam is made as small as possible, the passage from one state to the other is never instantaneous. When the chopper frequency increases though, this passage becomes sharper and sharper leading to a faster charging (and discharging) process. This can be easily observed from the graph in figure IV.7, looking at two specific changes occurring. Firstly, a faster charging process means greater amount of charge per unit time, hence higher current. In a second place, the peak shape itself is characterized by a higher slope.

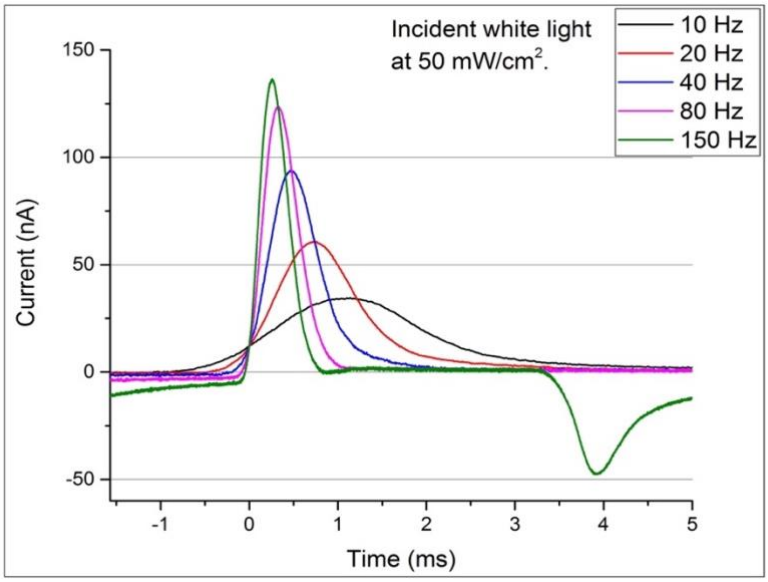


*Figure IV.7 Time resolved photo-current measured at different chopper frequencies under white light (I=50 mw/cm²).*

One effect that is not as easy to explain is related to the integrated area below the curves which decreases increasing the frequency, as reported in table IV.1. This is also not expected since, even if the process is faster, the amount of stored charge should ideally stay the same. An explanation might be found making a comparison with the so-called supercapacitors. In this kind of devices, which are basically a more efficient version of a classic capacitor, a faster process does not allow a correct penetration of the free charges in the dielectric materials. The correlation is not so straightforward, but a hint can nonetheless be found [7].

*Table IV.1. Stored charge and energy for the reference device at different frequencies.*

| Frequency [Hz] | Time [ms] | Stored charge [pC] | Stored energy [pJ] |
|---|---|---|---|
| 10 | 100.0 | 82 | 6.7 |
| 20 | 50.0 | 80 | 6.5 |
| 40 | 25.0 | 72 | 5.2 |
| 80 | 12.5 | 61 | 3.7 |
| 150 | 6.7 | 52 | 2.7 |

The capacitance used to calculate the stored energy was computed considering the different films thicknesses and dielectric constants, obtaining 0.5 nF. It was also measured experimentally finding matching values. After these considerations, the efficiency vs frequency plot can finally be reported in figure IV.8, to further analyze the effect of the changing frequency. It is possible to observe as, even though the amount of energy stored is lower, the $\eta_{ext}$ increases up to a maximum of 5.7 *$10^{-5}$% at 400

Hz. As a consequence, it can be safely assumed that the decrease in "wasted" energy, due the decrease in the difference between the light cycle time and the charging cycle one, is higher than the decrease in stored energy. This is only true up to a frequency value of 400 Hz, after which the efficiency starts to decrease again. It must be specified though, that different batches with the same reference device structure gave slightly different results for this frequency cap value, varying from 350 Hz to 400 Hz.

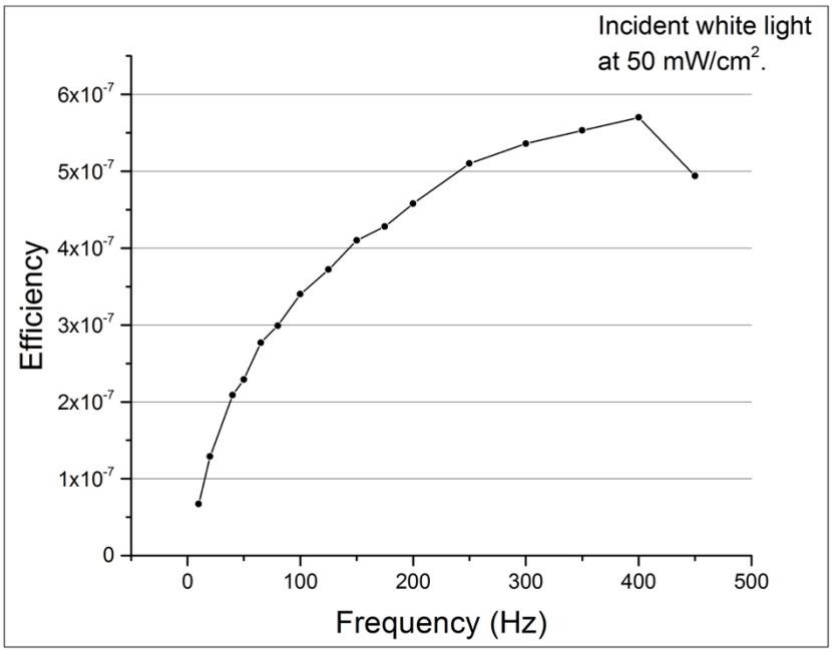


*Figure IV.8 Efficiency vs frequency trend for the reference device.*

All the standard procedures for light harvesting capacitors characterization and analysis have been introduced. Moreover, efficiency and photo-current values to use as comparisons have also been presented. At this point only one last step is needed before starting with new devices study: the effect of using titanium dioxide as an insulant layer will be reported in the next paragraph.

# IV.3 Titanium dioxide study

As already anticipated, titanium dioxide will be tested as one of the dielectric material together with PMMA and $ZrO_2$. However, since it is not a proper insulant, but rather a semiconductor, further studies are required. Its behavior within the device itself is observed and presented in this paragraph.

Due to its energy band levels, titania is usually exploited as an electron transport layer (ETL) when building perovskite devices. This layer is added to improve the charges conduction mechanism that is quite low in the active material itself [8]. As a consequence, it is also possible that when employed in a light harvesting capacitor, its behavior will differ from the other tested insulants.

In order to possibly observe any effect, two different device structures are tested: one where CuPc is sandwiched between two zirconia insulant layers, and a second structure where one of the two layers is replaced with titania. Both the symmetric and the asymmetric structures are reported in figure IV.9. The insulant thicknesses (also shown in figure IV.9) are chosen in order to achieve a higher capacitance for the $ZrO_2$-only device. The capacitance values computed (and measured) are 2.11 nF and 1.99 nF. The aim of this comparison is to observe as, replacing one of the two $ZrO_2$ layers, not only the device capacitance changes, but also the active behavior itself and thus the overall performance as well.

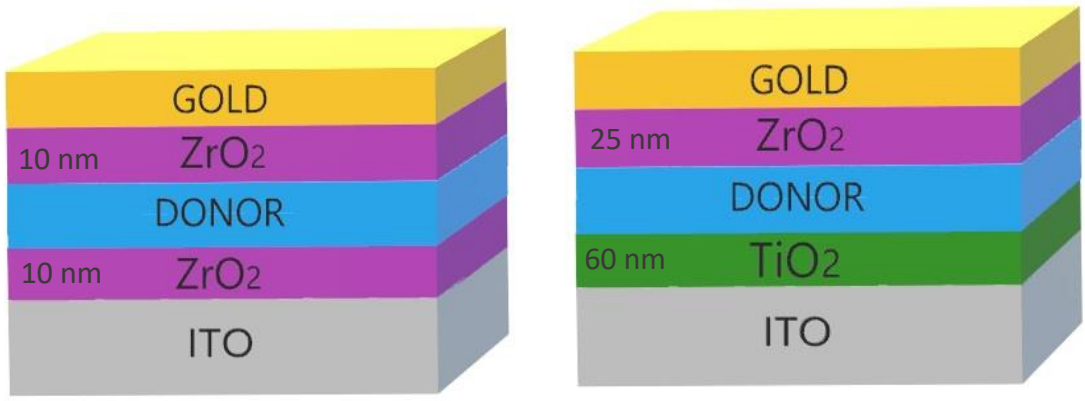


*Figure IV.9 Structure of both the devices tested with reported thicknesses of the insulant layers. On the left the symmetric and on the right the asymmetric one.*

The time resolved photo-current measurement for both the LHCs is reported in figure IV.10. It is evident that the photo-current, in the case where titanium dioxide is introduced, is definitely higher (by almost three times). This is contradictory, if the only difference between the structures is assumed to lie in the capacitance values. The device with the symmetric structure possesses a higher capacitance and hence it should show a higher current peak. Since this is not the case, it is obvious that titanium dioxide has to somehow affect the charging process itself. Integrating the photo-current, the efficiency values for both the devices can be obtained. Specifically, the LHC with a 25 nA current peak has a calculated efficiency of $1.6*10^{-6}$%, while the one with a 63 nA peak has an efficiency of $1.6*10^{-5}$%.

Considering that $TiO_2$ can be exploited to transport electrons, it is likely that it also behaves as an acceptor material. More in details, a sort of an extra D/A interface is expected, leading to an enhancement of the charge separation mechanism. This charge transfer can in theory be observed in the same way as for the classic small molecules interface: with ultra-fast transient absorption spectroscopy. Nevertheless, no real associated signal was observed with the transient analysis, possibly meaning that the signal and hence the transfer itself, were too weak.

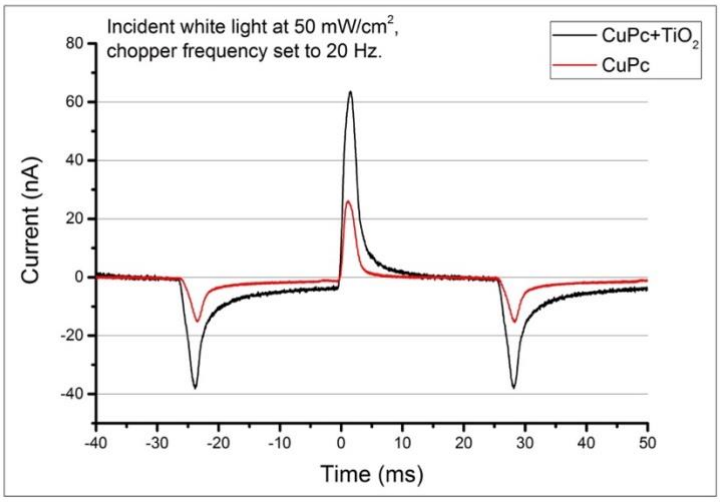


*Figure IV.10 Time resolved photo-current measurements for the two devices tested. Both are performed under white light (I=50 mW/cm$^2$) and with a chopper frequency of 20 Hz. The redline is the symmetric structure and the blackline the asymmetric one.*

It must be specified at this point, that different titania thicknesses were tried before achieving the expected LHCs behavior: using layers thinner than 60 nm, leads to a leakage current during the device testing. This leakage can be observed as a background current that shifts up the base line for the positive cycle; It can also be observed as a DC signal when the device is shined with constant light. The reason behind this lays in the fact that too thin layers do not allow a proper insulation. Despite this fact, when $TiO_2$ is employed as insulant layer in the bi-layered LHCs, lower thickness values are tried nonetheless. This is done because in the presence of a real D/A interface, the charge separation mechanism is expected to occurs mainly at that interface. Now that the preliminary study is completed, the actual testing of the new LHCs structures can finally start.

# IV.4 Thickness dependence

The first dependence that is studied and presented is the insulant layer thickness one. In this paragraph the effect of its variation on the photo-current is illustrated for all the dielectric materials exploited. Specifically, these are poly (methyl methacrylate), zirconium dioxide and titanium dioxide are employed with the three structures shown in figure IV.11. No efficiency value is given, since there will be a later section that will be focused exclusively on it. The photo-current is reported in three separated figures for the three materials tested, and each of them contains three different insulant layer thicknesses. Only the positive peak is shown to better observe the variation.

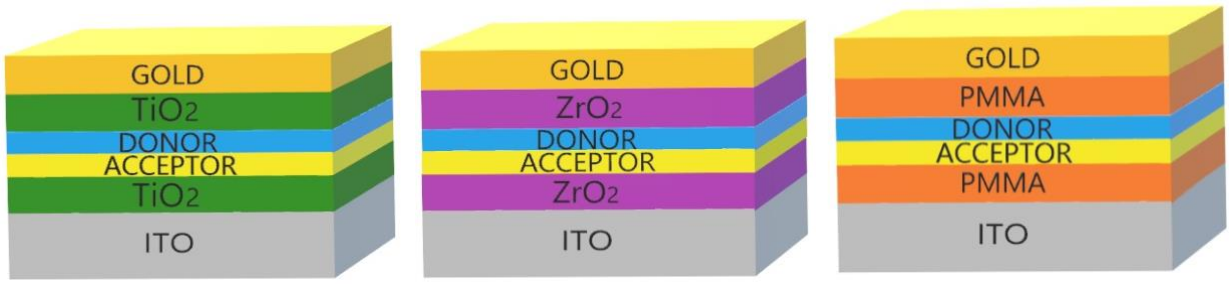


*Figure IV.11 Structure of the three devices tested. No thickness value is reported since it will be varied during the testing.*

Figure IV.12 shows the time-resolved current measurements performed on the three different PMMA thicknesses. The increase in the peak intensity is extremely evident. Changing from 150 nm to 100 nm the value is more than doubled and the same is quite true when changing from 100 nm to 25 nm. The three current maxima are respectively 23 nA, 60 nA and 115 nA.

It is interesting to note that from one thickness to another, the rise of the peak is not the only variation present: the peak also gets larger. This means that the process is getting slower. Fitting the three trends with an exponential decay curve, an approximated value of the characteristic time $\tau$ can be obtained. The three values are 0.59 ms, 0.61 ms and 0.80 ms. As already mentioned before, the charging process itself should only depend on the active layer, but when the measurement is done on a real device, other parameters influence it as well. In this case, what is changing is the overall capacitance of the device that, assuming an RC circuit, will then influence the time of the charging process.

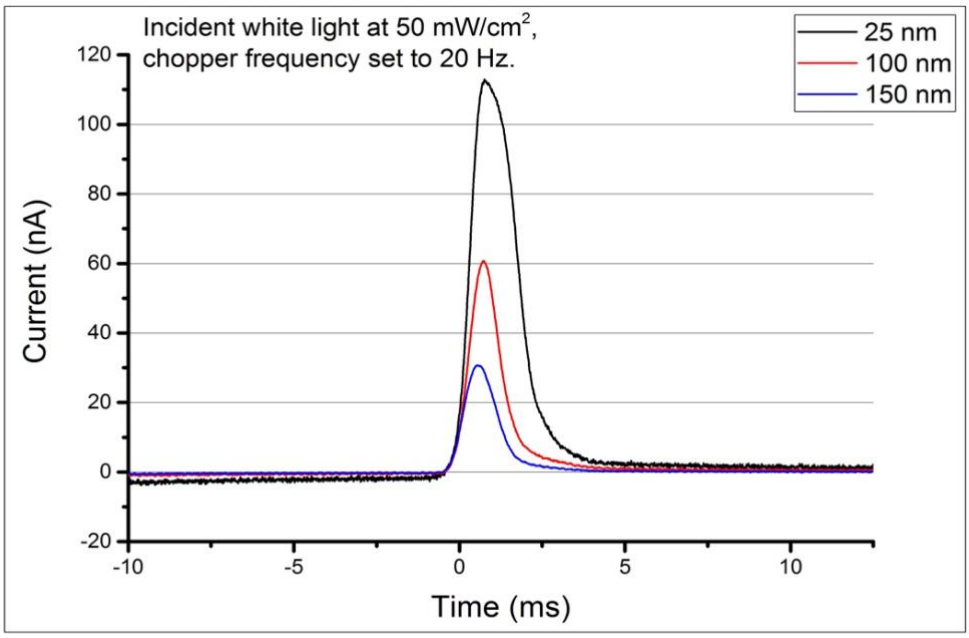


*Figure IV.12 Time resolved photo-current measurements for three different PMMA thicknesses. All the measurements are performed under white light (I=50 mW/cm$^2$) and with a chopper frequency of 20 Hz.*

Figure IV.13 shows instead the three photo-current measurements obtained for the different $ZrO_2$ thicknesses. Once again, the increase in the peak intensity is evident, but this time changing the insulant layer thickness is not as effective as before. When passing from 50 nm to 25 nm the current goes from 150 nA to 275 nA , while at 10 nm the current is 370 nA. This kind of behavior was expected even from the simulations presented in chapter II. The reason is that when the capacitance is already quite high, it increases more slowly. For the zirconia case, the three computed (and measured) capacitances are 1.4 nF, 1.5 nF and 1.6 nF. On the other hand, in the PMMA devices they were 0.37 nF, 0.50 nF and 1.0 nF.
The increase in capacitance leads one more time to a slower charging process, even if in this case it is not as marked as before. This is confirmed by the characteristic decay times obtained by the fitting of the three curves. The 50 nm has a $\tau$ of 0.84 ms, the 25 nm of 0.87 ms and the 10 nm of 0.98 ms.

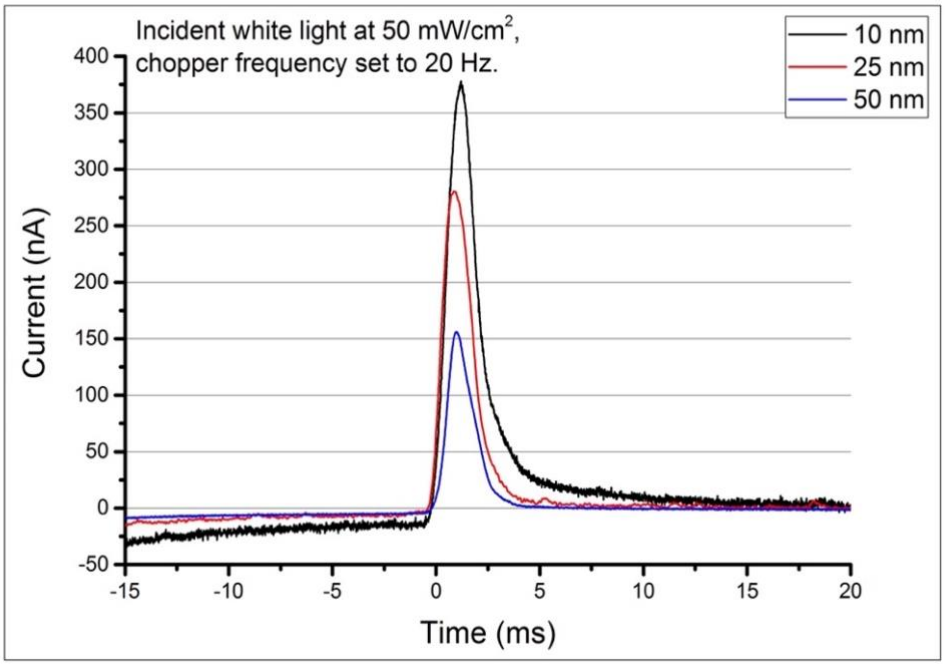


*Figure IV.13 Time resolved photo-current measurements for three different $ZrO_2$ thicknesses. All the measurements are performed under white light (I=50 mW/cm²) and with a chopper frequency of 20 Hz.*

Finally, figure IV.14 shows the photo-currents for the three titanium dioxide thicknesses. In this case the starting capacitance is even higher than before, and that is why the current maximum increase from 25 nm to 10 nm thick layer is not as striking as before. The two peaks are 600 nA and 805 nA, while the two capacitances are respectively 1.64 nF and 1.67 nF. Actually, the third and lowest thickness value that was tested, was not working as proper light harvesting capacitor. Specifically, with a layer as thick as 5 nm, it appears that $TiO_2$ does not behave as an insulant anymore. The same was observed in paragraph IV.3, where the minimum thickness to achieve a proper LHC behavior was 60 nm. However, with a proper D/A interface the lowest acceptable thickness seems to be much lower (10 nm). To better understand the DC

current that was mentioned earlier, the thinnest device photo-current is reported in figure IV.14 under continuous illumination. Since the constant current is much lower if compared to the two transient values, two different scales are exploited. Higher thickness values (i.e. 50 nm) could not be fabricated in a sandwiched structure (such as the one required for the LHC) because of the ALD process limitation.

It is interesting to note that the characteristic times of the process are much longer than the one reported for the PMMA and the $ZrO_2$ devices. Looking at the capacitance values, the expected increase in times should not be too high, however the two $\tau$ are 1.8 ms and 2.6 ms. With the measurement performed at 20 Hz it even appears that the discharging cycle, which for a LHC device is always slower than the charging one, has not enough time to be completed. The reason behind this might be found in the active contribution given by titanium dioxide reported in the previous section. It was observed that this material does not simply insulate the active layer, but it forms a sort of secondary interface with the small molecules. Considering this, it is possible that a further dipole formation occurs, leading to a slower, but stronger charging process for the overall device.

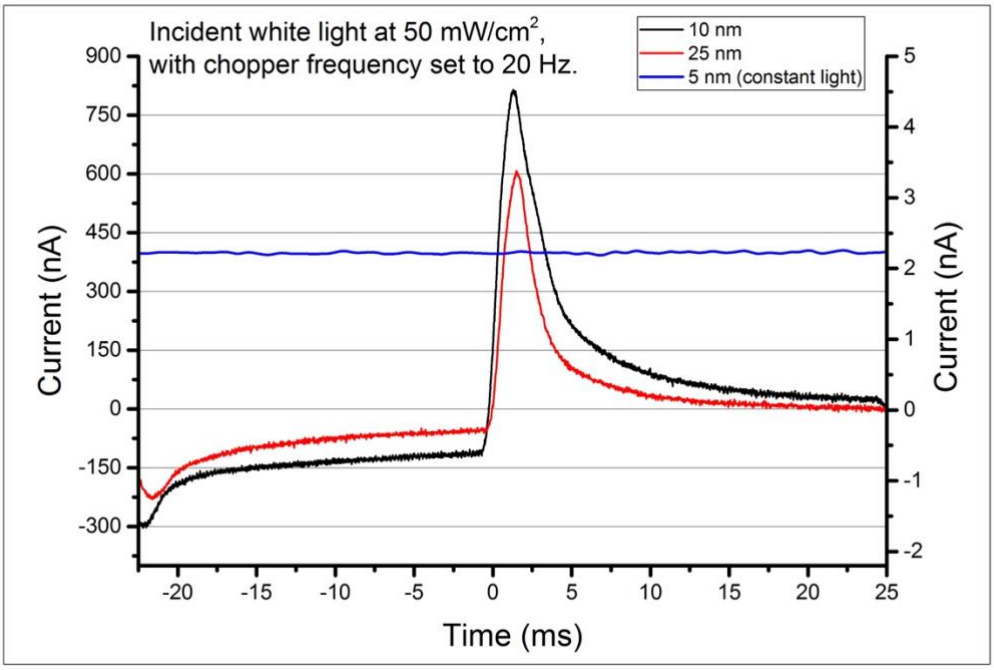


*Figure IV.14 Time resolved photo-current measurements for three different $TiO_2$ thicknesses. All the measurements are performed under white light (I=50 mW/cm$^2$). The black and the red line are obtained with a chopper frequency of 20 Hz, while the blue line is achieved under constant illumination.*

The overall comparison and efficiency analysis, reported in a later section, will help to further study this mechanism. In the next paragraph the analysis will be focused on the photo-current curves obtained for three different devices. The insulant thickness considered is constant, while the material varies between PMMA, $ZrO_2$ and $TiO_2$.

# IV.5 Insulant material dependence

The aim of this paragraph is to directly compare different insulating materials, keeping the thickness constant. This is done to better observe the effect of changing the material and the fabrication technique on the photo-current trend. Figure IV.15 reports the time resolved measurements for the three devices tested. The structures considered are the same shown in figure IV.11, although here the insulant thickness is fixed at 25 nm. The three capacitance values are respectively 1.06 nF for PMMA, 1.54 nF for $ZrO_2$ and 1.64 nF for $TiO_2$.

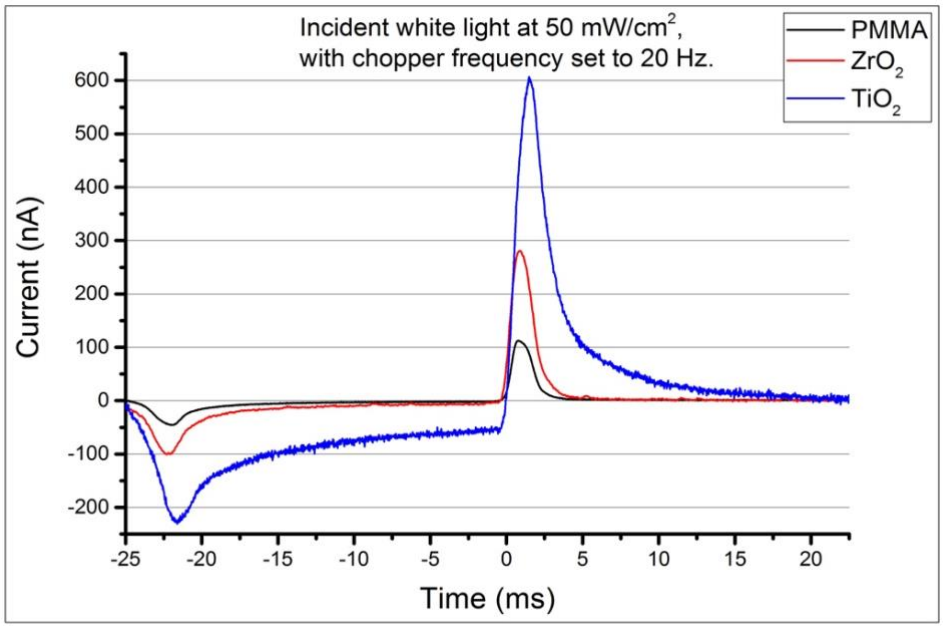


*Figure IV.15 Time resolved photo-current measurements for the three different 25 nm thick insulant materials. All the measurements are performed under white light ($I=50\ mW/cm^2$) and with a chopper frequency of 20 Hz.*

It is clear that, according to these capacitance values, the current increase should be much bigger when passing from PMMA to $ZrO_2$. However, even when changing to $TiO_2$ the increase is also rather marked. Specifically, the three peak maxima are 115 nA, 275 nA and 600 nA. These results were somehow expected, since in the two previous paragraphs the anomalous behavior for titania was observed, highlighting how the presence of this material leads to the creation of a secondary interface with the small molecules. The consequence is the generation of extra-dipoles that increases the amount of stored energy in the device and hence the current maximum. Obviously, this also causes the charging and discharging processes to be much slower, as shown in figure IV.15.

The next paragraph will finally focus on the devices efficiency itself, and it will help to further develop the study of the LHCs so far reported and to better understand their working mechanism.

# IV.6 Efficiency study

In this paragraph, starting from the photo-currents obtained for the devices presented so far, the efficiency is calculated. As shown with the reference LHC, the positive feature of the trend is first integrated over time to obtain the stored charge. At that point, the stored energy is derived using the overall capacitance as in eq. IV.1 and then the efficiency is finally computed based on eq. IV.2. The study focuses firstly on the different thicknesses comparison and secondly on the different insulants. After that an overall evaluation is performed. It must be specified that different chopper frequencies are exploited in this efficiency analysis. A comparison with the values obtained using the MATLAB model developed in chapter II will be also reported. The active parameters considered in the simulations are 4 nm dipole size and 10 ms decaying time. Finally, in the last part of the current section, a study of the LHC internal quantum efficiency (IQE) under a green laser is recounted.

## IV.5.1 Insulant layer thickness

To further analyze what was previously described in paragraph IV.3, the efficiency values obtained for those devices structures (fig. IV.11) are here reported. The dependency of the LHCs performance varying the thickness for three different insulants is studied. The first material that is considered is PMMA and its efficiency trend as function of frequency is illustrated in figure IV.16.

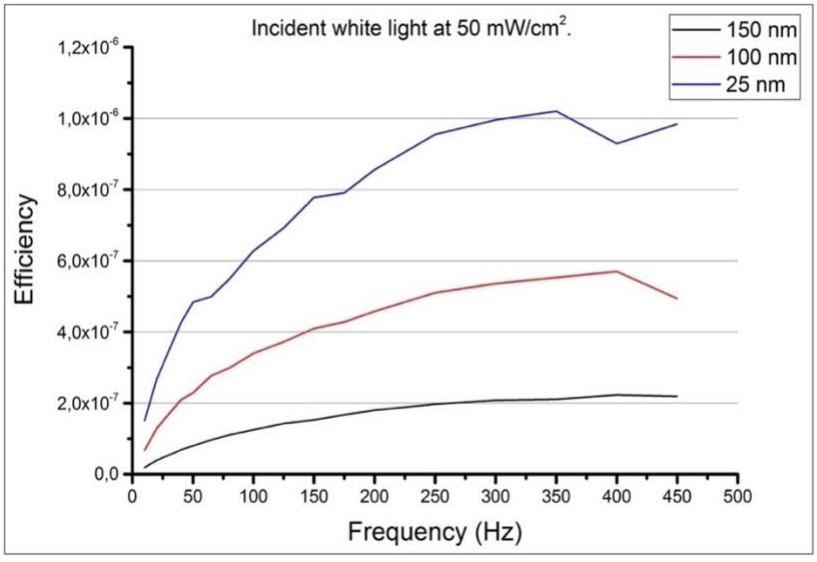


*Figure IV.16 Efficiency vs frequency trend for the three PMMA LHCs. The white light intensity employed is 50 mW/cm².*

As observed with the reference device, the efficiency increases with the frequency up to a certain maximum value which ranges from 350 Hz to 450 Hz. It seems like the slower is the charging process the lower is the frequency cap. This makes sense considering that for a slow process the amount of "wasted" radiation energy at a certain frequency is smaller. This can be easily seen by looking back at figure IV.12 where it is evident that the black line (25 nm) takes up the greatest portion of the light cycle. The 25 nm thick PMMA LHC, which is the one with the biggest characteristic time out of the three, is in fact the first to reach the cap value. The three efficiency maxima obtained are $2.44*10^{-5}$%, $5.70*10^{-5}$% and $1.05*10^{-4}$%, while the minima are $2.10*10^{-6}$%, $6.74*10^{-6}$% and $1.21*10^{-5}$%. Between these values there is almost a factor of ten, meaning that the frequency optimization is fundamental to reach the best device performance. Comparing these values with the one predicted by the simulations developed in chapter II (0.26%, 0.36% and 0.89%), it is clear that the device is far from optimized. However, it is nonetheless interesting to compare the ratios obtained between the different LHCs measured efficiencies and between the ones obtained with the simulations. Changing from 150 nm to 100 nm the simulated ratio is 1.38, while the measured one is 2.33. Passing instead from 150 nm to 25 nm, the ratios are 3.42 and 4.3. Even though the real ratios are higher than the simulated ones, the thickness dependence predicted by the model can be assumed to be correct. The difference between the two might be attributed to a decrease of the resistance due to the smaller insulant layer thickness. A second possible explanation might be found in the different layer homogeneity obtained using different concentrations of the spin-coated solution.

The second kind of LHCs considered in this paragraph is the one exploiting zirconia as insulant layer. The resulting efficiencies are reported in figure IV.17.

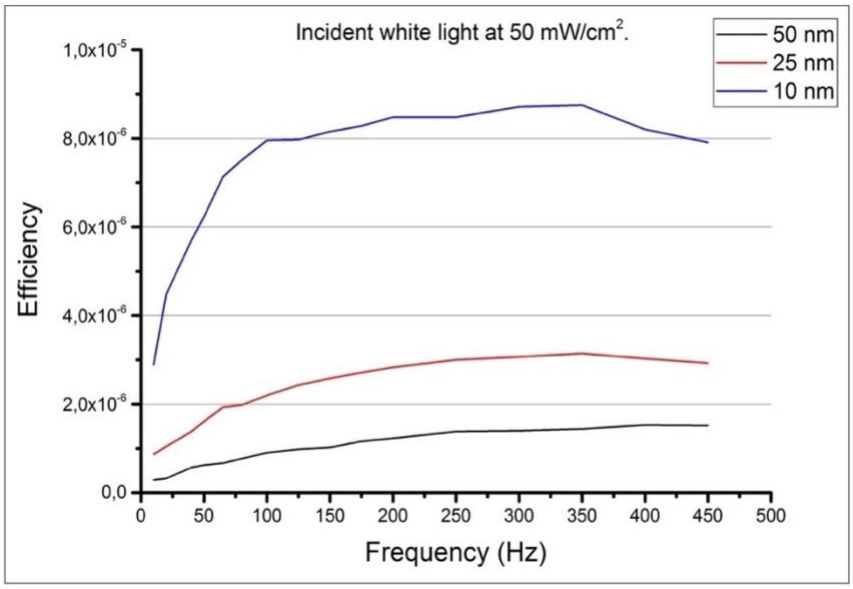


*Figure IV.17 Efficiency vs frequency trend for the three $ZrO_2$ LHCs. The white light intensity employed is 50 mW/cm².*

The increasing trend at the increasing frequency is observed straightaway. The three maxima calculated values are $1.53*10^{-4}$%, $3.14*10^{-4}$% and $8.75*10^{-4}$%, while the three minima are $2.89*10^{-5}$%, $8.69*10^{-5}$% and $2.89*10^{-4}$%. Once again it seems that the slowest process, which is associated to the 10 nm thick zirconia layers, reaches the efficiency cap at the lowest frequency. In the case of these devices, especially for the thinnest one, it also looks like the efficiency increases much faster than in the previous kind. Even though the actual cap is around 350 Hz, the slope steepness that precedes it is rather low, and most of the increase is concentrated in the first 150 Hz, meaning a slower process.

The simulated values for these three devices, which are used as a comparison, are 1.34%, 1.52% and 1.70%. Once again, the measured values are definitely lower, but this was expected since the active bi-layer was fabricated in the same batch to better observe the direct influence of the dielectric layer on the light harvesting capacitor. As in the previous case, it is useful to compare the efficiency ratios between the different thicknesses. Decreasing by half the thickness, the simulated ratio is 1.13, while the calculated one is 2.05. Decreasing instead the final thickness to a fifth of the original number, the simulated value is 1.26 and the calculated is 5.71. Even if these ratios are more different than the ones obtained for PMMA, the predicted thickness dependency can again be assumed to be rather correct. The differences that are found are probably related once again to the overall resistance that changes from one device to another. However, this is not enough to explain such a big difference, and a second possible phenomenon influencing the performance can be found in the zirconia fabrication process itself. As explained in chapter III, the thermal evaporation of this material requires very high temperatures. Since evaporating 50 nm takes much longer than evaporating 25 nm, which in turn takes much longer than 10 nm, the active bi-layer of the thinnest device is definitely less thermally stressed. The homogeneity of the three layers should more or less stay the same with the varying thickness and should not influence as much as it does in the PMMA case.

The last insulating material considered is titanium dioxide and its related efficiency values are shown in figure IV.18 for both the 25 nm thick LHC and the 10 nm one. The 5 nm device is not reported here since its behavior is not a proper one and hence the efficiency cannot be calculated. The maximum efficiencies are $1.73*10^{-3}$% and $5.75*10^{-3}$%, thus a 3.3 improvement ratio is obtained. These two values are achieved respectively at 80 Hz and at 10 Hz. This is quite surprising, even considering that a slower process caps at a lower frequency. The characteristic time associated to the titanium dioxide LHC is not big enough to justify a frequency cap either at 80 Hz or at 10 Hz. The phenomenon explanation might be found once again in the atypical $TiO_2$ behavior as an insulant material. Specifically, it might be found in the extra interface created between titania and the small molecules, that leads to the generation of extra dipoles. It is possible that the extra generation requires more time than the normal one, meaning that a too high

frequency does not allow the attainment of the full process. It appears that for the device with 10 nm titanium dioxide layers, this is even more marked since the efficiency starts to drop right after 10 Hz.
In this last case (titania based LHC) the values obtained through the MATLAB simulation are 1.67% and 1.72% while the ratio between the two is 1.03. It is evident that the simulated and the measured ratios are again rather different and this time it is probably due to the same reason found for the low frequency cap. However, the efficiency vs thickness dependence predicted by the model can finally be confirmed.

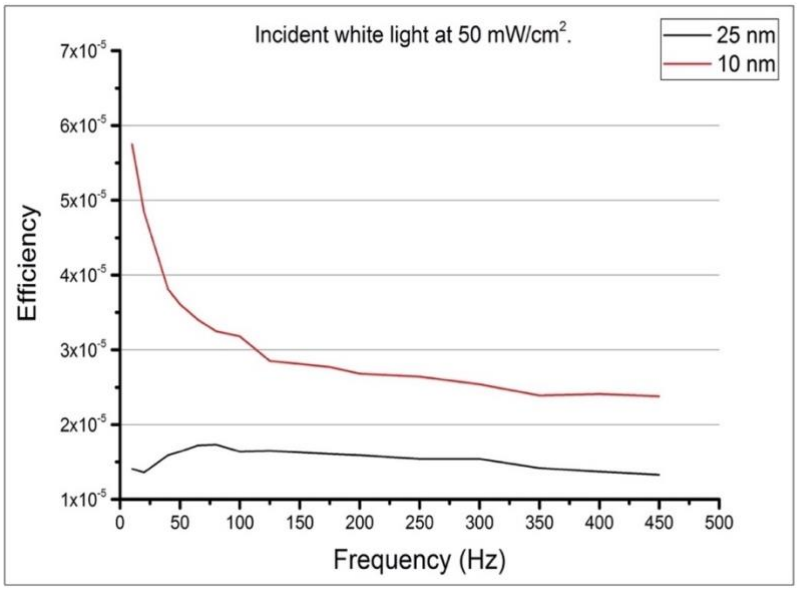


*Figure IV.18 Efficiency vs frequency trend for the two $TiO_2$ LHCs. The white light intensity employed is 50 mW/cm².*

One last remarkable observation is that the measured values are way closer to the predicted ones than in the other two cases. Considering that the active bi-layer is fabricated at the same time on all the devices, this must be related to the insulant layer itself. As a consequence, this is a further proof that $TiO_2$ does not simply insulate the evaporated small molecules, but rather it cooperates with them in the dipoles generation. This means that using $TiO_2$ as an insulant layer is possibly the best way to improve the device performance. Other confirmations on the matter will be given in the next two sections as well.

## IV.5.2 Insulant layer material

The aim of the following section is to report an efficiency comparison between the structures analyzed in paragraph IV.4. Figure IV.19 shows the trends obtained for the three different 25 nm thick insulant layers studied. The maximum efficiency values measured are $1.05*10^{-4}$%, $3.14*10^{-4}$% and $1.73*10^{-3}$%, while the simulated ones are 0.89%, 1.52% and 1.67%. Again, the simulated ratios (i.e. 1.71 and 1.87) are lower

than the experimental ones (i.e. 2.99 and 16). It must be noted that, while the prediction for the change from PMMA to $ZrO_2$ is quite acceptable, hence indicating a good model, the second prediction is too distant from the reality. This is another good indication of the active contribution of $TiO_2$ to the dipole moment generation, contribution that is not considered in the MATLAB simulation.
Finally, before starting with the overall comparison, it also interesting to focus on the frequency caps for the three LHCs. As observed in the previous passage, the $TiO_2$ device has an extremely low cap value, in any case the direct comparison with the other two insulants exploited, allows to better witness this quite outstanding difference.

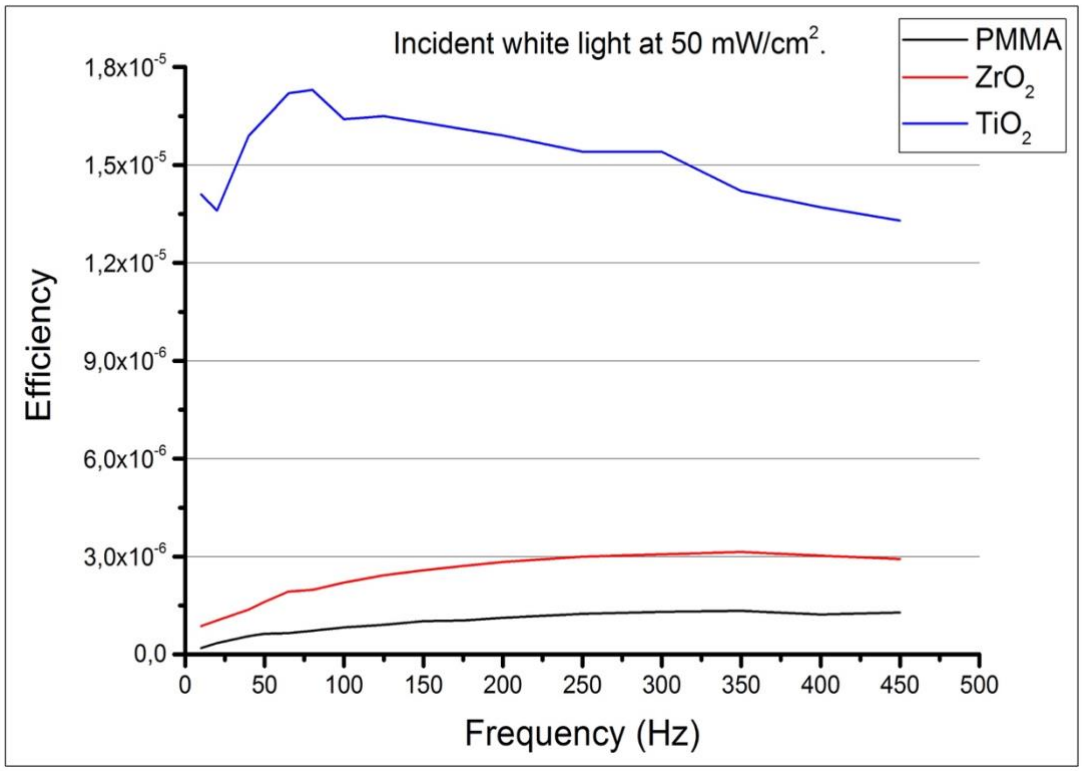


*Figure IV.19 Efficiency vs frequency trend for the three insulating materials tested. The dielectric layer thickness is fixed to 25 nm and the white light intensity employed is 50 mW/cm².*

## IV.5.3 Overall comparison

Now that all the different dependences for both the photo-current and the efficiency have been analyzed, an overall comparison between all the devices tested can be carried out. Figure IV.20 shows the charging feature of the time resolved current trend for the eight devices considered obtained at 20 Hz chopper frequency. In order to better observe the effect of varying the insulant layers, the active bi-layer has been fabricated in the same batch for all the LHCs.

It is possible to note a general increase of the charging peak at the increasing capacitance. When moving from the 150 nm thick PMMA capacitor to the 10 nm thick $TiO_2$ one, the measured current goes from 23 nA to 805 nA. This peak rise is quite remarkable and gives a calculated improvement ratio of 35 times. It is also interesting to note the feature enlargement which follows the same tendency. Specifically, the higher is the capacitance and the larger is the peak. This means a slower charging process, as already shown in the previous paragraphs and as described by the characteristic time summarized in table IV.2.

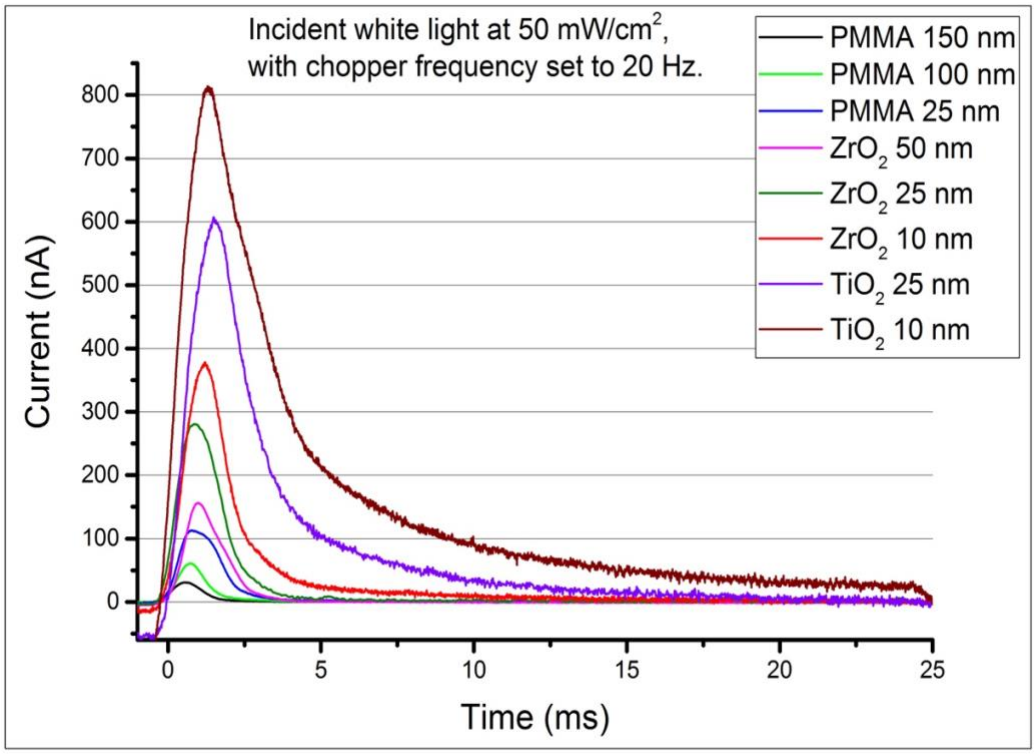


*Figure IV.20 Time resolved photo-current measurements for all the LHCs tested. All the measurements are performed under white light (I=50 mW/cm²) and with a chopper frequency of 20 Hz.*

With all the current trends shown in one graph it is easier to note that the devices containing $TiO_2$ are way slower than all the others. More in details, the 10 nm one takes up to 25 ms to complete the charging feature, while the PMMA and zirconia based never need more than 7 ms. Looking at table IV.2, it is also possible to have an overview of the frequency cap values that were discussed formerly. A general decrease, which goes in agreement with the increasing $\tau_{charge}$, is discernable. Once again, the abnormal behavior associated to the last two devices (reported in red) is rather evident since the cap decreases by 5 times in one case and by more than 30 times in the other. It is important to specify that the current values reported in this table are not the same achieved at the frequency cap, but they only express the peak intensity at 20 Hz.

*Table IV.2. Summary of all the main data obtained by every device produced and characterized.*

| Material | Thickness [nm] | C [nF] | $I_{20\ Hz}$ [nA] | $\tau_{charge}$ [ms] | $f_{cap}$ [Hz] | $Q_{max}$ [nC] | $\eta_{max}$ *$10^{-6}$ |
|---|---|---|---|---|---|---|---|
| PMMA | 150 | 0.37 | 23 | 0.59 | 450 | 0.02 | 0.24 |
| | 100 | 0.50 | 60 | 0.61 | 400 | 0.04 | 0.57 |
| | 25 | 1.05 | 115 | 0.80 | 350 | 0.09 | 1.34 |
| $ZrO_2$ | 50 | 1.42 | 150 | 0.84 | 400 | 0.14 | 1.53 |
| | 25 | 1.54 | 275 | 0.87 | 350 | 0.22 | 3.14 |
| | 10 | 1.62 | 370 | 0.98 | 350 | 0.29 | 8.75 |
| $TiO_2$ | 25 | 1.64 | 600 | 1.80 | 80 | 1.13 | 17.30 |
| | 10 | 1.67 | 805 | 2.60 | 10 | 5.87 | 57.50 |

At this point the focus of the comparison can shift to the efficiency of the devices and in particular to the maximum values achieved for each of them. Increasing the capacitance leads to the increase of the performance, as predicted by the theoretical model. Notwithstanding this, while the prediction is reasonably correct for the first two kinds of material, it becomes rather inaccurate for the last kind. For instance, changing from $ZrO_2$ 10 nm to $TiO_2$ 25 nm, the capacitance increases only by 1.01 times while the efficiency is almost doubled. This can be considered as a final proof that the titanium dioxide layers contribute to the photo-generation of separated charges and thus to the LHC charging process.

Now that all the necessary evaluations have been completed, it is safe to affirm that the exploitation of titanium dioxide for both the insulant layers leads to the best device structure out of all the ones tested. This is somewhat unforeseen considering that titania was not expected to possess proper insulant properties. Despite the fact that this expectation is actually correct, the $TiO_2$ peculiar behavior gives a positive effect on the light harvesting process rather than a negative one. To conclude this section dedicated to the efficiency, one last study is presented: internal quantum efficiency.

## IV.5.4 Internal quantum efficiency

In this section of the efficiency study, a monochromatic light source is used on the reference LHC to calculate the internal quantum efficiency. Looking at the internal efficiency is helpful to understand whether the external one is limited by the absorption or by other factors. A green LED emitting at 532 nm is used and, according to the CuPc absorption spectrum, the absorption at this specific wavelength is equal to 7%. Knowing this and the calculated external quantum efficiency, the internal one can be promptly computed as follow:

$$\eta_{int} = \frac{\eta_{ext}}{\alpha}$$

*Eq. IV-3*

where $\alpha$ is the absorbed fraction of the total incident radiation, namely 0.07. Figure IV.21 shows both the EQE and the IQE vs frequency trends. The two maximum values obtained are respectively $1.66*10^{-4}$% and $2.33*10^{-3}$%. It is evident that in the LHC case, since the internal efficiency is rather low too, the problem behind the limited performance has to be in the energy harvesting mechanism itself.

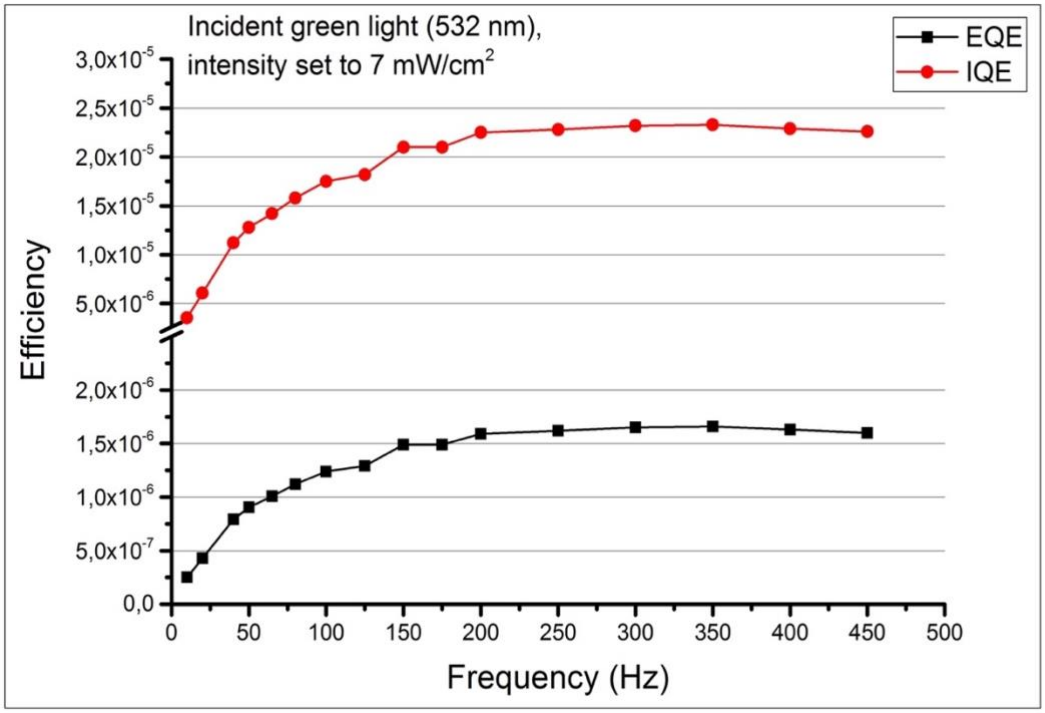


*Figure IV.21 Internal and external quantum efficiency vs frequency trends for the reference LHC. The light source is a 532 nm green LED with intensity set to 7 mW/cm².*

# IV.7 Light intensity study

According to the model developed in chapter II and specifically to equation II.10, which considers all the possible dependences, the LHC efficiency should increase linearly with the incident light intensity. This is usually not the case for classic PV and OPV solar cells, where the light intensity gets cancelled when doing the ratio between produced and incident energy [9]. In the present case however, the intensity enters squared in the stored energy and hence influences the final efficiency value. In order to verify what the model predicted, the reference device (whose structure was presented in figure IV.5) is tested at fixed chopper frequency under different incident light intensities. A further study is done with a lock-in amplifier and will be shown in the last part of this section.

The different time resolved photo-currents obtained at 10 Hz are reported in figure IV.22. While the peaks height increases, at the same time its width decrease, and if the first effect was rather predictable, the second one is definitely unexpected. Specifically, a thinner peak means that the capacitor charging process is getting faster. A possible explanation might be related to a faster dipoles generation within the active layer itself. To verify whether this has an impact on the efficiency or not, the curves must be integrated to calculate the stored charge.

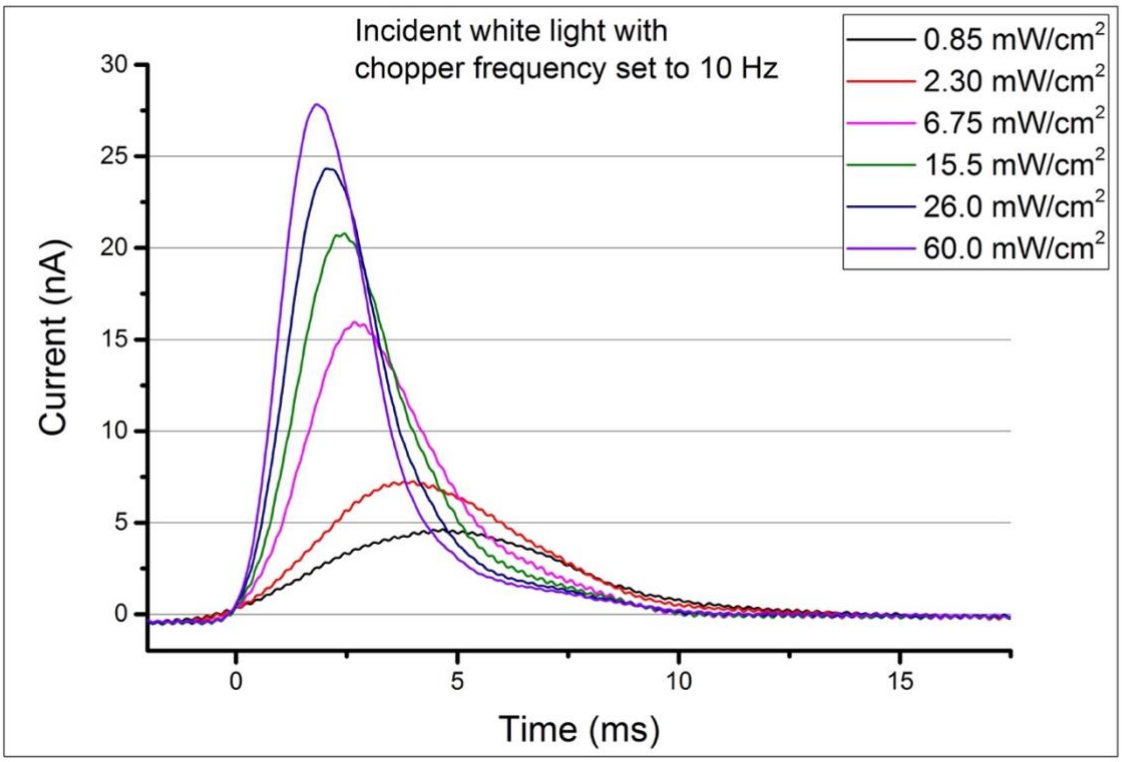


*Figure IV.22 Time resolved photo-current performed on the reference device under white light at different intensity. The chopper frequency is set to 10 Hz.*

Table IV.3 contains the data obtained by the manipulation of the photo-current trends shown in figure IV.22. Specifically, the peak maximum, the stored charge and the calculated efficiency are given for each radiation intensity tested. It is evident that the model prediction might be fundamentally wrong. Not only the efficiency does not improve, but it does not even remain constant as in all the other light harvesting technologies.

Apparently, with the process getting faster, the stored charge does not increase in a linear way with the intensity as expected. More in detail, the charge increases by only 4 times while the intensity was increased by 70 times. Considering this is enough to understand why the efficiency starts decreasing, but the reason behind the unexpected small Q increase is not clear yet.

*Table IV.3. Light intensity dependence of different data obtained at a 10 Hz chopper frequency.*

| Light intensity [mW/cm$^2$] | $I$ [nA] | $Q$ [pC] | $\eta$ *10$^{-7}$ |
|---|---|---|---|
| 0.85 | 4.8 | 19.9 | 2.1 |
| 2.30 | 7.4 | 31.1 | 1.9 |
| 6.75 | 16.2 | 47.0 | 1.8 |
| 15.50 | 20.8 | 52.3 | 1.1 |
| 26.00 | 24.5 | 60.5 | 0.7 |
| 60.00 | 27.9 | 72.9 | 0.4 |

Bearing in mind that a similar effect (a faster charging process) can be also obtained increasing the frequency, a second light intensity dependence was checked at 200 Hz and the results are reported in table IV.4. In this case it is possible to observe that up to the fourth intensity tried, the efficiency increases. Despite the fact that the performance improvement is not linear as predicted, these data contain a hint that the model might still be correct. More in details, it is possible that the way the efficiency is calculated in practical terms is not completely accurate. This consideration is done on the basis that no frequency dependence is present in the theoretical prediction. In the actual measurement however, a higher frequency allows to achieve a sharper passage from light to dark, while at the same time decreasing the amount of stored charge. As a consequence, a sharper transition might be what leads to the efficiency vs intensity trend observed at 200 Hz. Moreover, it is also important to note that at higher frequencies the amount of "wasted" light is smaller and this might affect the intensity dependence as well. However, even after all this consideration, why does the stored charge not increase linearly is still not clear. A fundamental mistake in the way the measurement is performed might be the key, but further studies need to be done.

*Table IV.4. Light intensity dependence of different data obtained at a 200 Hz chopper frequency.*

| Light intensity [mW/cm$^2$] | $I$ [nA] | $Q$ [pC] | $\eta$ *10$^{-7}$ |
|---|---|---|---|
| 0.85 | 6.2 | 9.0 | 8.5 |
| 2.30 | 12.2 | 16.0 | 9.9 |
| 6.75 | 42.3 | 30.0 | 11.9 |
| 15.50 | 58.2 | 36.5 | 17.6 |
| 26.00 | 70.1 | 42.2 | 9.7 |
| 60.00 | 79.5 | 44.6 | 6.8 |

At this point, trying to unravel these enigmatic results, a new way to test the device is presented: the lock-in amplifier. What is actually being measured by this instrument in the present case is not well-defined. As explained in chapter III, when measuring a non-pure sinusoidal function, the lock-in only gives as output the first harmonic. The function that is obtained with a chopped light source applied on a LHC is the one measured with the oscilloscope which is not a pure sine. As a consequence, only the first harmonic of the transient photo-current will be given as output. It is obvious then, that even this method is not the right one to test light harvesting capacitors. Despite that, the results are still valuable in the study of the light intensity dependence and that is why they are reported in figure IV.23.

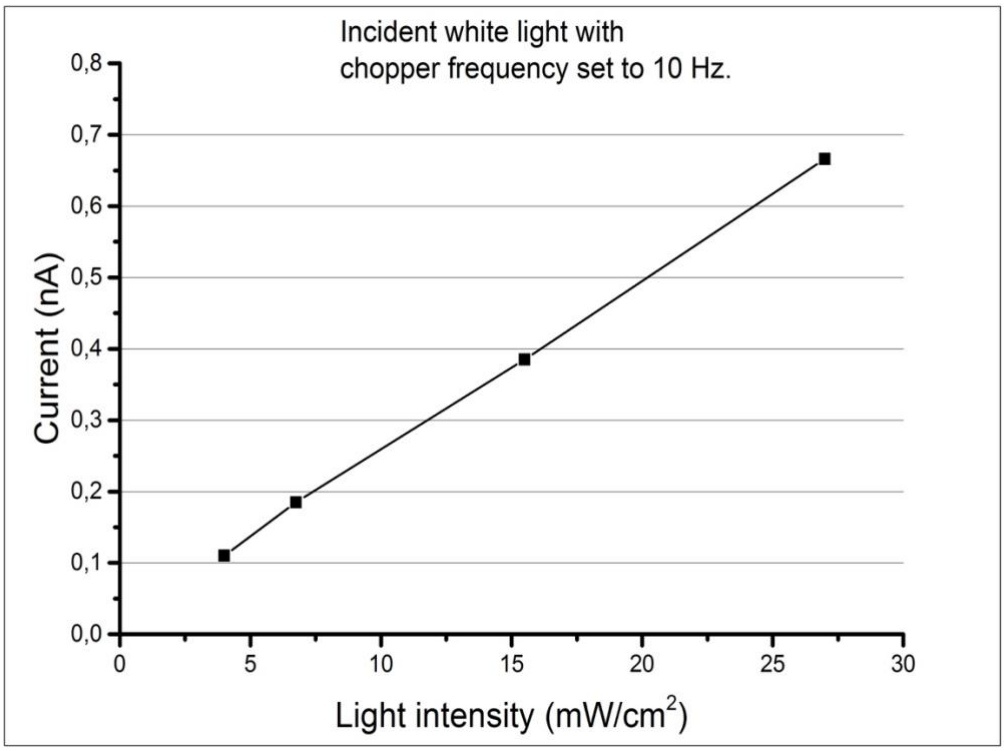


*Figure IV.23 Photo-currents values obtained with a lock-in amplifier under white light and a chopper frequency set to 10 Hz.*

The photo-current obtained is only proportional to the actual generated one, moreover it cannot be integrated to calculate the stored charge and hence the efficiency. However, it is interesting to observe that in this case the current almost increases linearly with the radiation intensity. Specifically, the former increases by 6.1 times while the latter by 6.8. These results might be a further proof that the model is actually correct, and that the problems lays in the way the efficiency itself is calculated.

Now that all the measurements have been presented and discussed, a greater understanding of the device working principle is achieved. Nevertheless, there is still a lot of work that needs to be done and some suggestions will be given in the next chapter together with some final considerations.

# Bibliographic References

[1] M. Garbugli *et al.*, “Light energy harvesting with nano-dipoles,” *Nanoscale*, vol. 4, no. 5, p. 1728, 2012.

[2] G. Paternò, F. Cacialli, V. Garcìa-Sakai, “Structural and dynamical characterization of P3HT/PCBM blends”, Chemical Physics, vol. 427, pp. 142-146, 2013.

[3] C. W. Tang, “Two-layer organic photovoltaic cell,” *Appl. Phys. Lett.*, vol. 48, no. 2, pp. 183–185, 1986.

[4] B. W. Caplins, T. K. Mullenbach, R. J. Holmes, and D. A. Blank, “Femtosecond to nanosecond excited state dynamics of vapor deposited copper phthalocyanine thin films,” *Phys. Chem. Chem. Phys.*, vol. 18, no. 16, pp. 11454–11459, 2016.

[5] W. Zilong, “PLASMON-POLARON COUPLING IN CONJUGATED POLYMERS ON,” 2015.

[6] K. Sendai, “ELECTRON TRANSFER OF ( C60 AND C70 ) STUDIED BY NEAR-IR REGION,” vol. 23, no. 5, pp. 389–402, 1997.

[7] J. Z. Aiping Yu, Victor Chabot, "*Electrochemical supercapacitors for energy storage and delivery*.", 2013.

[8] M. A. Green, A. Ho-Baillie, and H. J. Snaith, “The emergence of perovskite solar cells,” *Nat. Photonics*, vol. 8, no. 7, pp. 506–514, 2014.

[9] L. M. Cowen, J. Atoyo, M. J. Carnie, D. Baran, and B. C. Schroeder, “JSS FOCUS ISSUE ON THERMOELECTRIC MATERIALS & DEVICES Review — Organic Materials for Thermoelectric Energy Generation,” vol. 6, no. 3, pp. 3080–3088, 2017.

# Chapter V. Final remarks and future perspectives

In this master thesis project, a new light harvesting concept has been proposed: light harvesting capacitors. This system, instead of trying to improve the charge carrier mobility within the organic materials normally used for OPV solar cell, it simply gets rid of the charge transport itself.

Firstly, a physical model was developed to understand what was actually happening inside the device during the charging and discharging process. The same model was then used to simulate the efficiency dependence on several parameters of both the insulant layer (thickness and dielectric constant) and the active layer (lifetime and dipole moment).

After this preliminary section, the actual experimental part of the work started. With the help of two different pump-probe spectroscopy set-ups, the active bi-layer itself was studied first. From the ultrafast transient analysis, it was possible to observe the charge separation mechanism that is at the very core of the LHC working mechanism. This result allowed to confirm that the thermally evaporated interface was good enough for the charge transfer to occur. On the other hand, the steady-state spectroscopy results proved that these separated-charge states were quite long-lived, which is a desired characteristic for an LHC as illustrated in the physical model.

A preventive analysis was also run on $TiO_2$ to verify its appropriateness as an insulant material. Although its behavior resulted quite atypical and although a minimum thickness limit for the device to work was present, titanium dioxide was found suitable for the LHCs fabrication. Comparing the efficiency values obtained for the actual devices with the simulated one, it is evident that a lot of optimization still needs to be done. Nonetheless, the study of the different insulant thicknesses and materials proved that the efficiency increase expected by the model was quite accurate. This is actually not true when the dielectric material is changed from the proper insulants to $TiO_2$: an unpredicted improvement in the LHC performance was found. After several different comparisons, this higher than anticipated rise in the efficiency was assigned to the atypical behavior of titania. It was surmised that, given its properties as an ETL, its presence causes an extra photo-generation of dipoles and hence a higher amount of stored energy. As a consequence, even if this phenomenon makes the charging process slower, using $TiO_2$ leads to the most performing device.

At this point it is evident that the efficiency values obtained are definitely lower than the predicted ones, even considering the quantum internal efficiency. This means that the problem is not in the light absorption, but rather in the active process itself. Specifically, it is possible that the charge separation is not efficient enough and only a small part of the generated excitons actually becomes free charges. It is also possible that, even though some long-lived dipoles where observed with the steady-state analysis, most of the separated states recombine in a very short time. Both these two considerations can be related either to the quality of the evaporated layers or to the active materials considered themselves. In the first case, a more advanced deposition technique could allow the fabrication of a cleaner interface and thus lead to an improved charge separation mechanism. This is quite trivial and easy to accomplish, while exploiting new active materials is definitely more interesting and complicated. A possible approach can be the substitution of one or both the small molecules with other p/n-type materials, in order to observe the effect on the excitons splitting and on the dipoles lifetime.

More intriguing could be to change from classic OPV heterojunctions, to a hybrid-perovskite based structure. It has been found, and widely reported in literature, that this kind of material possesses a huge dipole moment due to the presence of organic cations. These cations are relatively big if compared to the molecule structure, and for this reason they are extremely slow in their orientation process. The immediate consequence is the affecting of the charge carriers dynamic and thus the appearance of a hysteresis cycle [1]. Even though this is normally considered a drawback, it is possible that in the case of LHCs this might actually be an advantage. These huge cations should increase the amount of stored energy within the device, and moreover, since no charge transport is required in a light harvesting capacitor, their slow reorganization process should not be a problem for the charge carriers. As a final advantage, it is also possible that, given the smaller exciton binding energy characteristic of hybrid perovskites (10 times smaller), no bi-layer is required to separate the charges [2-3].

As a final remark, it must also be said that the way the efficiency is calculated starting from the transient-current trend might not be completely accurate. This assertion derives from the study of the light intensity dependence predicted by the theoretical model: it was found that increasing the radiation intensity not only the efficiency does not increase, but it actually decreases. A conclusive explanation was not found, but some suppositions were made. Specifically, it is possible that a higher intensity affects not only the number of photo-generated dipoles, but rather the overall process itself. This would mean a fundamental mistake in the theoretical model or at least some missing considerations.

In spite of this, it is also possible that the way the efficiency is physically computed might be partially incorrect: increasing the chopper frequency for instance, a certain efficiency rise was instead observed (up to 15.5 $mW/cm^2$). Moreover, measuring the LHC with a lock-in amplifier a current increase was also observed. At this point it is rather evident that a complete understanding of what is exactly happening

within the device itself has not been reached yet and that further studies are required. Some potential suggestions for future analysis include an asymmetrical light cycle measurement and a steady-state potential measurement. The first one will help to understand if all the radiation provided is actually necessary to completely charge the capacitor. The “energy waste” associated to the symmetrical light cycle might be the reason behind the efficiency decrease at the increasing intensity. The latter suggestion instead, represents a viable alternative to directly measure the stored energy without exploiting the current integration.

In conclusion, a feasible alternative device to harvest solar energy has been presented and studied. A deeper comprehension of its working mechanism has been achieved and some attempts to improve the external efficiency have been made. Despite that, there is still a lot about light harvesting capacitors that needs and deserves to be puzzled out.

# Bibliographic References

[1] R. S. Sanchez *et al.*, “Slow dynamic processes in lead halide perovskite solar cells. Characteristic times and hysteresis,” *J. Phys. Chem. Lett.*, vol. 5, no. 13, pp. 2357–2363, 2014.

[2] B. Kippelen and J.-L. Brédas, “Organic photovoltaics,” *Energy Environ. Sci.*, vol. 2, no. 3, p. 251, 2009.

[3] Z. Fan, K. Sun and J. Wang, “Perovskites for photovoltaics: a combined review of organic–inorganic halide perovskites and ferroelectric oxide perovskites”, J. Mater. Chem. A, vol. 3, p. 18809, 2015.